Adam Mickiewicz University in Poznań

Faculty of Physics

PhD Thesis

Particular Properties of Spin Waves in Magnonic Crystals: Negative Refractive Index, Nonreciprocity and Damping

Michał Mruczkiewicz

Thesis supervisor:
prof. UAM dr hab. Maciej Krawczyk
Nanomaterials Physics Division, Faculty of Physics, UAM

Thesis second supervisor:
prof. Yuri A. Filimonov
Kotelnikov Institute of Radio Engineering and Electronics, Russian Academy of Sciences

Poznań 2014

Uniwersytet im. Adama Mickiewicza

Wydział Fizyki

Praca doktorska

Szczególne właściwości fal spinowych w kryształach magnonicznych: ujemny współczynnik załamania, nieodwracalność oraz tłumienie

Michał Mruczkiewicz

Promotor:
prof. UAM dr hab. Maciej Krawczyk
Zakład Fizyki Nanomateriałów, Wydział Fizyki UAM

Promotor pomocniczy:
prof. Yuri A. Filimonov
Kotelnikov Institute of Radio Engineering and Electronics, Russian Academy of Sciences

Poznań 2014

Acknowledgements

The completion of this doctoral dissertation would not have been possible without the support of several people. I would like to express my sincere gratitude to all of them. First of all, I would like to thank my advisors, Professors Maciej Krawczyk and Yuri Alexandrovich Filimonov, for supporting me during these past years. They devoted enormous time to discussions, directing me on the track of interesting research, and also gave me the freedom to pursue various projects without objection. A special thanks to all my colleagues from Poznan, Saratov, Donetsk, Perugia, Białystok, Exeter and Munich groups for the work accomplished together as well as the pleasant time spent together. I am also very grateful to my girlfriend, family and friends for support and understanding during all this time.

Abstract

In this PhD thesis I am presenting the results of investigation of spin wave properties in periodic ferromagnetic structures (one-dimensional magnonic crystals). The main attention of research was put on developement of numerical methods and analysis of spin waves properties that are important for designing a functional device. Three subjects of spin waves properties were studied and they can be classified as: i) influence of damping on standing spin wave formation ii) metamaterial properties for electromagnetic waves propagating through magnonic crystal and iii) nonreciprocal dispersion of spin waves. In particular I have shown the analysis of the influence of the damping factor on the spectrum of ferromagnetic resonance, the influence of metallic overlayer on the damping, influence of structural parameters of magnonic crystals on the magnetic permeability function of metamaterial based on the crystal. I have also presented a detailed analysis of symmetry breaking of the dispersion relation of spin waves propagating in the ferromagnetic films in contact with metal. The numerical calculation were confronted with measured data, when available, and agreement between them was shown.

Streszczenie

W pracy doktorskiej pod tytułem "Particular Properties of Spin Waves in Magnonic Crystals: Negative Refractive Index, Nonreciprocity and Damping (Szczególne właściwości fal spinowych w kryształach magnonicznych: ujemny współczynnik załamania, nieodwracalność oraz tłumienie)ńapisanej w języku angielskim, prezentuje rezultaty moich badań prowadzonych nad właściwościami fal spinowych rozchodzących się w periodycznych strukturach ferromagnetycznych. Fala spinowa jest to koherentna precesja momentów magnetycznych, która może być wzbudzona poprzez oscylujące mikrofalowe zewnętrzne pole magnetyczne. Procesujące momenty magnetyczne wzbudzone lokalnie, np. w cienkiej warstwie lub krysztale magnonicznym, będą oddziaływały z sąsiadującymi momentami magnetycznymi poprzez oddziaływania dipolowe oraz wymienne. Dla pewnego zakresu częstotliwości oscylującego zewnętrznego pola magnetycznego, leżącego w okolicach częstotliwości rezonansowej, mogą być wzbudzone propagujące fale spinowe. Zależność częstotliwości od wektora falowego tych fal jest opisywany poprzez relacje dyspersji. Badanie relacji dyspersji jest istotnym elementem pracy doktoranckiej.

W rozprawie doktorskiej rozważanymi strukturami ferromagnetycznymi są cienkie warstwy ferromagnetyczne oraz jednowymiarowe kryształy magnoniczne. Kryształ magnoniczny może być np. złożony z naprzemiennie rozmieszczonych pasków materiałów ferromagnetycznych i jego struktura opisywana jest poprzez periodycznie powtarzającą się komórkę elementarną. Do rozwiązania zagadnienia brzegowego oraz związanego z nim równania różniczkowego cząstkowego, które opisuje fale spinowe stosuję analityczne oraz numeryczne metody. Obliczenia są wykonywane dla struktur umieszczonych w zewnętrznym polu magnetycznym, które przyłożone jest równolegle do powierzchni warstwy i jest wystarczająco silne aby wszystkie momenty magnetyczne w strukturze (w stanie podstawowym) były skierowane wzdłuż kierunku tego pola. Ponieważ dla fal spinowych amplitudy dynamicznych składowych momentu magnetycznego (prostopadłych do zewnętrznego pola magnetycznego) są znacznie mniejsze od wartości magnetyzacji nasycenia, może być stosowane przybliżenie liniowe. Ponadto rozwiązania są zakładane w postacie fali monochromatycznej i rozwiązania poszukiwane są w dziedzinie częstotliwości.

W pracy doktorskiej skoncentrowałem się na badaniach, które można podzielić na trzy zagadnienia: i) wpływ tłumienia na formowanie się fal stojących w kryształach magnonicznych, ii) meta-materiałowe własności (w tym ujemny współczynnik załamania) dla fal elektromagnetycznych rozchodzących się poprzez kryształ magnoniczny, iii) zjawisko nieodwracalnej dyspersji fal spinowych. Praca doktorska składa się z 6 rozdziałów.

Wprowadzenie teoretyczne zostało zawarte w rozdziale pierwszym. Rozdział ten zawiera opis głównych pojęć potrzebnych do opisu fal spinowych w kryształach magnonicznych. Analityczne obliczenia dyspersji zostały zaprezentowane dla jednorodnej warstwy ferromagnetycznej z polem przyłożonym wzdłuż warstwy. Ponadto wpływ oddziaływań wymiennych oraz podstawowe właściwości periodycznych struk-

tur ferromagnetycznych (kryształów magnonicznych) zostały omówione. Zagadnenia zaprezentowane w tym rozdziale będą przydatne do opisu wyników prezentowanych w dalszej części pracy.

Rozdział drugi przedstawia przegląd podstawowych metod eksperymentalnych stosowanych do badania wzbudzeń fal spinowych. Opisane są techniki doświadczalne takie jak: rezonans ferromagnetyczny, rozpraszanie Brillouina czy pomiary absorpcji i transmisji poprzez fale spinowe wzbudzane antenami. Wyniki pomiarów tymi metodami były wykorzystywane bezpośrednio w pracy lub były używane do sprawdzenia metod numerycznych.

Rozdział nr. 3 zawiera opis metod numerycznych używanych do obliczeń widma fal spinowych. W pierwszej części została opisana metoda fal płaskich a w drugiej, metoda elementów skończonych. Zaimplementowanie metody elementów skończonych do obliczeń dyspersji fal spinowych w kryształacj magnonicznych jest ważnym osiągnięciem prezentowanym w pracy. Metoda ta daje dużą swobodę w definicji geometrii struktury i pozwoliła na przeprowadzenie szeregu obliczeń przedstawianych w dalszej części pracy.

Kolejny rozdział (nr. 4) prezentuje wyniki obliczeń modów stojących za pomocą metody elementów skończonych. Wyniki te zostały zaprezentowane dla jednowymiarowych kryształów magnonicznych składających się z warstw kobaltu oraz permaloju o grubości 50 nm. Period rozważanych kryształów magnonicznych był rzędu kilku mikrometrów. Dane eksperymentalne z pomiaru rezonansu ferromagnetycznego otrzymane od współpracowników z grupy doświadczalnej zostały porównane z obliczeniami numerycznymi. Dzięki rozwiniętej metodzie numerycznej oraz danych o tłumieniu uzyskanym z danych doświadczalnych można zinterpretować powstające fale stojące i odtworzyć widmo rezonansowe. W rezultacie tych badań wyjaśniono obserwowane linie absorpcyjne w widnie rezonansu jako pochodzące od fali spinowej zlokalizowanej w materiale kobaltu lub permaloju. Pomimo większego tłumienia dla modów fal spinowych wyższego rzędu, sprzężenie stojących fal spinowych z falą elektromagnetyczną jest dostatecznie duże i może być wykorzystywane do konstrukcji urządzeń, do czego nawiązuje następny rozdział.

Ściśle związane z badaniem widma rezonansowego jest przeprowadzona w rozdziale piątym, analiza struktur mogących posiadać ujemny współczynnik załamania światła. Proponowana struktura jest złożona z oddzielonych od siebie jednowymiarowych kryształów magnonicznych w których fale stojące są odpowiedzialne za występowanie ujemnej podatności magnetycznej. Badania prezentowane w tym rozdziale zostały przeprowadzone za pomocą metody fal płaskich oraz analitycznych obliczeń podatności magnetycznej dla jednorodnych warstw. Analiza rozmieszczenia amplitudy fali spinowej w strukturze pozwoliła na oszacowanie sprzężenia wzbudzeń fal spinowych z falą elektromagnetyczną w zakresie setek gigaherców. Dodatkowo pokazany został wpływ parametrów strukturalnych kryształu magnonicznego na funkcje podatności magnonicznej.

W rozdziale szóstym przedstawiona została analiza wpływu warstwy metalicznej na dyspersję fal spinowych. Ze względu na brak symetrii modów fal spinowych propagujących się w cienkiej warstwie prostopadle do zewnętrznego pola magnetycz-

nego (przyłożonego wzdłuż warstwy) można zdefiniować strukturę dla których fala spinowa propagująca się w określonym kierunku będzie posiadała rożną dyspersje od fali propagującej się w przeciwnym kierunku. W części 6.1 opisany jest wpływ metalu o skończonej przewodności na jednorodną warstwę ferromagnetyczną. Dokładna analiza wpływu parametrów na zakres wektora falowego występowania nieodwracalnej dyspersji została również tam zamieszczona. W tej części jest również zawarte wyprowadzenie przybliżonej formuły analitycznej na relację dyspersji oraz analiza tłumienia indukowanego przez warstwę metaliczną.

Przykład kryształu magnonicznego posiadającego nieodwracalną dyspersję został zaprezentowany w części 6.2. Złamanie symetrii w tego typu strukturach ma wpływ na fale spinowe i prowadzi do występowania nowych efektów. Nieodwracalność prowadzi między innymi do pojawienia się skośnych przerw magnonicznych. W tej samej części zaprezentowane są obliczenia dla dwóch kryształów magnonicznych złożonym z warstw o grubości rzędu kilkudziesięciu (o małym oraz znacznym kontraście magnetyzacji) w kontakcie z idealnym metalem. Analiza amplitudy fal spinowych pozwaliła na zrozumienie mechanizmu powstawania niesymetrycznej struktury pasmowej.

W tym samym rozdziale, w części 6.3, opisany został kolejny kryształ magnoniczny w kontakcie z metalem. Kryształ ten składał się z jednorodnej warstwy granatu itrowo-żelazowego o grubości rzędu kilku mikrometrów z naciętymi rowkami o periodyczności 150 mikrometrów. Tak zdefiniowana struktura pozwaliła na doświadczalne zbadanie przerw magnonicznych w pomiarach transmisji fal spinowych. Dane eksperymentalne potwierdzają wskazane przez numeryczne obliczenia podwyższenie częstotliwości przerwy magnonicznej dla kryształu w kontakcie z metalem.

Podsumowanie wyników prezentowanych w pracy doktorskiej zawarte jest w ostatnim rozdziale, nr. 7.

Contents

Preface

This PhD thesis presents results of investigations on particular properties of spin wave (SW) excitations in thin ferromagnetic structures. A spin wave is a physical phenomenon widely investigated in various magnetic structures and it is a coherent precession of magnetic moments. An alternating external magnetic field can serve as a source of spin wave excitation in uniform ferromagnetic films or one dimensional magnonic crystal (1D MC). The precession of magnetic moments is induced locally. Neighboring magnetic moments start to precess due to dipole and exchange interactions that exist in the system. At specific frequencies, the excitation will be formed as traveling wave, with wavevector determined by the aforementioned interactions. A study of frequency-wavevector relation (dispersion relation) is one of the main task solved in the thesis.

The structures under consideration are homogeneous magnetic films and periodically arranged magnetic elements, i.e., magnonic crystals. The analytical and numerical methods are used to solve partial differential equations that govern the magnetization precession in such structures. The study is made under the influence of in-plane bias magnetic field (e.g, along the z-axix), sufficiently strong to saturate magnetization in the same direction. The distortion of the magnetization vector from its equilibrium orientation is assumed small (x and y components of a magnetization are much smaller than the z component), so the oscillation might be described under the assumption of constant z component of the magnetization (i.e., in linear approximation). Further, the solutions are looked for in the form of monochromatic waves allowing for analysis of SWs eigen-excitation in the frequency domain.

The following particular properties of SWs in such structures are investigated in details: damping, negative refractive index (NRI) and nonreciprocity. The analysis of the influence of the intrinsic damping on the FMR spectra is made. In addition, the metal induced damping is studied for uniform ferromagnetic films with various structural parameters. The NRI properties are theoretically studied for 1D MCs. The studied structures are considered as potentially possessing the negative permeability at sub-THz frequency range. Nonreciprocal dispersion properties are extensively studied in the metalized structures and potential applications of this property are listed. The theoretical results are partially confronted with measured experimental data.

The dissertation is composed of six chapters. In the first chapter, the introduction to the theory of SWs excitations in thin ferromagnetic films and magnonic crystals is given. The equations and assumption that are used to describe harmonic and coherent oscillation of magnetization are listed. The analytical procedure of obtaining the SW dispersion relation is presented for uniform magnetic film under the influence of an in-plane bias magnetic field in magnetostatic approximation. In addition, the influence of exchange interaction is discussed. A brief introduction to magnonic crystals is given. In the chapter, the summary of the recent trends in SWs research and their potential applications as part of functional devices is also outlined.

The detailed theoretical description is followed by the overview of the experimental methods used to characterize SWs (chapter 2). The experimental techniques such as: Ferromagnetic Resonance (FMR), Brillouin Light Scattering (BLS) and measurements in the absorption and transmission modes with Vector Analyzers are described. The results of measurements from described methods are either used directly within the thesis or serve to verify the numerical methods of calculations.

In chapter 3 the numerical procedures that are used to calculate SW dispersion relation presented in the dissertation are described. The first part of the chapter addresses the Plane Wave Method (PWM), whereas the second part deals with the Finite Element Method (FEM).

Chapter 4 reports the results of FEM calculations and comparison of these results with FMR measurements for one-dimensional MCs composed of alternating Co and Py stripes of depth of tens of nanometers and a periodicity of a few micrometers. Also the structures composed of slabs of Co and Py separated by dielectric slab underwent investigation. It is shown that with established calculation method complemented with the damping analysis it is possible to understand the formation of standing spin waves in MCs and to explain the FMR data. The analysis is made for two field configurations, when the bias magnetic field is along the stripes and perpendicular to the stripes.

In chapter 5, the PWM together with analytical formulas is used to define the effective permeability tensor of a metamaterial. The investigation is made for thin slabs of one-dimensional MCs in order to obtain a structure that possesses negative permeability at elevated frequencies. The analysis of the spatial dependency of amplitudes of dynamic magnetization components is conducted in order to demonstrate the strong coupling of high order magnonic modes with electromagnetic wave from the microwave part of the spectrum. It is found that the coupling between electromagnetic waves and magnonic modes can be significantly enhanced for the specific design of the magnonic structure as a result of the lateral quantization of SWs. These results suggest that magnonic crystals are therefore promising candidates for the negative refractive index metamaterials. The negative permeability at frequencies close to 100 GHz can be achieved in structures feasible for fabrication with present technology.

In the chapter 6 an analysis of the influence of metal overlayer on the SW dispersion is made. Due to nonreciprocal character of SWs propagating perpendicular

to the bias magnetic field, it is possible to define structure with different dispersions for waves propagating in opposite directions. Specific conditions for the appearance of nonreciprocal dispersion are discussed in the subsection 6.1. A detailed discussion of the metal influence on the spin waves in uniform magnetic film is presented as well as analysis of metal induced damping. The approximated analytical formulation of the SW dispersion relation for a uniform film is given.

The analysis and example of magnonic structures composed of slabs of thickness in range of tens of nanometers with nonreciprocal dispersion are presented in the subsection 6.2. The nonreciprocal property of propagation has significant consequences for dynamical properties of MCs and new effects are analyzed. In particular, nonreciprocity leads to the appearance of indirect magnonic band gaps in magnonics crystals with both low and high magnetization contrast. A nonreciprocity in low contrast magnonic crystals leads to appearance of several magnonic band gaps located within the first Brillouin zone for waves propagating along a metallized surface. The analysis of spatial distribution of dynamic magnetization amplitudes allows to explain the mechanism of magnonic bands formation in structures with nonreciprocal properties.

In the same chapter, a special case of nonreciprocal structure is investigated further in subsection 6.3, i.e., a magnonic crystal composed of micrometer thick yttrium iron garnet with a metal overlayer characterized by finite conductivity. A structure of this kind is closer to physical realization than perfect electric conductors. The theoretical investigation is compared with the results of experiment, confirming the expected effects of metal on the SW dispersion.

The summary of the results reported in the dissertation are presented in chapter 7.

Chapter 1

Introduction

The periodically arranged magnetic materials form a magnonic crystal, novel material possessing not observed before properties. The dispersion relation of spin waves is significantly different from homogeneous material, e.g., forbidden frequency gaps can exists. This difference can cause that the MCs will be widely used in the application in the close future as photonic crystals are used now [1, 2]. Also molding the flow of plasmons, elastic or acoustic waves is under development. Although the research of MCs begin in more or less at the same time as photonic crystals, the experimental attempts to realize the magnonic crystal based devices had lower success. The prototypes has been proposed in the macroscopic scale [3, 4]. The existing obstacles to implement MCs in technology such as high damping, low propagation length or complex electrical excitation and detection of SWs needs to be overcome.

Nevertheless, the knowledge of this field of study expands. Advanced analytical and numerical model together with manufacture and experimental techniques continuously develops [5, 6, 7, 8, 9, 10, 11, 12, 13, 14]. One of the branches, magnonics, brought a special attention, where SWs are used for carrying and processing the information [15, 16, 17, 18]. The potential advantages of magnonic devices are such as: miniaturization below the size of device where the electromagnetic wave is used, low energy consumption, fast operation rates compared with electronic devices [17, 19] or easy tunability (controlled with the external magnetic field). The dispersions of spin waves in the MCs depends on the arrangement of the magnetization vector. The reprogramability can be achieved by controlling the direction of the magnetization, leading to applications such as magnetic logic devices [20, 21, 22]. The MCs might be also suitable in the interdisciplinary study, e.g., linked with semiconductor technology or spintronics.

The classification of MCs can be made based on the structural size [22]. Thus the classes of finite thickness and bulk MCs are differentiated. For both classes, MCs can be classified with one (1D), two (2D) or three-dimensional (3D) translational symmetry. In this thesis, the research effort are put solely on the 1D finite thickness MCs. It contains the investigation of the particular properties of the SWs in magnonic crystals, i.e., interaction of SWs and EM wave, nonreciprocal properties

of SWs and damping.

The presented findings important for implementation of MCs are supported by comparison of calculated FMR spectra with the experiment in the chapter 4. The strong absorption due to the standing spin waves leads to the idea of metamaterial with negative refractive index or close to zero refractive index at elevated frequencies. The permeability function of metamaterial is defined theoretically in the chapter 5 in order to define the interaction of SW with EM. It is possible to design the optimal response of the metermaterial, if the influence on the structural and physical parameters of element composing the metamaterial is known. At the moment there are few ideas in the NRI research, e.g., split ring resonators [23]. However the experimental realization at elevated frequencies requires structural miniaturisation which is difficult for the device basing on the complicated geometry. The metamaterial described in this thesis is based on the simple geometry, the structures of similar parameters are possible to manufacture nowadays.

Another direction of research in the SW subject is related to the property of nonreciprocal dispersion. The SWs propagating in perpendicular direction to the bias magnetic field in the thin film posses a nonreciprocal distribution of amplitude across the film thickness. Breaking the symmetry of the thin film might lead to the nonreciprocal dispersion. In the chapter 6 the conditions for observing the nonreciprocal dispersion are discussed and discussion of MCs with nonreciprocal dispersion is made. The device based on the MCs with nonreciprocal dispersion has been already proposed and studied experimentally, i.e., as sensitive magnetic field sensor [24]. In addition, the nonreciprocal dispersion might be employed in miniaturized microwave elements, such as isolators or circulators, where its anisotropic properties might be exploited.

1.1 Spin Waves

The magnetic moment in solids associated with electrons is related either to orbital angular momentum $\mu_{\mathbf{l}}$ or the intrinsic angular magnetic moment, spin $\mu_{\mathbf{s}}$. They are related due to kinetics of electrons by :

$$\mu_{\mathbf{l}} = -\frac{\mu_{\mathbf{B}}}{\hbar}\mathbf{l}, \tag{1.1}$$

$$\mu_{\mathbf{s}} = \frac{g_e \mu_B}{\hbar}\mathbf{s} = -\gamma_e \mathbf{s}, \tag{1.2}$$

where $\mathbf{l}$ is angular momentum, $\mathbf{s}$ spin angular momentum, g_e is electron spin g-factor and characterize magnetic moment of electron, μ_B is Bohr magneton and $\hbar$ is reduced Planck constant, γ_e is gyromagnetic ratio of an isolated electron.

For light atoms and weak magnetic fields, the total angular momentum j might express the total magnetic moment μ:

$$\mu = -\frac{g_j \mu_B}{\hbar}\mathbf{j}, \tag{1.3}$$

where g_j is Landé g factor, $\mathbf{j}$ is total angular momentum, $\mathbf{j} = \mathbf{l} + \mathbf{s}$.

The concept of spin waves as collective excitations of the magnetic moments was introduced by Felix Bloch [25]. A spin wave is an assembly of precessing magnetic moments about the effective magnetic field (H_{eff}) direction. In the discrete lattice of magnetic moments the neighboring spins precess with constant phase difference (see Fig. 1.1) and their amplitude may vary, depending upon structural parameters. The origin of this movement will be discussed further in this chapter.

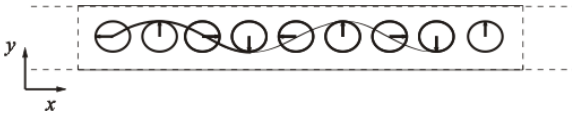

Figure 1.1: The dynamical components of the magnetic moment vectors (these perpendicular to the direction of the effective magnetic field) $\mu_{s,x}(\mathbf{r}, t)$ and $\mu_{s,y}(\mathbf{r}, t)$ components at some fixed time t. The precession of neighboring spins is realized with constant phase difference around direction of the effective magnetic field pointing perpendicular to the cross section plane..

Forces acting on the magnetic moment under external magnetic field can be considered. Magnetic moments of the electrons in ferromagnets tend to align along the external magnetic field to minimize the energy. However, the magnetic angular moment of electrons under applied field result in torque that is acting perpendicular to the magnetic moment and applied field. If only contribution from the spin angular momentum is considered (the orbital angular momentum is usually quenched in solids [26]), the moment of force can be defined as:

$$\mathbf{\Gamma_s} = -\mu_\mathbf{s} \times \mu_0 \mathbf{H}_{\text{eff}}, \tag{1.4}$$

where μ_0 is the vacuum permeability. This should equal to derivative of angular momentum with respect to time:

$$\mathbf{\Gamma_s} = \frac{d\mathbf{s}}{dt} = \frac{d\mu_\mathbf{s}}{\gamma dt}. \tag{1.5}$$

The torque equation takes the form:

$$\frac{d\mu_\mathbf{s}}{\gamma dt} = -\mu_\mathbf{s} \times \mu_0 \mathbf{H}_{\text{eff}}, \tag{1.6}$$

where the effective magnetic field might be assumed to have contribution from the external magnetic field and the dynamic magnetic field:

$$\mathbf{H}_{\text{eff}}(\mathbf{r}, t) = \mathbf{H}_0(\mathbf{r}) + \mathbf{h}(\mathbf{r}, t), \tag{1.7}$$

where $\mathbf{r}$ is a position vector. The $\mathbf{h} = (h_x, h_y)$ are dynamic components of the effective magnetic field.

The Eq. 1.6 can be generalized to the equation describing macroscopic magnetization 1.9, since:

$$\mathbf{M}(\mathbf{r},t) = \frac{N}{V}\mu_{\mathbf{s}}, \tag{1.8}$$

where V is a volume, and N is the number of magnetic moments in the sample. The quantity $\frac{N}{V}$ is also defined as n, the density of magnetic moments. The Eq. 1.6 can be transformed to:

$$\frac{\partial \mathbf{M}(\mathbf{r},t)}{\partial t} = -\gamma\mu_0 \mathbf{M}(\mathbf{r},t) \times \mathbf{H}_{\text{eff}}(\mathbf{r},t). \tag{1.9}$$

This equation describe the precession of the magnetization in a ferromagnetic material in external magnetic field. It was introduced by Landau and Lifshitz (LL) [27].

The LL equation written in the form 1.9 describes the processional movement of the magnetization around the direction of the magnetic field, see Fig. 1.2. Since there is no energy dissipation, the precession will be not damped. An additional term, the phenomenological Gilbert term [28], is added in order to take into account the dissipation of energy:

$$\frac{\partial \mathbf{M}(\mathbf{r},t)}{\partial t} = -\gamma\mu_0 \mathbf{M}(\mathbf{r},t) \times \mathbf{H}_{\text{eff}}(\mathbf{r},t) - \frac{\alpha\mu_0}{M_S}\mathbf{M}(\mathbf{r},t) \times \frac{\partial \mathbf{M}(\mathbf{r},t)}{\partial t}, \tag{1.10}$$

where α is a damping coefficient. This equation is known as Landau-Lifshitz-Gilbert equation. Damping is a loss of energy of the macroscopic magnetization (magnetic moment per unit volume). There are few damping mechanism leading to this transfer of energy, e.g., it can be due to eddy currents, lattice vibrations, scattering on strains or scattering on defects [28]. The effect of damping on the precessional motion of the magnetization is a reduction of the angle of precesion up to stabilization of the magnetization vector along the direction of the effective magnetic field Fig. 1.2.

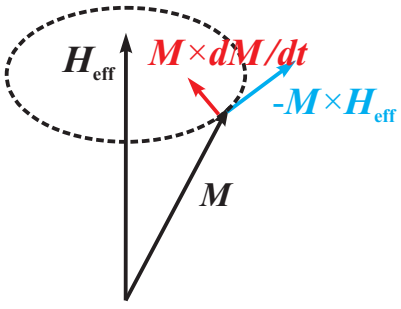

Figure 1.2: The terms of the Landau-Lifshitz-Gilbert equation: precession (blue arrow) and damping (red). The trajectory of the magnetization with zero damping is shown by dashed circle.

The uniform ferromagnetic resonance can be considered as an example of spin

wave excitation with infinitely long wavelength (zero wavevector) Fig. 1.3. It means also that the phase shift between neighboring oscillating magnetic moments is absent.

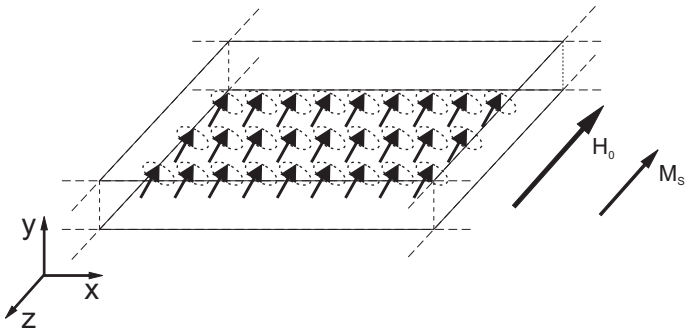

Figure 1.3: The uniform oscillation of the magnetic moments under the applied bias magnetic field in a film of ferromagnetic material.

A spin wave with finite wavevector might also exists in the magnetic body. A propagating spin wave appears due to the existing interactions between spins, i.e., dipole and exchange interactions. Dipole interactions originate from the magnetic field distribution around magnetic moment. Exchange interaction is a quantum effect, appearing due to the Pauli principle and electrostatic interactions.

The propagating spin waves can exists in the magnetic material naturally due to the thermal excitations or they can be induce by the external fields. For instance the microwave antennas can induced locally the precession of the magnetic moments. Neighboring magnetic moments start to precess, due to dipole and exchange interactions that exist in system. At specific frequencies of external harmonic microwave field, the excitation in the ferromagnetic film is formed in the form of traveling wave, with wavevector determined by the dispersion relation. A study of frequency-wavevector relation (dispersion relation) is one of the main task solved in my thesis.

1.2 Dipole Spin Waves

The analytical approach often used for calculating the SW dispersion relation in uniform thin films is based on solving the LL equation 1.9 and Maxwell equation for magnetostatic potential in the magnetostatic approximation. [29] The magnetostatic potential is defined separately for each material (i.e., for the ferromagnetic material and its nonmagnetic surrounding) and linked together by the electromagnetic boundary conditions. This leads to a system of secular equations which can be solved analytically in some cases, but in general the numerical solutions are required. The dispersion relation of SWs in a magnetic material surrounded by a dielectric, in contact with a perfect conductor[30] or separated from a perfect conductor by a dielectric of finite width can be determined in this way too.[31] In a similar manner

the dispersion relation has been obtained for SWs propagating in various geometries, [29, 32] with the exchange interaction taken into account,[33, 34] or in a ferromagnetic film surrounded by a magnetic wall.[35] The influence of the finite conductivity of the magnetic film on the SWs was studied with the use of Green's functions.[36]

The configuration in which the external magnetic field H_0 is applied in the plane of the thin film and the wave vector of the propagating SW is perpendicular to this field is referred to as the Damon-Eshbach (DE) geometry. [29] If the wave vector of the propagating SW is parallel to the field, the excitation is refereed to as Backward Volume(BV) geometry.

It is important for physical phenomena discussed in the thesis to present the analytical calculation given in [29] for in plane magnetized ferromagnetic film and in plane propagating spin waves. The results of those calculations will be referred throughout the thesis.

The Maxwell equations in the magnetostatic approximation for nonconductive materials are:

$$\nabla \times \mathbf{H}_{\text{eff}} = 0, \tag{1.11}$$

$$\nabla \cdot (\mathbf{H}_{\text{eff}} + \mathbf{M}) = 0. \tag{1.12}$$

In magnetostatic approximation, the time dependance of the electric field vector $\mathbf{E}$ is neglected in the Maxwell equations. The electric field can be calculated from the third equation:

$$\nabla \times \mathbf{E} = \frac{\partial(\mathbf{H}_{\text{eff}} + \mathbf{M})}{\partial t}. \tag{1.13}$$

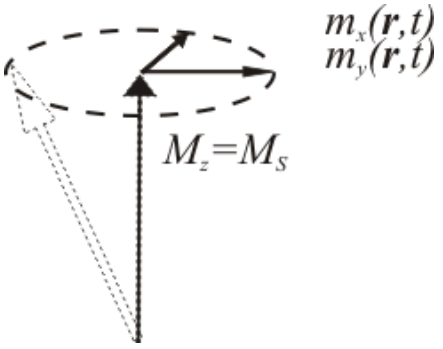

Figure 1.4: Approximation of constant $M_z = M_S$ component magnetization vector is valid if m_x and m_y components fulfill: m_x, $m_y << M_S$.

Under the influence of external magnetic field, if H_0 is strong enough to saturate the ferromagnetic film, the magnetization vector can be decomposed into static (parallel to H_0) and dynamical components from the perpendicular plane:

$$\mathbf{M}(\mathbf{r}, t) = \mathbf{M}_z(\mathbf{r}) + \mathbf{m}(\mathbf{r}, t). \tag{1.14}$$

The magnetization and magnetic field are linearized, by assumption time independence of the z component of the magnetization vector, see Fig. 1.4. The

$\mathbf{m} = (m_x, m_y)$, $\mathbf{h} = (h_x, h_y)$ are dynamic components assumed in the form of monochromatic wave: $\sim \exp(-i\omega t)$, where ω is a angular frequency of SW. The spatial distribution of these dynamic components characterize the profile of this SW excitation.

If the exchange and anisotropy is neglected, only dipolar interaction will be responsible for forming spin wave. From the Eq. 1.9 the following equations are defined:

$$\begin{pmatrix} i\frac{\omega}{\gamma\mu_0}m_x \\ i\frac{\omega}{\gamma\mu_0}m_y \end{pmatrix} = \begin{pmatrix} m_y H_0 - M_S h_y \\ M_S h_x - m_x H_0 \end{pmatrix} \tag{1.15}$$

and transformed to:

$$\begin{pmatrix} h_y \\ h_x \end{pmatrix} = \begin{pmatrix} i\frac{\omega}{M_S\gamma\mu_0}m_x + \frac{H_0}{M_S}m_y \\ \frac{H_0}{M_S}m_x - i\frac{\omega}{M_S\gamma\mu_0}m_y \end{pmatrix}. \tag{1.16}$$

That allows to define the relation between dynamical components of the magnetic field and magnetization:

$$\mathbf{h} = \begin{pmatrix} \frac{H_0}{M_S} & -i\frac{\omega}{M_S\gamma\mu_0} \\ i\frac{\omega}{M_S\gamma\mu_0} & \frac{H_0}{M_S} \end{pmatrix} \mathbf{m}. \tag{1.17}$$

The relation between the dynamic $\mathbf{m}$ and $\mathbf{h}$ components is:

$$\mathbf{m} = \begin{pmatrix} \kappa & -i\nu \\ i\nu & \kappa \end{pmatrix} \mathbf{h}, \tag{1.18}$$

where:

$$\kappa = \frac{\Omega_H}{\Omega_H^2 - \Omega^2},\ \nu = \frac{\Omega}{\Omega_H^2 - \Omega^2} \tag{1.19}$$

and

$$\Omega = \frac{\omega}{\gamma\mu_0 M_\mathrm{S}},\ \Omega_H = \frac{H_0}{\mu_0 M_\mathrm{S}}. \tag{1.20}$$

Neglecting the dynamic electric field and currents in Eq. 1.11 allows to define the magnetic field by the magnetostatic potential, ψ:

$$\mathbf{h} = \nabla\psi. \tag{1.21}$$

The Eqs 1.12 and 1.21 leads to:

$$\nabla^2\psi + \nabla\mathbf{m} = 0, \tag{1.22}$$

which leads to following equations for magnetostatic potential inside the ferromagnetic material, (internal, ψ^i), and outside (external, ψ^e):

$$(1+\kappa)(\frac{\partial^2\psi^i}{\partial x^2} + \frac{\partial^2\psi^i}{\partial y^2}) + \frac{\partial^2\psi^i}{\partial z^2} = 0, \tag{1.23}$$

$$\nabla^2 \psi^e = 0. \tag{1.24}$$

The electromagnetic boundary conditions require continuity of the normal component of the magnetic induction field **B** and tangential component of **H** field. Setting the center of ferromagnetic film at the origin of the x, y, z Cartesian coordinating system (so the edges of the film characterized by the thickness d are located at $x = \pm\frac{d}{2}$) gives:

$$(1+\kappa)\frac{\partial \psi^i(\pm\frac{d}{2})}{\partial x} - i\nu\frac{\partial \psi^i(\pm\frac{d}{2})}{\partial y} = \frac{\partial \psi^e(\pm\frac{d}{2})}{\partial x}, \tag{1.25}$$

$$\psi^i(\pm\frac{d}{2}) = \psi^e(\pm\frac{d}{2}). \tag{1.26}$$

The solutions of the Eq. 1.23 and 1.24 with the boundary conditions 1.25 and 1.26 can be looking for with the separation variables method. In this method the magnetostatc potential is written in the form:

$$\psi(x, y, z) = X(x)Y(y)Z(y), \tag{1.27}$$

To fulfill the Eq. 1.26 and due to homogeneity in the film plane, only the function $X(x)$ varies when moving from inside to outside of the ferromagnetic film:

$$\psi^i(x, y, z) = X^i(x)Y(y)Z(y), \tag{1.28}$$

$$\psi^e(x, y, z) = X^e(x)Y(y)Z(y). \tag{1.29}$$

The exponential or sinusoidal functions of x, y and z are acceptable solutions. The function X is required to disappear at ∞ and $-\infty$, thus:

$$X^e(x) = (b_1 e^{k_x^e x}),\ x < -\frac{d}{2}, \tag{1.30}$$

$$X^e(x) = (a_3 e^{-k_x^e x}),\ x > \frac{d}{2}, \tag{1.31}$$

where b_1 and a_3 are unknown coefficients and k_x^e is real number. Inside the sample the solution is assumed in the form:

$$X^i(x) = (a_2 \sin k_x^i x + b_2 \cos k_x^i x), \tag{1.32}$$

where a_2 and b_2 are unknown coefficients and k_x^e can be real or imaginary number.

We require that the k_y and k_z are real arguments. The Y and Z should remain finite as y and z tends to infinity, the Y and Z should be sinusoidal function with arbitrary origin. Thus the equation 1.25 require that Y must be [29, 37]:

$$Y(y) = e^{ik_y y} \tag{1.33}$$

and the Z is taken in the form:

$$Z(z) = \cos k_z z. \tag{1.34}$$

Inserting these forms of magnetostatic potential functions in Eqs. 1.23 and 1.24 will define the wave vector components along x, inside and outside the ferromagnetic film, k_x^e and k_x^i as:

$$k_x^e = \sqrt{k_y^2 + k_z^2}, \tag{1.35}$$

$$k_x^i = \sqrt{-k_y^2 - k_z^2/(1+\kappa)}. \tag{1.36}$$

Using the boundary conditions allow to define 4 equations with 4 unknown variables (b_1, a_2, b_2, a_3), that after elimination of b_1 and a_3 can be written in form of the matrix multiplication:

$$\mathbf{M}\begin{pmatrix} a_2 \\ b_2 \end{pmatrix} = \begin{pmatrix} m_{11} & m_{12} \\ m_{21} & m_{22} \end{pmatrix}\begin{pmatrix} a_2 \\ b_2 \end{pmatrix} = 0, \tag{1.37}$$

where:

$$m_{11} = (1+\kappa)\sqrt{-k_y^2 - \frac{k_z^2}{(1+\kappa)}}\cos\frac{1}{2}\sqrt{-k_y^2 - \frac{k_z^2}{(1+\kappa)}}d + (\sqrt{k_y^2+k_z^2} - k_y\nu)\sin\frac{1}{2}\sqrt{-k_y^2 - \frac{k_z^2}{(1+\kappa)}}d, \tag{1.38}$$

$$m_{12} = ((-\sqrt{k_y^2+k_z^2} + k_y\nu)\cos\frac{1}{2}\sqrt{-k_y^2 - \frac{k_z^2}{(1+\kappa)}}d + (1+\kappa)\sqrt{-k_y^2 - \frac{k_z^2}{(1+\kappa)}}\sin\frac{1}{2}\sqrt{-k_y^2 - \frac{k_z^2}{(1+\kappa)}}d), \tag{1.39}$$

$$m_{21} = (1+\kappa)\sqrt{-k_y^2 - \frac{k_z^2}{(1+\kappa)}}\cos\frac{1}{2}\sqrt{-k_y^2 - \frac{k_z^2}{(1+\kappa)}}d + (\sqrt{k_y^2+k_z^2} + k_y\nu)\sin\frac{1}{2}\sqrt{-k_y^2 - \frac{k_z^2}{(1+\kappa)}}d, \tag{1.40}$$

$$m_{22} = -(-(\sqrt{k_y^2+k_z^2} + k_y\nu)\cos\frac{1}{2}\sqrt{-k_y^2 - \frac{k_z^2}{(1+\kappa)}}d + (1+\kappa)\sqrt{-k_y^2 - \frac{k_z^2}{(1+\kappa)}}\sin\frac{1}{2}\sqrt{-k_y^2 - \frac{k_z^2}{(1+\kappa)}}d). \tag{1.41}$$

The nontrivial solutions are found from the equation: $det(\mathbf{M}) = 0$. Leading to characteristic equation that can be solved numerically (e.g., with the Newton iterations):

$$2(1+\kappa)\sqrt{k_y^2+k_z^2}\sqrt{-k_y^2 - \frac{k_z^2}{(1+\kappa)}}\cot\sqrt{-k_y^2 - \frac{k_z^2}{(1+\kappa)}}d + ((2+\kappa)k_z^2 + k_y^2(2+2\kappa+\kappa^2-\nu^2)) = 0. \tag{1.42}$$

The results of the calculations for 30 nm film of Co: $d = 30$ nm, $M_S = 1.2 \cdot 10^6$ A/m, $\gamma = 176$ GHz/T, $\mu_0 H_0 = 0.1$ T are presented in the Fig. 1.5. The characteristic positive group velocity of waves propagating perpendicular to the field (DE geometry) and negative group velocity for waves propagating in parallel direction (BV geometry) can be seen. The dispersion relation is shown in two equivalent dependence: as a frequency in dependence on the wave vector with the fixed external magnetic field (a), and as an external (resonance) magnetic field in dependence on k with the fixed frequency (b). These to kinds dispersion relation

are characteristic for VNA-FMR and FMR measurements described in the chapter 2, respectively.

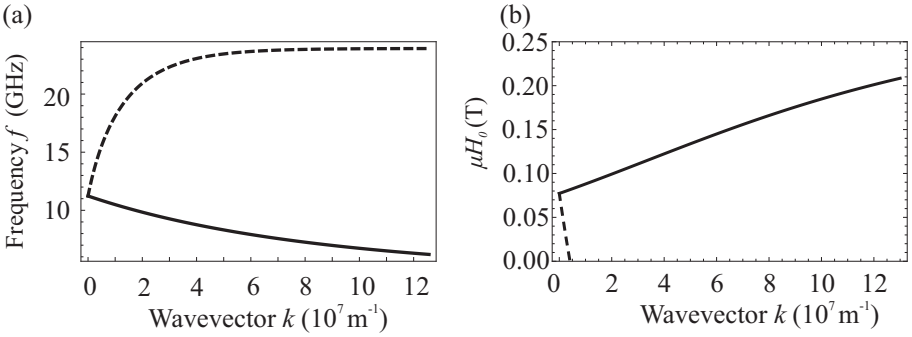

Figure 1.5: The dispersion relation of the uniform film characterized by: $d = 30$ nm, $M_S = 1.2 \cdot 10^6$ A/m, $\gamma = 176$ GHz/T, (a) Frequency as a function of the wave vector, $f(k)$ function for $\mu_0 H_0 = 0.1$ T, (b) Magnetic resonance field in dependence on k $\mu_0 H_0(k)$ for fixed $f = 9.8$ GHz . The dashed line shows the dispersion perpendicular to the in-plane external magnetic field (DE geometry), continuous line presents the dispersion along the bias field (BV geometry).

Properties of the Damon-Eshbach Excitation

A SW excitation propagating perpendicular to the applied magnetic field ($k_y \neq 0$, $k_z = 0$) posses an interesting spatial distributions of dynamic magnetizations across the magnetic film. To plot the relative amplitudes, the normalization is made by assuming $b_2 = 1$ (it means that the value of magnetostatic potential is 1 at the center of the film), the value of a_2 is searched:

$$m_{11} a_2 + m_{12} b_2 = 0, \tag{1.43}$$

since m_{11} is imaginary number and m_{12} is real (see the Eqs. 1.38 and 1.39 for $k_z = 0$), the a_2 will be imaginary. In the considered case also imaginary is the $k_x^i = i|k_y|$, thus in the chosen basis the X^i function is real and might be written in the form of exponential function using Euler's formula:

$$X^i(x) = (a_2 \sin k_x^i x + b_2 \cos k_x^i x) = c_2 e^{i k_x^i x} + d_2 e^{-i k_x^i x}. \tag{1.44}$$

The c_2 and d_2 are coefficients, that can be also calculated with the use of Euler's formula:

$$\begin{aligned} c_2 e^{i k_x^i x} + d_2 e^{-i k_x^i x} &= c_2(\cos k_x^i x + i \sin k_x^i x) + d_2(\cos k_x^i x - i \sin k_x^i x) \\ &= (c_2 + d_2)\cos k_x^i x) + i(c_2 - d_2)\sin k_x^i x. \end{aligned} \tag{1.45}$$

Thus:

$$b_2 = c_2 + d_2, \tag{1.46}$$

$$a_2 = i(c_2 - d_2). \tag{1.47}$$

For $k_y = 1 \cdot 10^7$ 1/m, the value of coefficients are: $c_2 = -1.04$ and $d_2 = 2.04$. These values and equations shows that the magnetostatic potential inside the material is composed of two exponential functions with different coefficient, thus a localization is present at one of the edges, see Fig. 1.6. Further analysis of a_2 functions show that it is even function, $a_2(k_y) = a_2(-k_y)$, leading to symmetric sweep of c_2 and d_2 (if the value of potential is normalized to the same value at the center of the film), what is seen when changing sign in Eq. 1.47. Thus for $k_y = -1 \cdot 10^7$ 1/m, the value of coefficients are: $c_2 = 2.04$ and $d_2 = -1.04$, the localization switch to opposit edge of the film. The a_2 for large k_y and $-k_y$ is converging to 1 and -1 respectively. In that cases either c_2 or d_2 is 0 and due to the Eq. 1.44, the decay is defined by one exponential function.

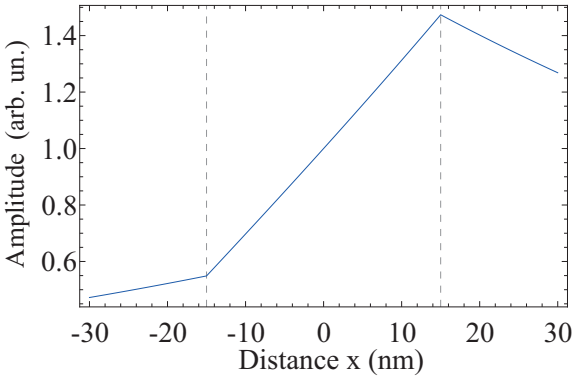

Figure 1.6: The magnetostatic potential as a function of x (thickness) ot the ferromagnetic film for the SW propagating perpendicular to the direction of the external magnetic field. The uniform function is characterized by following parameters: $d = 30$ nm, $M_S = 1.2 \cdot 10^6$ A/m, $\gamma = 176$ GHz/T, $\mu_0 H_0 = 0.1$ T. The wavevector of spin wave is $k_y = 1 \cdot 10^7$ 1/m. The dashed lines indicate the ferromagnetic-dielectric boundaries.

Using the relations defined by the Eqs. 1.17 and 1.21, it can be found that also the magnetization will decrease exponentially:

$$\begin{aligned} m_x &= \kappa(k_x^i(a_2 \cos k_x^i x - b_2 \sin k_x^i x)) + \nu k_y(a_2 \cos k_x^i x + b_2 \sin k_x^i x) \\ &= ik_x^i\kappa(c_2 e^{ik_x^i x} - d_2 e^{-ik_x^i x}) + \nu k_y(c_2 e^{ik_x^i x} + d_2 e^{-ik_x^i x}) \\ &= (ik_x^i\kappa + \nu k_y)(c_2 e^{ik_x^i x}) - (ik_x^i\kappa - \nu k_y) d_2 e^{-ik_x^i x}, \end{aligned} \tag{1.48}$$

$$\begin{aligned} m_y &= ik_y\kappa(a_2 \cos k_x^i x + b_2 \sin k_x^i x) + i\nu(k_x^i(a_2 \cos k_x^i x - b_2 \sin k_x^i x)) \\ &= ik_y\kappa(c_2 e^{ik_x^i x} + d_2 e^{-ik_x^i x}) - \nu(k_x^i(c_2 e^{ik_x^i x} - d_2 e^{-ik_x^i x}) \\ &= (ik_y\kappa - \nu(k_x^i)c_2 e^{ik_x^i x} + (ik_y\kappa + \nu(k_x^i) d_2 e^{-ik_x^i x}. \end{aligned} \tag{1.49}$$

The excitation of this type is called magnetostatic surface wave (or Damon-Eshbach wave), the localization edge is dependent upon the sign of k_y. In the chosen basis (b_2

real), the m_y is imaginary number. In the Fig. 1.7 the $|m_x|$ and $|m_y|$ for $k_y = 1 \cdot 10^7$ 1/m is shown, and confirm SW amplitude localization.

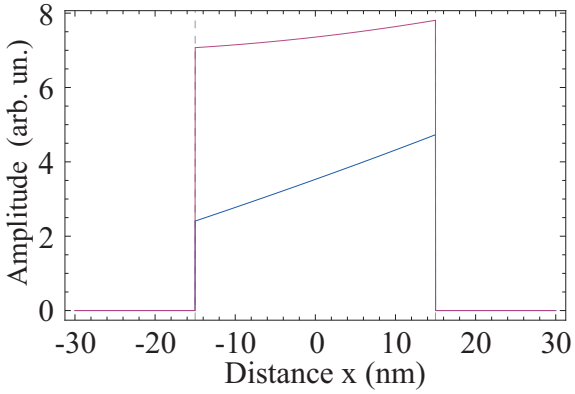

Figure 1.7: The m_x (blue line), m_y (purple line) as a function of x for a ferromagnetic film for SW propagating perpendicular to H_0. The uniform film is characterized by following parameters: $d = 30$ nm, $M_S = 1.2 \cdot 10^6$ A/m, $\gamma = 176$ GHz/T, $\mu_0 H_0 = 0.1$ T. The wavevector of spin wave is $k_y = 1 \cdot 10^7$ 1/m.

1.3 Dipole-Exchange Spin Waves

The exchange interactions influence the solution of the SW excitation spectra. Additional term to the effective field H_{eff}, exchange field describing the exchange interactions, H_{ex} needs to be added:

$$\mathbf{H}_{\text{ex}} = \frac{2}{\mu_0 M_S} \left(\nabla \cdot \frac{A_{ex}}{M_S} \nabla \mathbf{m} \right), \tag{1.50}$$

where A_{ex} is exchange constant which define the interaction strength coefficient.

The governing equations (Eqs. 1.9 and 1.12, where the effective field contributions are H_0 and H_{ex}) can be solved with the use of numerical methods. Under the assumption of the dynamic components and magnetostatic potential in the form of propagating waves ($\varphi(x,y) = \varphi'(x)\mathrm{e}^{i(k_y y + k_z z)}$, where $\varphi' = m'_x$, m'_y and ψ'_x) leads to the following:

$$\begin{pmatrix} \frac{i2\pi f}{\gamma\mu_0} & H_0 - k_y^2 M_S \left(\frac{2A_{ex}}{M_S\mu_0}\right) - k_z^2 M_S \left(\frac{2A_{ex}}{M_S\mu_0}\right) - M_S \frac{\partial}{\partial x}\left(\frac{2A_{ex}}{M_S\mu_0}\frac{\partial}{\partial x}\right) & ik_y M_S \\ -H_0 + k_y^2 M_S \left(\frac{2A_{ex}}{M_S\mu_0}\right) + k_z^2 M_S \left(\frac{2A_{ex}}{M_S\mu_0}\right) - M_S \frac{\partial}{\partial x}\left(\frac{2A_{ex}}{M_S\mu_0}\frac{\partial}{\partial x}\right) & \frac{i2\pi f}{\gamma\mu_0} & -M_S \frac{\partial}{\partial x} \\ \frac{\partial}{\partial x} & ik_y & -k_y^2 - k_z^2 + \frac{\partial^2}{\partial x^2} \end{pmatrix} \begin{pmatrix} m'_x \\ m'_y \\ \psi' \end{pmatrix} = 0. \tag{1.51}$$

This set of equations can be solved with the use of finite element method, described further in the chapter 3.

The results of calculations for the 30 nm Co film with taken exchange interaction into account is plotted in the Fig. 1.8 ($d = 30$ nm, $M_S = 1.2 \cdot 10^6$ A/m,

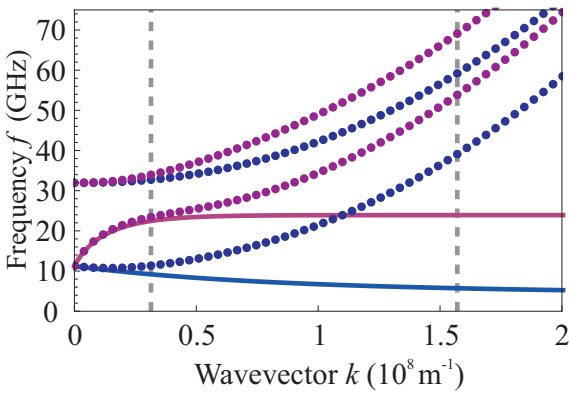

Figure 1.8: The dispersion relation for a uniform film characterized by parameters: $d = 30$ nm, $M_S = 1.2 \cdot 10^6$ A/m, $\gamma = 176$ GHz/T and $\mu_0 H_0 = 0.1$ T. The exchange constant is varied $A_{ex} = 2.8 \cdot 10^{-11}$ J/m (dots) amd $A_{ex} = 0$ J/m (solid lines). Blue line and blue dots shows BV geometry without and with exchange interaction respectively. Purple line and purple dots shows DE geometry without and with exchange interaction respectively. The grid lines divide the dispersion into three regions: i) long wavelength $k < 0.35 \cdot 10^8$ 1/m, where dipole interactions are determining the dispersion relation, ii) intermediate wavelength, $0.35 \cdot 10^8$ 1/m$< k < 1.55 \cdot 10^8$ 1/m, where dipole and exchange are of similar strength, iii) short wavelength $k > 1.55 \cdot 10^8$ 1/m, where exchange interactions are determining the dispersion relation.

$A_{ex} = 2.8 \cdot 10^{-11}$ J/m, $\gamma = 176$ GHz/T, $\mu_0 H_0 = 0.1$ T) and in the Fig. 1.9 (for $d = 60$ nm). If these dispersions are compared with the dispersions obtained without taking the exchange interactions into account, the exchange shift is present in both directions of propagation. In addition, 3 regions can be differentated, dipole (range of k wavevectors where the exchange has no significant influence), dipole exchange (where both interactions are comparable), exchange (where dispersion takes characteristic parabolic exchange form).

Additional influence of exchange is appearing for standing modes (quantized modes across the thickness of the film). The interaction of standing and main mode might be present, providing the hybridization between these two modes. The exponential decay of the DE mode is modified and can be even changed if the interaction with standing modes is strong. The spatial distribution of $|m'_x|$ and $|m'_y|$ of main dispersion branch is also changing when the exchange interactions are included into calculations.. It might even change the localization near region interacting with quantized modes as was reported in the Ref. [38].

1.4 Magnonic Crystals

In analogy to the electronic structures and photonic crystals (PCs are materials that possesses periodic index of refraction), a magnonic crystals might be defined. By

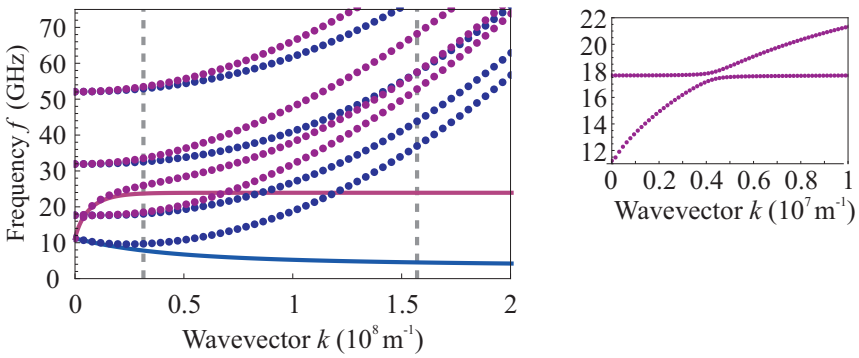

Figure 1.9: The dispersion relation for a uniform film characterized by parameters: $d = 60$ nm, $M_S = 1.2 \cdot 10^6$ A/m, $\gamma = 176$ GHz/T and $\mu_0 H_0 = 0.1$ T. The exchange constant is varied $A_{ex} = 2.8 \cdot 10^{-11}$ J/m (dots) amd $A_{ex} = 0$ J/m (solid lines). Blue line and blue dots shows BV geometry without and with exchange interaction respectively. Purple line and purple dots shows DE geometry without and with exchange interaction respectively. The grid lines divide the dispersion into three regions: i) long wavelength $k < 0.35 \cdot 10^8$ 1/m, where dipole interactions are determining the dispersion relation, ii) intermediate wavelength, $0.35 \cdot 10^8$ 1/m$< k < 1.55 \cdot 10^8$ 1/m, where dipole and exchange are of similar strength, iii) short wavelength $k > 1.55 \cdot 10^8$ 1/m, where exchange interactions are determining the dispersion relation. The inset shows the interaction of dipole and perpendicular standing spin wave.

MC it is meant artificially made structures composed of periodically arranged ferromagnetic materials (it can be of various magnetizations or structural parameters) with its influence on the collective spin-wave dynamics [39]. In periodic structures, a new physical phenomenons arise, i.e., spatial confinement, localization of modes or completely prohibited propagation of wave at some range of frequencies, i.e., band gaps. The MCs have been subject of the intensive theoretical, experimental and application studies in solid state physics and magnetism for last years.

The research in MCs is an important part of magnonics, a sub-field of condensed matter physics which explores spin waves in magnetic materials. The vast spectrum of applications of magnonics devices includes, among others, non-volatile magnetic storage devices that will bring closer to the construction of programmable devices with sub-nanosecond re-programming time.[15, 40, 41] Magnonics technology is also regarded as an alternative to the silicon-based logic-gate technology. [3, 42, 43] These potential applications are followed by the design of magnonic devices that will allow the control of spin waves and information processing as spin-wave interferometers of the Mach-Zehnder type, [44, 45] enhancement of the signal-to-noise ratio, reduction or suppression of high-power signals, and power-dependent phase shift.[46]

Another important part of the research in magnonics is focused on the interaction of spin waves with electromagnetic waves especially in the microwave regime. Magnonic crystals can be used as materials with a negative refractive index

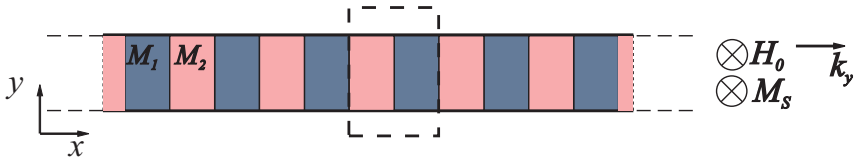

Figure 1.10: The 1D MC composed of alternating ferromagnetic slabs characterized by the saturation magnetizations M_1 and M_2. The dashed rectangular indicates the unit cell that is taken in the numerical calculations.

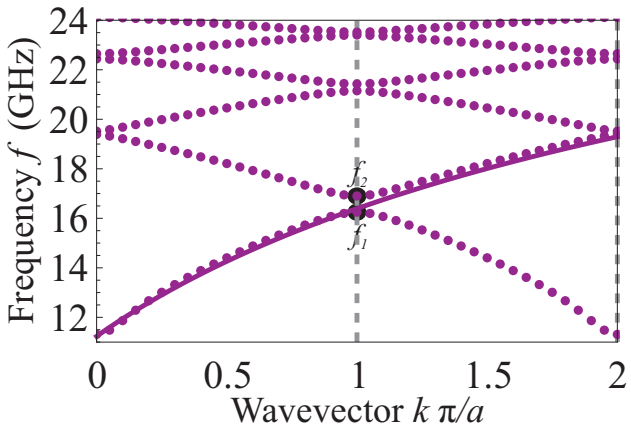

Figure 1.11: The dispersion relation of 1D MC composed of two materials with the saturation magnetizations $M_1 = 1.15 \cdot 10^6$ A/m and $M_2 = 1.25 \cdot 10^6$ A/m. The lattice constant is $a = 500$ nm, the film thickness $d = 30$ nm, the stripe widths $w = 250$ nm, the exchange coefficient $A_{ex} = 2.88 \cdot 10^{-11}$ J/m. In addition, solid line shows the dispersion of uniform film with saturation magnetization $M_{\text{avrg}} = 1.2 \cdot 10^6$ A/m.

(NRI) for electromagnetic waves in the high-frequency regime, or as zero refractive index medias, i.e., MCs can be regarded as metamaterials for electromagnetic waves.[47, 48, 49] The properties of NRI materials and their potential application in cloaking devices or perfect lenses are studied extensively.[50, 51] Materials with a refractive index close to zero could be used for squeezing electromagnetic energy into an ultra-narrow channel.[52]

The various numerical methods have been implemented for calculations of the SW dynamics in periodic structures. In this thesis, it is considered a special case of MCs, i.e., an one-dimensional MC composed of alternating ferromagnetic slabs with finite thickness and width, see Fig. 1.10. In results presented in this thesis, the plane wave method and finite element method (FEM) have been used to solve the problem in the frequency domain. In both cases, the solution of SWs is assumed in the form of monochromatic Bloch wave:

$$\phi(\mathbf{r}) = \phi'(\mathbf{r}) \mathrm{e}^{i\mathbf{k}\cdot\mathbf{r}} \tag{1.52}$$

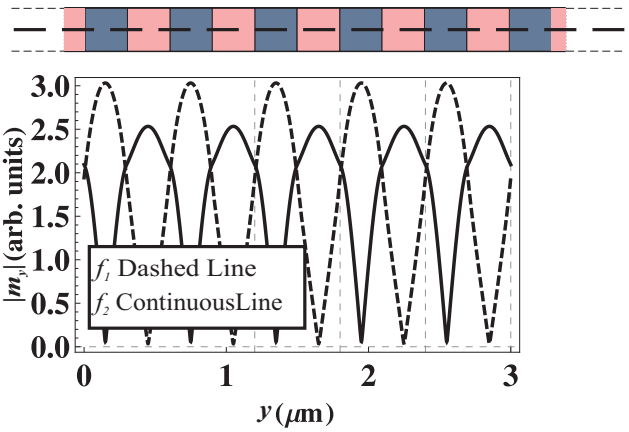

Figure 1.12: The distribution of the $|m_y|$ component of the magnetization vector at $x = \frac{d}{2}$ along the y direction. The localization at low/high magnetic potentials is seen for low/high frequency modes, f_1 and f_2 marked in the dispersion relation in Fig. 1.11.

where $\phi = m_x, m_y, \psi$. This allows to define a set of equations with $\phi'(\mathbf{r})$ eigen functions and ω eigenvalues. According with the Bloch theorem $\phi'(\mathbf{r})$ functions are periodic functions of the position vector which allows for performing efficient calculation in the unit cell with periodic boundary conditions (PBC), see Fig. 1.10.

The results of calculation shown in Fig. 1.11, presents the common effects known for dispersion relation in periodic structures, i.e., band folding, band gap opening and in analogies to nearly free electron model, localization of a wave amplitude in low/high potential wells for the modes near the band gap edges (Fig. 1.12). These properties are useful for designing functional devices, filters, circulators. Some of these properties will be discussed further within the dissertation according with the objectives of my thesis, i.e., observation of standing spin waves or design of metamaterials with effective properties due to these quantization.

Chapter 2

Experiment

Among the experimental methods aiming to measure the SWs and characterize their properties, we can differentiate such as: ferromagnetic resonance (FMR), vector analysis or Brillouin ligh scattering spectroscopy (BLS). These examples of measurement techniques are either compared with numerical results presented in the thesis or were used to verify the models. Each of the method is complementary and provide various data for analysis. The FMR setup is used to characterize the interaction of SWs with electromagentic wave at GHz range and measure standing spin waves frequencies and the damping parameter that are analyzed in the chapter 4. The vector network analyzer is a technique used for measuring transmission of the signal, it is widely use for studying forbidden gaps in micrometer size MCs. A BLS can characterize full dispersion of the thin films. The full Brillouin zone of MC can be characterized, if the periodicity is below nanometers. This chapter describes these techniques in details.

2.1 Ferromagnetic Resonance

An FMR spectrometer is use to characterize the absorption of the electromagnetic (EM) wave of the ferromagnetic material as function of the external static magnetic field [53]. The schema of the FMR measurement setup is depicted in the Fig. 2.1. The main elements of the device are the microwave source, microwave cavity, magnet and detector.

The microwave source is operating at fixed frequency at microwave range, i.e., at frequency of the cavity resonant excitation. The wave is transported by transmission line to the cavity, passing by the circulator. At the fixed frequency standing EM wave is formed within the cavity, since the size of the cavity is choose accordingly with the wavelength of generated wave. The EM field emitted by the cavity is passing back by the circulator to detector. The induced voltage in the transmission is analyzed and the power of absorption might be measured.

The magnetic external field is controlled and swept in the experiment. If the

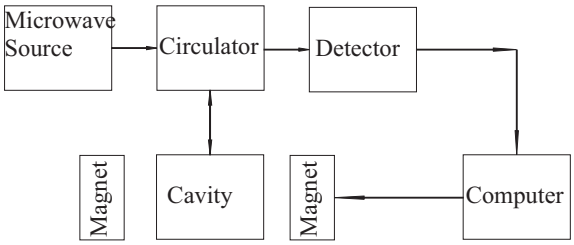

Figure 2.1: The schema of the FMR measurement setup.

frequency of EM wave and the external field correspond to the frequency of the mode that is effectively excited, the spin wave mode absorbs the energy from the EM field. In general EM in the cavity can excite standing spin wave oscillations if the overlapping integral of oscillating EM field and spin wave mode is nonzero.

To determine the response of the magnonic structure to an external uniform alternating magnetic field $\mathbf{b}(t)$ the problem of coupling of this field to the eigenmodes is considered. The spatial distribution of the dynamic components of the magnetization vector of the spin wave modes allows to calculate the relative intensity of the corresponding absorption peaks. The time-averaged absorption power $P_n(\mathbf{r})$ associated with the n-th mode at a particular point $\mathbf{r}$ is given by:

$$P_n(\mathbf{r}) = -\frac{1}{T}\int_0^T \mathbf{m}_n^*(\mathbf{r},t)\cdot\frac{\mathrm{d}\mathbf{b}(t)}{\mathrm{d}t}\,\mathrm{d}t, \tag{2.1}$$

where $\mathbf{m}_n$ is an amplitude of the dynamic magnetization compontent of the standing spin wave, T is the period of the magnetic field oscillations. By averaging $P_n(\mathbf{r})$ over the entire of the ferromagnetic material the absorbed power by the the excitation is obtained:

$$\langle P(\mathbf{r})\rangle = \frac{1}{V}\int_V P_n(\mathbf{r})\,\mathrm{d}V, \tag{2.2}$$

where V denotes the volume of the magnetic material. Thus, the relative efficiency of the interaction of the external uniform alternating magnetic field with the spin waves can be defined for each mode.

The excitation of spin precession results in absorption of the EM wave, thus observed as a change by the detector. Although optimization of cavities, this signal is weak. In order to increase signal to noise ration, lock-in amplifier is used [53] and supplemented with small modulations of external magnetic field.

The small modulating bias field component might be applied in addition to constant field:

$$H(t) = H_0 + H_a cos(\omega t) \tag{2.3}$$

where ω is certain frequency at range of hundreds KHz. The reference voltage signal V_{ref} is:

$$V_{ref} = cos(\omega t + \phi). \tag{2.4}$$

The Taylor expansion at H_0 of the FMR voltage signal V_{FMR} is:

$$V_{FMR}(H) = V_{FMR}(H_0) + \left.\frac{dV_{FMR}}{dH}\right|_{H=H_0} H_a cos(\omega t) + ... \tag{2.5}$$

The product:

$$\begin{aligned} V_{FMR}(H)V_{ref} &= V_{FMR}(H_0)cos(\omega t + \phi) + \left.\frac{dV_{FMR}}{dH}\right|_{H=H_0} H_a cos(\omega t)cos(\omega t + \phi) \\ = V_{FMR}(H_0)cos(\omega t + \phi) &+ \frac{1}{2}\left.\frac{dV_{FMR}}{dH}\right|_{H=H_0} H_a cos(\phi) + \frac{1}{2}\left.\frac{dV_{FMR}}{dH}\right|_{H=H_0} H_a cos(2\omega t + \phi) \end{aligned} \tag{2.6}$$

Applying low pass filters, only the second term is nonzero. These result in presenting the derivation of the signal in respect to swept field. The example of measurement data for a thin bicomponent ferromagnetic film (Co and Py) is presented in the Fig. 2.2 and will be analyzed in details in the chapter 4. The value of damping parameter characteristic for specific material can be extracted from the measured data. It is related with the halfwidth of the peak in absorption intensity-field characteristic, see chapter 4.3.

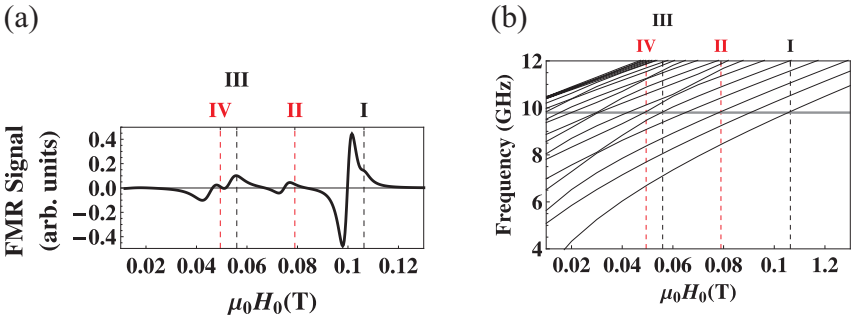

Figure 2.2: (a) An example of the FMR derivative signal. The data measured and shared by V. K. Sakharov from Kotelnikov Institute of Radio Engineering and Electronics, Saratov branch, Russian Academy of Sciences. (b) Calculated dependence of the spin wave frequency as a function of the external magnetic field ($f(H_0)$) of $k = 0$ modes for corresponding MCs, that will be described in the chapter 4.

2.2 Network Analysis

A spin waves can be excited and investigated by the network analysis. The network analysis is a complex instrument developed for characterization of passive and active elements of devices, e.g., filters, couplers, circulators, waveguides or resonators [54, 55]. The attenuation of the signal passing through a device, might be measured with Scalar Network Analyzer, SNA. However, in some cases, in addition to information about the attenuation of the magnitude of the signal, the phase information is

needed. A device that is able to measure both magnitude and phase of signal is Vector Network Analyzer (VNA). The phase measurements requires the comparison of signal passing through the device under test (DUT) and the reference signal, see Fig. 2.3.

A schematic overview of the VNA is shown in the Fig. 2.3. An input microwave current is produced in the port 1, generating the electromagnetic field in its surrounding. The transmission properties of the field through the DUT is analyzed by the port 2, where the field induce microwave current. The scattering parameters S are introduced in order to define the transmission or reflection coefficients. At the same time they allow to avoid measurements of total voltage and current.

A source of microwave generates a microwave signal at the measurement frequency. The signal is split into two: the reference signal and the signal directed to the DUT (at port 1 or 2). The local oscillator is locked with the frequency of the measurement. The received signal at detector is mixed with the reference signal and down-converted to low intermediate frequency. Then the magnitude and phase difference is analyzed (taking into account delay due to difference in path lengths). However, in the experiment the difference between cycles of wave cannot be made, thus phase frequency characteristic is reduced to $\pm 180\,\mathrm{deg}$.

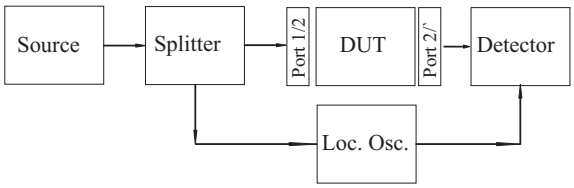

Figure 2.3: The schema of the Vector Network Analyser measurment setup.

Solutions of the equations governing the voltage and current characteristic in the transmission line can be written in the form of the propagating waves [56]:

$$V_i(x) = V_i^+ e^{-\gamma x} + V_i^- e^{\gamma x}, \tag{2.7}$$

$$I_i(x) = I_i^+ e^{-\gamma x} + I_i^- e^{\gamma x}, \tag{2.8}$$

where V_i^+, V_i^-, I_i^+ and I_i^- are amplitudes of voltage and current wave respectively. The γ is a propagation constant. Thus, incident and reflected power waves are defined as [57]:

$$a_i = \frac{1}{2}\frac{V_i + Z_{Ci} I_i}{\sqrt{|Re(Z_{Ci})|}}, \tag{2.9}$$

$$b_i = \frac{1}{2}\frac{V_i - Z_{Ci}^* I_i}{\sqrt{|Re(Z_{Ci})|}}, \tag{2.10}$$

where Z_{Ci} is the characteristic impedance:

$$Z_{Ci} = \frac{V_i^+}{I_i^-}. \tag{2.11}$$

The a_i and b_i are depicted on the Fig. 2.4.

The S parameters defines the relation between incident and reflected power waves:

$$\begin{pmatrix} b_1 \\ b_2 \end{pmatrix} = \begin{pmatrix} S_{11} & S_{12} \\ S_{21} & S_{22} \end{pmatrix} \begin{pmatrix} a_1 \\ a_2 \end{pmatrix}. \tag{2.12}$$

Figure 2.4: The incident and reflected waves passing through the Device Under Test (DUT).

If the port 2 is terminated with a load that impedance is equal to the impedance of the system, a_2 is zero and:

$$S_{11} = \frac{V_1^-}{V_1^+} \tag{2.13}$$

is the input port voltage reflection coefficient

$$S_{21} = \frac{V_2^-}{V_1^+} \tag{2.14}$$

is the reverse voltage gain.

If the port 1 is terminated with a load that impedance is equal to the impedance of the system, a_1 is zero and:

$$S_{12} = \frac{V_1^-}{V_2^+} \tag{2.15}$$

is the forward voltage gain

$$S_{22} = \frac{V_2^-}{V_2^+} \tag{2.16}$$

is the output port voltage reflection coefficient.

Two important transmission lines are used in the measurements of transmission due to SW excitations, i.e., microstripe antenna and coplanar antenna, see Fig. 2.5. The field produced by these two kinds of antennas is significantly different. In case of microstripe antenna the conducting plate is separated by dielectric from the ground plate. In case of coplanar antenna, the ground stripes are in the same plane as conductor.

An example of the measurements done with microstripe antennas are plotted in the Figs 2.6. The increase of transmission signal is observed above frequency $f \approx f_{FMR}$ indicating that excited SW are responsible for enhanced transmission. In addition, narrow ranges of frequency above f_{FMR} are observed where transmission is not enhanced. The measured sample is a MC, and the low transmission ranges are due to the presence of frequency band gap. The analysis of phase-frequency

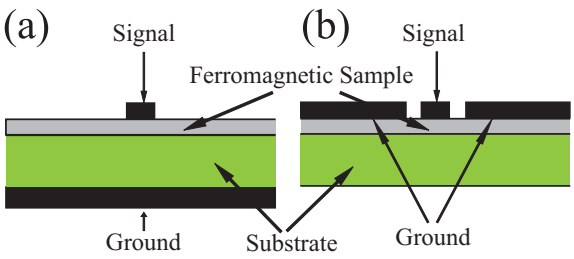

Figure 2.5: The crosssection of transmission lines (a) microstripe line and (b) coplanar waveguide.

characteristic, PFC allow for estimation of dispersion relation, confirming that gap in transmission is present at wavevector corresponding to Brillouin zone border of measured MCs. Further about comparison of the VNA measurements with theoretical calculation will be presented in the chapter 6

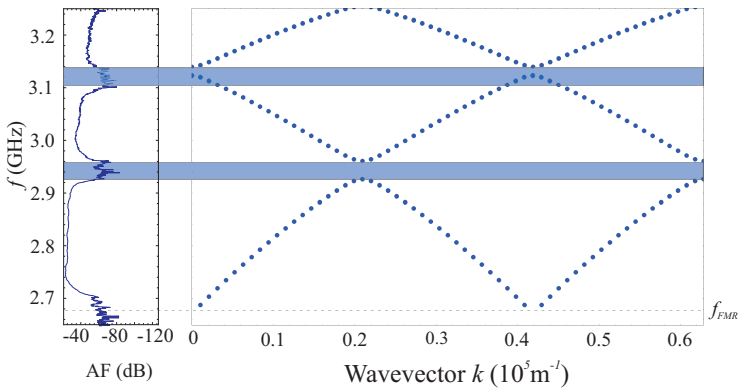

Figure 2.6: An example of the measured enhanced transmission due to the SW excitation. The data measured and shared by S. L. Vysotskii from Kotelnikov Institute of Radio Engineering and Electronics, Saratov branch, Russian Academy of Sciences. The measured data is compared with the calculated dispersion.

2.3 Brillouin Light Scattering

The fore-mentioned measurements setup in GHz regime are strongly supplemented byt the results of the Brillouin Light Scattering measurements [58, 59]. This method allows for measuring the frequencies as a function of the wavevector values. In addition, the excitation of spin waves is not necessary, thermal excitations can be measured. The spatial resolution is high, determined by the size of the laser focus beam $30 - 50$ μm [58]

The principle of BLS experiment is following, the generated photons interact with spin waves. The scattered photon can gain/loose energy and momentum due

to the spin wave annihilation/creation:

$$\hbar\omega_{P,S} = \hbar(\omega_{P,I} \pm \omega_{SW}), \tag{2.17}$$

$$\hbar k_{P,S} = \hbar(k_{P,I} \pm k_{SW}), \tag{2.18}$$

where ω_{SW}, $\omega_{P,I}$ and $\omega_{P,S}$ are frequencies of spin wave, incident and scattered photon respectively. The k_{SW}, $k_{P,I}$ and $k_{P,S}$ are wavevectors of spin wave, incident and scattered photon respectively. The Fig. 2.7 shows the scattering of photon and spin wave annihilation/creation.

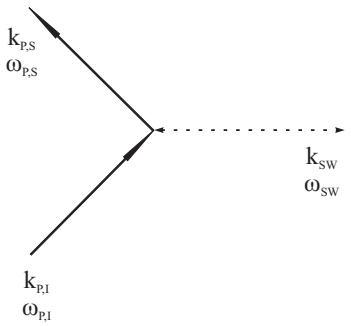

Figure 2.7: The annihilation/creation of the magnon in light scattering process.

The source of the light is usually the green line of an Ar^+ laser of 514.5 nm wavelenght. Only the in-plane components of the wavevectors undergo the conservation condition, for the light scattered on the film. If $k_{P,I} = -k_{P,S}$ (back-scattering geometry), the parallel wavevector of SW is defined by the incident angle θ:

$$k_{||} = 2k_{P,I}sin(\theta). \tag{2.19}$$

The perpendicular component of the photon wavevector $k_\perp$ is not well defined due to the symmetry of the structure, the uncertainty is negligible if $(k_{SW} - k_{P,I})d >> 2\pi$, where d is the thickness of the film.

Changing the incident angle θ, the determined value of spin wave wavevector $k_{||}$ is varied also. The frequency absorption characteristic might be collected in the BLS measurement for various wavevectors, showing peaks at frequencies of SW modes. The full dispersion characteristic of SW in thin films can be measured.

Chapter 3

Numerical Methods

The band structure of excitations in materials with discrete translational symmetry, including electronic, photonic, phononic and magnonic crystals, can be calculated with the similar nuerical calculations methods. These methods are applicable for various geometries and are applicable to any type of periodic arrangement structures. [60, 61, 62, 7, 63] Most of these numerical methods has also been used to calculate spin-wave spectra of 1D and 2D MCs of finite thickness. [64, 65, 66]

A global coordinate system is defined, in which the y- and z-axes define the plane of the MC, and the x-axis is normal to its surface. In the continuous medium approach, the spin-wave dispersion relation is determined from the Landau-Lifshitz Eq. 1.9. MC is assumed to be magnetized to saturation and time dependance of parallel to field magnetization component is neglected (linearization, see Eq. 1.14).

Effective magnetic field $\mathbf{H}_{\text{eff}}$ acting on the magnetization in an MC is the sum of several components, such as external, exchange, demagnetizing or anisotropy fields. However, here only three should be considered: a uniform and constant applied magnetic field $\mathbf{H}_0$ (along the z-axis), the exchange field $\mathbf{H}_{\text{ex}}$ and the magnetostatic field $\mathbf{H}_{\text{ms}}$. The latter two fields, i.e., the exchange field and the magnetostatic field, are space-dependent:

$$\mathbf{H}_{\text{eff}}(\mathbf{r}, t) = \mathbf{H}_0 + \mathbf{H}_{\text{ex}}(\mathbf{r}, t) + \mathbf{H}_{\text{ms}}(\mathbf{r}, t). \tag{3.1}$$

The exchange field in uniform materials has the well known form.[67, 68] But in MCs the magnetization changes abruptly at interfaces and a reformulation of the exchange field term is required to spectral methods. In the literature different formulations of the exchange field were proposed for calculations of the SW spectra in MCs so far.[69, 70, 7] Each formulation introduces different boundary conditions on dynamical components of the magnetization vector, so can describe different physical situations on interfaces. The exchange field is assumed to have the form that can be obtained directly from the exchange-energy functional in the linear

approximation with sharp interfaces:

$$\mathbf{H}_{\mathrm{ex}}(\mathbf{r},t) = \frac{1}{M_{\mathrm{S}}}\left(\nabla \cdot \frac{2A_{ex}(\mathbf{r})}{\mu_0 M_{\mathrm{S}}(\mathbf{r})}\nabla\right)\mathbf{m}(\mathbf{r},t). \tag{3.2}$$

In magnetically inhomogeneous materials, the spatial inhomogeneity of both the exchange constant $A_{ex}(\mathbf{r})$ and the spontaneous magnetization $M_{\mathrm{S}}(\mathbf{r})$ must be taken into account in the definition of the exchange field.

The last component of the effective magnetic field in the Eq. 3.1, the magnetostatic field is calculated by decomposing this field into the static and dynamic components, $\mathbf{H}_{dem}(\mathbf{r})$ and $\mathbf{h}(\mathbf{r},t)$, respectively. When the magnetic stripes are infinitely long $\mathbf{H}_{dem}(\mathbf{r}) = 0$. The time dependence of the dynamic magnetostatic field has the same form as that of the dynamic component of the magnetization vector: $\mathbf{h}(\mathbf{r},t) = \mathbf{h}(\mathbf{r})\mathrm{e}^{i\omega t}$.

Using the linear approximation, the following system of equations from (1.9) is derived:

$$i\frac{\omega}{\gamma\mu_0}m_x(\mathbf{r}) + \left(\nabla \cdot \frac{2A_{ex}(\mathbf{r})}{\mu_0 M_{\mathrm{S}}(\mathbf{r})}\nabla\right)m_y(\mathbf{r}) - m_y(\mathbf{r})H_0 + M_{\mathrm{S}}(\mathbf{r})h_y(\mathbf{r}) = 0, \tag{3.3}$$

$$i\frac{\omega}{\gamma\mu_0}m_y(\mathbf{r}) - \left(\nabla \cdot \frac{2A_{ex}(\mathbf{r})}{\mu_0 M_{\mathrm{S}}(\mathbf{r})}\nabla\right)m_x(\mathbf{r}) + m_x(\mathbf{r})H_0 - M_{\mathrm{S}}(\mathbf{r})h_x(\mathbf{r}) = 0. \tag{3.4}$$

A_{ex} and M_{S} are periodic functions of y for 1D MC with the periodicity along y and constant across the film thickness. In MCs composed of two materials, each of these material parameters can be expressed by two values, A_{A}, A_{B} and $M_{\mathrm{S,A}}$, $M_{\mathrm{S,B}}$, corresponding to each constituent material.

3.1 Plane Wave Method

To solve the system of equations (3.3)-(3.4), the Bloch's theorem is applied:

$$\mathbf{m}(y) = \sum_G \mathbf{m}_k(G)e^{i(k+G)y}, \tag{3.5}$$

where G denotes a reciprocal lattice vector along direction of periodicity: $G = \frac{2\pi}{a}n_y$; n_y is an integer. Bloch wave vector k refers to those spin waves that, according to Bloch's theorem, can be limited to the first Brillouin Zone (1BZ). Already in Eq. 3.5 limits the solutions to the uniform ones across the film thickness.

In the next step, the Fourier transformation is performed to map the periodic functions M_{S} and $\frac{2A_{ex}(y)}{\mu_0 M_{\mathrm{S}}(y)}$ to the reciprocal space, as

$$M_{\mathrm{S}}(y) = \sum_G M_{\mathrm{S}}(G)e^{iGy}, \qquad \frac{2A_{ex}(y)}{\mu_0 M_{\mathrm{S}}(y)} = \sum_G \frac{2A_{ex}(G)}{\mu_0 M_{\mathrm{S}}(G)}e^{iGy}. \tag{3.6}$$

In the 1D case, the Fourier components of the saturation magnetization $M_{\mathrm{S}}(G)$ and the $\frac{2A_{ex}(y)}{\mu_0 M_{\mathrm{S}}(y)}$ can be calculated analytically:

$$M_{\mathrm{S}}(G) = -\frac{1}{a}\int_0^a M_{\mathrm{S}}(y)e^{-iGy}\mathrm{d}y, \tag{3.7}$$

$$\frac{2A_{ex}(G)}{\mu_0 M_{\mathrm{S}}(G)} = -\frac{1}{a}\int_0^a \frac{2A_{ex}(y)}{\mu_0 M_{\mathrm{S}}(y)}e^{-iGy}\mathrm{d}y. \tag{3.8}$$

The formula for the dynamic demagnetizing fields, $h_x(y,x)$ and $h_y(y,x)$ is needed. According to the idea presented in Ref. [71], for a slab of a 2D magnonic crystal with a uniform magnetization along its thickness (its static and dynamic components) Maxwell's equations can be solved in the magnetostatic approximation with the electromagnetic boundary conditions at both surfaces of the slab, i.e., at $x = -d/2$ and $x = d/2$ (d is a thickness of the MC). For the considered structure, infinite in the (y,z) plane, analytical solutions in the form of Fourier series can be obtained for dynamic demagnetizing fields:

$$\begin{aligned} h_y(y,x) &= \sum_G \left[im_{x,k}(G)\sinh\left(|k+G|x\right)\mathrm{e}^{-|k+G|d/2}\right. \\ &- \left. m_{y,k}(G)\left(1-\cosh\left(|k+G|x\right)\mathrm{e}^{-|k+G|d/2}\right)\right]\mathrm{e}^{i(k+G)y}; \end{aligned} \tag{3.9}$$

$$\begin{aligned} h_x(y,x) &= \sum_G \left[im_{y,k}(G)\sinh\left(|k+G|x\right)\mathrm{e}^{-|k+G|d/2}\right. \\ &- \left. m_{x,k}(G)\cosh\left(|k+G|x\right)\mathrm{e}^{-|k+G|d/2}\right]\mathrm{e}^{i(k+G)y}. \end{aligned} \tag{3.10}$$

Represented in the reciprocal space for the in-plane components, these formulas for the demagnetizing fields are x-dependent, i.e., vary with position across the thickness of the slab. However, when the slab is thin enough (which is the case for the discussed MC, with $d = 5$ nm), the nonuniformity of the demagnetizing fields across its thickness can be neglected, and the respective field values calculated from equations (3.9)-(3.10) for $x = 0$ can be used in the PWM calculations. Because of its Fourier series form, the solution found for the demagnetizing fields can be used directly in the equations (3.3)-(3.4), together with the Bloch theorem, Eq. 3.5.

The substitution of equations (3.5)-(3.10) into (3.3)-(3.4) leads to the algebraic eigenvalue problem with eigenvalues $i\omega/\gamma\mu_0 H_0$:

$$\hat{M}\mathbf{m}_k = i\frac{\omega}{\gamma\mu_0 H_0}\mathbf{m}_k, \tag{3.11}$$

where the eigenvector is $\mathbf{m}_k^{\mathrm{T}} = [m_{x,k}(G_0),\cdots,m_{x,k}(G_N),m_{y,k}(G_0),\cdots,m_{y,k}(G_N)]$ and a finite number N of reciprocal lattice vectors is used in Fourier series (3.5) and (3.6). The elements of matrix $\hat{M}$ are defined as:

$$\hat{M} = \begin{pmatrix} \hat{M}^{xx} & \hat{M}^{xy} \\ \hat{M}^{yx} & \hat{M}^{yy} \end{pmatrix}. \tag{3.12}$$

The submatrices in Eq. 3.12 are defined as:

$$\hat{M}_{ij}^{xx} = -\hat{M}_{ij}^{yy} = -i\frac{1}{H_0}S(k+G_j)M_{\mathrm{S}}(G_i-G_j), \tag{3.13}$$

$$\begin{aligned}\hat{M}_{ij}^{xy} &= \delta_{ij} + \sum_l \frac{(k+G_j)(k+G_l)}{H_0} l_{\mathrm{ex}}^2 (G_l-G_j)M_{\mathrm{S}}(G_i-G_l) \\ &+ \frac{1}{H_0}(1-C(k+G_j,x))M_{\mathrm{S}}(G_i-G_j),\end{aligned} \tag{3.14}$$

$$\begin{aligned}\hat{M}_{ij}^{yx} &= -\delta_{ij} - \sum_l \frac{(k+G_j)\cdot(k+G_l)}{H_0} l_{\mathrm{ex}}^2 (G_l-G_j)M_{\mathrm{S}}(G_i-G_l) \\ &- \frac{1}{H_0}C(k+G_j,x)M_{\mathrm{S}}(G_i-G_j),\end{aligned} \tag{3.15}$$

where indexes of the reciprocal lattice vectors i, j, l are integer numbered reciprocal lattice vectors. The additional functions used in above equations are defined as follows:

$$\begin{aligned}S(k,x) &= \sinh(|k|x)\mathrm{e}^{-|k|d/2}; \\ C(k,x) &= \cosh(|k|x)\mathrm{e}^{-|k|d/2}.\end{aligned} \tag{3.16}$$

The system of Eqs. 3.11 is solved by standard numerical procedures designed for solving complex matrix eigenvalue problems. All the eigenvalues found by these procedures must be tested for convergence, though. A satisfactory convergence of numerical solutions of Eq. 3.11 for all the structures considered proves to be assured by the use of 101 reciprocal lattice vectors. The model presented here has been validated by comparison with other numerical simulations and experimental results for MCs composed of Co and permalloy stripes, for details see Ref. [64].

The PWM will be used in the chapter 5. It is an effective method in the cases where the uniform excitation across the thickness of the film can be assumed. In next section, the FEM will be presented.

3.2 Finite Element Method

The FEM method is a tool that leads to approximate solutions of differential problem. It allow for calculation of structures that nonuniformity over the thickness of the film is strong and also for calculations of structures that are nonuniform across the thickness. The backdraw of this calculation as compare to PWM calculation is the computational time. Another dimension required to define structure expand largely the degrees of freedom

Although the 1D problem can be defined and solved with the use of programming environment (C++, MatLab, Mathematica). The 2D and 3D geometries will most probably required implementation of advanced techniques (e.g. unstructured grid, high order polynomial discretionary, iterative methods to solve matrix), thus

specialized software is common to use. Here the COMSOL software for that purpose is used.

The procedure of FEM might be defined as follows:

- Defining a physical problem
- Defining the governing equations in the weak formulation
- Discretization
- Setting up the matrix
- Defining the boundary conditions
- Solving the matrix

In this part only the physical problem will be defined for magnonic calculations. The following steps of FEM procedure are presented for simply example of 1D photonic crystal in the Appendix A.

The effective magnetic field in the Eq. 1.9 is defined as:

$$\mathbf{H}_{\text{eff}} = \mathbf{H}_0 + \mathbf{H}_{\text{ex}} + \mathbf{H}_{\text{ms}}, \tag{3.17}$$

where $\mathbf{H}_0$ is the external static magnetic field; $\mathbf{H}_{\text{ms}}$ is the magnetostatic field with two components: a static demagnetizing component: H_{dem} (present only in BV geometry) and dynamic components that are perpendicular to $\mathbf{H}_0$: $h_{\text{dem,x}}$, $h_{\text{dem,y}}$ (in DE geometry) and h_{y}, h_{z} (in BV geometry); $\mathbf{H}_{\text{ex}}$ is the exchange field. In the DE and BV geometries the exchange field is:

$$\mathbf{H}_{\text{ex, DE}} = \begin{pmatrix} Q_x \\ Q_y \\ 0 \end{pmatrix} \quad \text{and} \quad \mathbf{H}_{\text{ex, BV}} = \begin{pmatrix} 0 \\ Q_y \\ Q_z \end{pmatrix}, \tag{3.18}$$

where:

$$Q_x = \frac{2}{\mu_0 M_{\text{S}}} \left(\nabla \cdot \frac{A_{ex}}{M_{\text{S}}} \nabla m_x \right), \tag{3.19}$$

$$Q_y = \frac{2}{\mu_0 M_{\text{S}}} \left(\nabla \cdot \frac{A_{ex}}{M_{\text{S}}} \nabla m_y \right), \tag{3.20}$$

$$Q_z = \frac{2}{\mu_0 M_{\text{S}}} \left(\nabla \cdot \frac{A_{ex}}{M_{\text{S}}} \nabla m_z \right).^{1} \tag{3.21}$$

After linearization the Eq. 1.9 in the DE geometry can be written as:

$$\begin{pmatrix} i\frac{\omega}{\gamma\mu_0} m_x \\ i\frac{\omega}{\gamma\mu_0} m_y \end{pmatrix} = \begin{pmatrix} m_y(H_0 + H_{\text{dem}}) - M_{\text{S}}(h_y + Q_y) \\ M_{\text{S}}(h_x + Q_x) - m_x(H_0 + H_{\text{dem}}) \end{pmatrix}. \tag{3.22}$$

[1] Here, different definition of the effective exchange field is used to simplify the calculation. For parameters considered throughout the thesis, there is no discrepancy in results as it was shown in [72].

In order to find the dynamic components of the demagnetizing field (h_x and h_y) the Gauss equation is employed: $\nabla \cdot (\mathbf{H}_{\mathrm{dem}} + \mathbf{M}) = 0$, in which $\mathbf{H}_{\mathrm{dem}}$ can be expressed as the gradient of the scalar potential function, so that $\nabla \times \mathbf{H}_{\mathrm{dem}} = 0$ is always satisfied. In the linear approximation the static component and dynamic components of the demagnetizing field can be regarded as independent. The static demagnetizing field will be calculated separately, the Gauss equation can be split into two equations:

$$\nabla^2 \psi = \frac{\partial m_x}{\partial x} + \frac{\partial m_y}{\partial y}, \quad \nabla^2 \psi_{\mathrm{dem}} = \frac{\partial M_{\mathrm{S}}}{\partial z}, \tag{3.23}$$

where ψ is the magnetostatic potential related to the dynamic components of the demagnetizing field and ψ_{dem} is the magnetostatic potential related to the static component of the demagnetizing field; ψ_{dem} is zero ($H_{\mathrm{dem}} = 0$) in the DE geometry because of the homogeneity of the sample in the z direction (i.e. along the stripes).

In the BV geometry (1.9) can be written in the form:

$$\begin{pmatrix} i\frac{\omega}{\gamma\mu_0} m_y \\ i\frac{\omega}{\gamma\mu_0} m_z \end{pmatrix} = \begin{pmatrix} m_z(H_0 + H_{\mathrm{dem}}) - M_{\mathrm{S}}(h_z + Q_z) \\ M_{\mathrm{S}}(h_y + Q_y) - m_y(H_0 + H_{\mathrm{dem}}) \end{pmatrix}. \tag{3.24}$$

In general, in the BV geometry even if only the y component of the magnetization is nonzero within the sample in the static case, the demagnetizing field will have nonzero components beyond the y direction because of the finite thickness of the sample. The x component of the demagnetizing field will result in a magnetization rotation near the edges of the stripes. However, this effect is neglected here, and consequently, the x component of the static demagnetizing field at the interfaces. Thus, the static demagnetizing field will be collinear with the external field in the calculations. The rotation of the static demagnetizing field (and of the magnetization vector) near the edges of the stripes at low magnetic fields can be critical for analyzing edge modes, which, however, are not the subject of this study. Finally, the magnetostatic potential is calculated from the equations:

$$\nabla^2 \psi_{\mathrm{dem}} = \frac{\partial M_{\mathrm{S}}}{\partial y}, \quad \nabla^2 \psi = \frac{\partial m_y}{\partial x} + \frac{\partial m_z}{\partial z}. \tag{3.25}$$

The term h_z in Eq. 3.24 and the term $\frac{\partial m_z}{\partial z}$ in Eq. 3.25 are zero because of the homogeneity of the sample in the z direction.

The periodic boundary conditions along the y direction are employed, thus the solutions according to Bloch's theorem for the DE geometry are following:

$$\begin{aligned} m_x(x,y) &= m'_x(x,y)\mathrm{e}^{iky}, \\ m_y(x,y) &= m'_y(x,y)\mathrm{e}^{iky}, \\ \psi(x,y) &= \psi'(x,y)\mathrm{e}^{iky} \end{aligned} \tag{3.26}$$

and for the BV geometry:

$$\begin{aligned} m_x(x,y) &= m'_x(x,y)\mathrm{e}^{iky}, \\ m_z(x,y) &= m'_z(x,y)\mathrm{e}^{iky}, \\ \psi(x,y) &= \psi'(x,y)\mathrm{e}^{iky}, \end{aligned} \tag{3.27}$$

where m'_x, m'_y, m'_z and ψ' are periodic functions of y dependent on x and y; k is a Bloch wavevector, which can be limited to the first Brillouin zone, i.e. to the range from -π/a to π/a (a is the period of the lattice). The solutions in the form of Eqs. 3.26 and 3.27 are substituted to the system of governing equations the Eqs. 3.22, 3.23 and the Eqs. 3.24, 3.25 for the DE and BV geometries respectively, to obtain the eigenvalue problem. The eigenvalue problem can be defined so that the eigenvalues are either frequencies or resonance magnetic field values. The eigenvectors represent the spatial distribution of the dynamic components of the magnetization vector.

The eigenvalue problem is written in the weak form [73], obtained by multiplying it by the test function v and integrating over the domain. In the next steps the unstructured grid is generated. The values of parameters are assigned for each grid element. Assuming solution, e.g. in the quadratic form and taking test function in the quadratic form, taking into account boundary conditions leads to creation of a matrix. That is solved by default in COMSOL with Arnoldi iterations method. The Arnoldi iteration method is a way of solving general eigenvalue problem for specified number of eigenvalues around defined eigenvalue.

Procedure of solving eigenvalue problem is executed with the use of COMSOL 4.2. The solutions satisfy electromagnetic boundary conditions on the interfaces between magnetic materials and dielectric (i.e. tangential **h** component and normal **b** components are continuous). On the interfaces between magnetic materials dynamic magnetizations (m'_i) and $\frac{\partial m'_i}{\partial y}\frac{A_{ex}}{M_S}$ are continuous functions [11, 70]. The eigenvalue solution from the solver does not dependanct on the choice of a linearization point of matrix for general linear and quadratic eigenvalue problems. The solution is dependant on the linearization point for nonlinear eigenvalue problem.

Chapter 4

Damping of Standing Spin Waves in MCs[1]

Numerous samples of one-dimensional MCs have been produced to date, many spin-wave spectrum measurements and other experimental investigations performed and supported by theoretical studies. Three basic 1D MC structures are considered: periodic lattices of grooves in a ferromagnetic material,[74, 75, 76, 77] systems of thin ferromagnetic stripes periodically arranged on a dielectric substrate,[78] or bi-component MCs composed of thin stripes of two ferromagnetic materials.[79] More complicated structures have been studied as well,[80] including periodic stripes of different width of the unit cell [81] or ferromagnetic stripes on a metallic or ferromagnetic substrate. Studies of 1D MCs are rich in new physics originating in the complex SW dispersion in plain films, the shape anisotropy and the hysteresis history of the magnetization/remagnetization process. The angular dependence of the spectrum and the propagation losses has been investigated for magnetostatic spin waves in MCs based on yttrium-iron-garnet (YIG).[82] The angular dependence of the SW frequency in an in-plane external field has been examined in MCs formed by permalloy stripes. Hybridization of edge-localized modes has been observed in ferromagnetic resonance spectra.[83]

Many theoretical methods of predicting the properties of MCs have been developed, including micromagnetic simulations,[84] the finite element analysis[11, 85] or the plane wave method,[64] the latter also adapted to thin films of MC with a metallic overlayer.[86] In this study a FEM (section 3.2) is used to calculate the dispersion relation and the FMR absorption spectrum of a thin film of 1D MC in an external magnetic field parallel to the film plane. A two particular configurations of the external magnetic field with respect to the periodicity direction in the MC are distinguished. In one configuration the external field is oriented along the magnetic stripes (the z direction in Fig. 4.1); (Damon-Eshbach DE). In the other configuration, the field is perpendicular to the stripes, i.e. oriented along the x (backward

[1] Based on the [66]

volume BV). The calculations presented in the chapter allows to predict the response of the magnetic metamaterial to electromagnetic waves. Thus, makes it a useful tool for designing devices based on MCs and interacting with electromagnetic waves (more about it in chapter 5).[49, 50, 51, 47, 87, 88] A numerical model is used for analyzing the data obtained from the FMR measurements of samples prepared by magnetron sputtering, photolithography and ion etching by V. K. Sakharov from Kotelnikov Institute of Radio Engineering and Electronics, Saratov branch, Russian Academy of Sciences. Three samples with different structures are studied: a periodic array of Co stripes, a periodic lattice of Py stripes, and a bi-component MC that is the superposition of the other two. These three structures are schematically depicted in Fig. 4.1. The Co stripes are 6.6 μm wide, the Py stripes are 3.4 μm wide, and the lattice constant is 10 μm in all three structures. The samples are 50 nm thick. An important output of this study is a detailed analysis of standing spin waves and the conditions of their formation in the considered structures and geometries, including possible challenges in the observation of standing spin waves in the BV geometry due to attenuation.

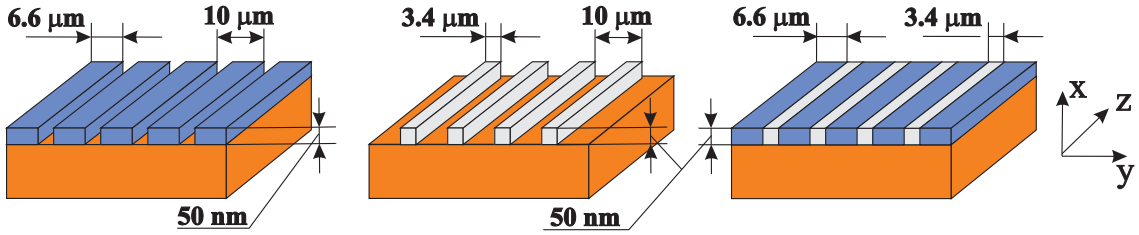

Figure 4.1: Magnonic crystals investigated in this chapter. Left: periodic lattice of 6.6 μm wide Co stripes with a lattice constant of 10 μm. Center: periodic lattice of 3.4 μm wide Py stripes with a lattice constant of 10 μm. Right: bi-component MC of alternate 3.4 μm wide Py stripes and 6.6 μm Co stripes in direct contact. Two geometries are considered: the magnetostatic surface wave geometry with the bias magnetic field oriented along the stripes (z-axis), and the backward volume magnetostatic wave geometry with the field oriented along the direction of periodicity (y-axis). In both geometries the spin waves propagate along the direction of periodicity.

4.1 Experiment

The structures were fabricated by magnetron sputtering, photolithography and ion etching by the Kotelnikov Institute of Radio Engineering and Electronics group. The bi-component MC (Fig. 4.1(c)) was produced by combining the fabrication of a periodic lattice of Co stripes by the etching technique with the fabrication of a periodic lattice of Py stripes by the lift off method using a single photolithography process. In the first step a 50 nm film of Co was deposited on an Si substrate by DC magnetron sputtering. Next, a mask of resist in the form of a striped structure was

created by photolithography on top of the Co film. A positive lithography process was used for AZ5214E resist along with a photomask that had opened for irradiation windows in the form of 3.4 μm wide stripes with a period of 10 μm on an area of 5 mm $\times$ 5 mm. Photolithography was followed by ion etching of the Co film and the deposition of a 50 nm thick Py film through the same photoresist mask by DC sputtering and resist lift off by acetone in ultrasonic bath. Periodic lattices of Co and Py stripes (Fig. 4.1(a) and (b)) were fabricated separately by the etching and lift off techniques, respectively.

The thickness of the Co and Py films was controlled by the deposition time with a constant deposition rate assumed. The deposition rate had been found by growing a few test samples at the same conditions through a shadow mask and measuring their thickness by means of an atomic force microscope (AFM). Similarly, the etching time for Co had been determined by etching test samples and AFM measurements of their thickness.

The geometry of the fabricated structures was checked by the AFM. Figure 4.2 shows an AFM image of the bi-component structure. The geometry of the fabricated bi-component MC was as desired in general, but had two kinds of imperfections. The level of Py was ca. 20 nm lower than that of Co, which could be due to overetching rather than different thickness of the deposited films, since the accuracy of the determined deposition rates was significantly higher than that of the etching rate. The other kind of imperfection consisted in regular defects in the form of vertical flakes on the edges between Co and Py stripes. These defects were probably caused by the deposition of Py on the sidewalls of the photoresist mask.

In order to eliminate the effect of the plain magnetic films beyond the structured regions of the samples, for FMR measurements the 2 mm $\times$ 2 mm squares cut from the middle of each fabricated structure was used. The FMR measurements were performed at a fixed frequency of 9.8 GHz by the conventional cavity method with modulation of the bias field and signal detection using a lock-in amplifier. In this case the FMR signal represents the derivative dP/dH of the absorbed power as a function of the bias field (see, for example, Fig. 4.8 (g)-(i)). To make the comparison between the theoretical and experimental data more clear and to represent the actual absorption curves the experimental FMR signal curves were integrated numerically.

4.2 Formation of Standing Spin Waves

Before presenting the results of the calculations and measurements the expected behavior of the SWs will be discussed in the considered arrays of Co and Py stripes and in the bi-component MC. The predictions will be based on analytical solutions for a plain ferromagnetic thin film in two field configurations: DE and BV spin wave wave geometry. Two models will be of use for the interpretation of the results. One is based on the assumption of almost independent oscillations in the stripes and can be regarded as analogous with the electronic tight binding model. The other model

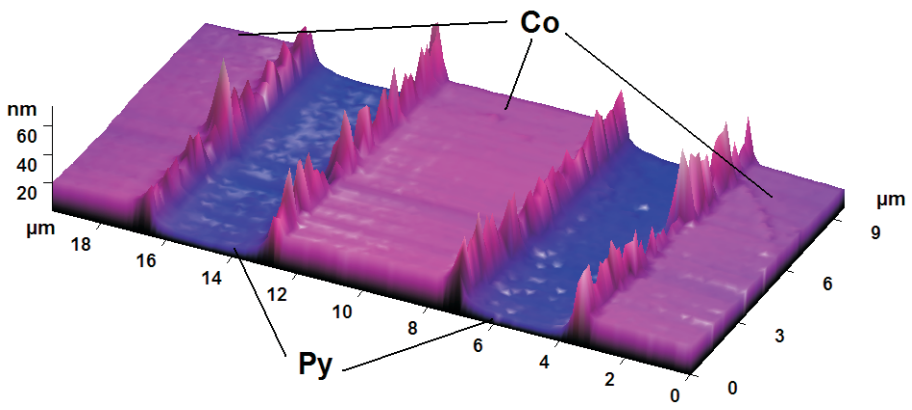

Figure 4.2: AFM image of the fabricated bi-component structure. Measured with the us of Atomic Force Microscope Solver P-47 NT-MDT by Kotelnikov Institute of Radio Engineering and Electronics group.

is based on the Bloch theorem and the magnonic band structure folding to the first Brillouin zone, and is analogous with the nearly free electron model. These models will be used depending on the configuration and the SW spectrum.

Figure 4.3 presents the wavevector dependence of the resonance magnetic field for SWs in plain films of Co and Py (dashed and solid lines, respectively) in the DE and BV geometries (left and right from the point $k = 0$, respectively) for a resonance frequency of 9.8 GHz. In the DE geometry the first excitation (counting from high magnetic fields) in the bi-component MC is expected to be concentrated in Py stripes. At magnetic fields below the FMR field of the plain Py film (0.114 T) and above the FMR field of the plain Co film (0.065 T), i.e. in the range between the two horizontal lines in Fig. 4.3, no states are allowed to SWs in Co. Thus, SWs will be reflected from the boundaries between Py and Co, and standing SW modes are expected to form in the Py stripes, as they would do in an isolated Py stripe. For lower magnetic fields (below 0.065 T) the excitations will spread over both materials instead of being solely confined to Py. The formation of standing spin waves will be possible due to magnonic band structure folding.

Also in the BV geometry field ranges in which waves can propagate solely in Py or in both materials can be distinguished. However, the dispersion relation and the profiles of dynamic magnetization are expected to be more complex in the BV geometry than in the DE geometry, since the dispersion relation for a plain film itself is not monotonic. For certain resonance fields SWs in a bi-component MC composed of Co and Py can have two or three possible values of the wavevector at a fixed frequency. For fields between 0.114 T and 0.15 T two wavevectors are available in a plain Py film and none in a plain film of Co, but for magnetic fields from 0.065 T to 0.08 T there are two allowed states in Co and one in Py (Fig. 4.3). However, it must be remembered that this is only a qualitative estimation since the nonuniform internal magnetic field in the MCs in the BV geometry will affect the dispersion curves observed in measurements.

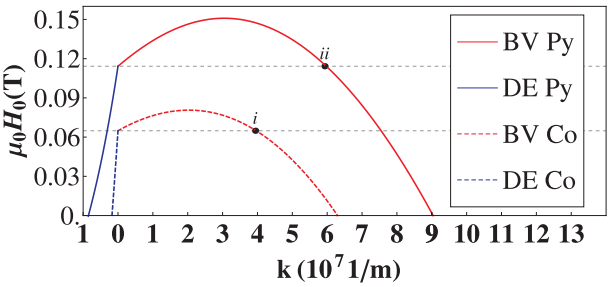

Figure 4.3: Resonance magnetic field versus wavevector in a 50 nm thick uniform film of Py (solid lines) and Co (dashed lines) at a frequency of 9.8 GHz. The blue lines on the left refer to the DE geometry, and the red lines on the right to the BV geometry. Points i and ii correspond to the wavevector values k indicated by vertical grid lines in Fig. 4.13(d)-(f).

The condition of occurrence of standing SWs can also be determined by analyzing the group velocity V_g and the propagation length L in the limit of $k \to 0$ in uniform Co and Py films, which allows to elucidate the effects of damping, too. The propagation length is defined as:

$$L = V_g \tau \approx \frac{V_g}{\gamma \mu_0 \Delta H}, \tag{4.1}$$

where τ is the lifetime of SWs and ΔH is the half-width of the resonance line. The $\Delta H_{Py} = 0.001$ T for Py and $\Delta H_{Co} = 0.005$ T for Co, as observed in experiments.[89] The group velocities V_g^{DE} and V_g^{BV} in the DE and BV geometries, respectively, for $k = 0$ have the analytical form:[90]

$$V_g^{DE} = \frac{\omega_M^2 d}{4\sqrt{\omega_0(\omega_0 + \omega_M)}}, \tag{4.2}$$

$$V_g^{BV} = -\frac{\omega_M \omega_0 d}{4\sqrt{\omega_0(\omega_0 + \omega_M)}}, \tag{4.3}$$

where $\omega_M = \gamma \mu_0 M_S$ and $\omega_0 = \gamma \mu_0 H_0$. Figure 4.4 shows the group velocity V_g and the propagation length L for SWs with $k = 0$ versus the bias magnetic field in plain Co (dashed lines) and Py (solid lines) films, as calculated from Eqs. (4.1)-(4.3). Both V_g and L decrease with increasing bias magnetic field in the DE geometry (Fig. 4.4(a) and (c)) and increase with the bias magnetic field in the BV geometry (Fig. 4.4(b) and (d)). The values of V_g and L are significantly (more than 10 times) lower in the BV geometry than in the DE geometry. This indicates that the observation of SWs in the BV geometry will be more challenging, especially if the width of the Co stripes exceeds the propagation length.

The plots in Fig. 4.4 clearly indicate that even though the group velocity is larger in Co than in Py the propagation length is significantly shorter in Co. This is due to higher spin wave damping in Co. For example, for magnetic fields larger

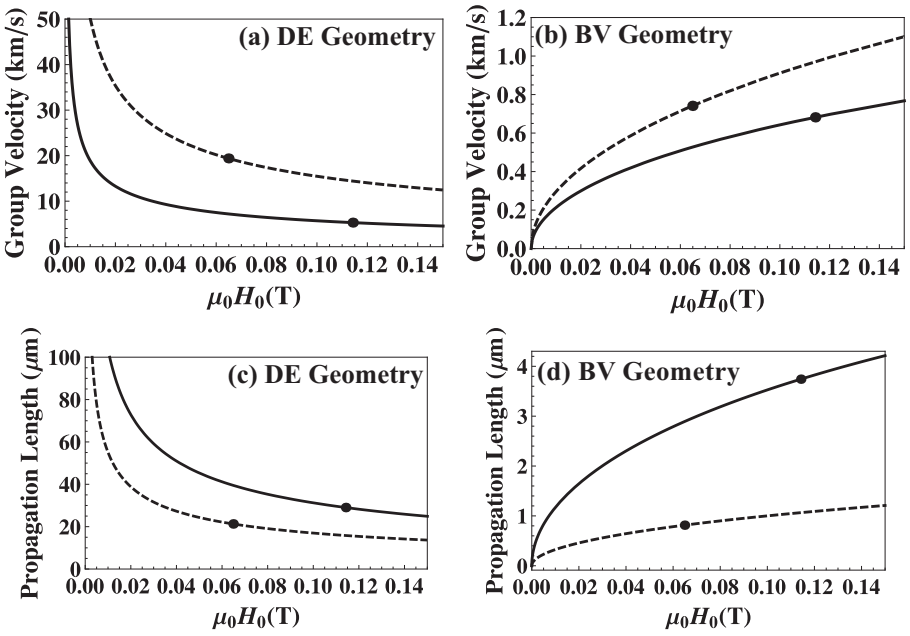

Figure 4.4: (a), (b) Group velocity and (c), (d) propagation length of uniform ($k = 0$) SWs in plain Py (solid lines) and Co (dashed lines) thin films of thickness $d = 50$ nm versus bias magnetic field in two geometries: (a), (c) DE and (b), (d) BV. Highlighted points correspond to uniform film excitations at a frequency of 9.8 GHz.

than 0.06 T the SWs are seen to penetrate Co to a distance shorter than 20 μm in the DE geometry. In the BV geometry in the range of the bias magnetic field considered in this chapter L is up to 1.2 μm in Co (and less than 4.2 μm in Py). This means that coherent coupling of SWs can be suppressed if the width of the Co (Py) stripes is larger than 1 μm (4.2 μm) in the BV geometry. This analysis brings to the conclusion that damping can lead to the suppression of coherent Bragg reflections and, consequently, coherent SW excitations throughout the bi-component MC[70, 91] if the propagation length is shorter than the linear size of the ferromagnetic inclusions. For the same reason damping can suppress the formation of standing SWs in an array of spaced stripes if the stripe width is larger than L. In the samples the Py and Co stripes are 3.4 μm and 6.6 μm wide, respectively. According to the results shown in Fig. 4.4(c) and (d) such a situation can be expected to occur in the array of Co stripes and in the bi-component MC in the BV geometry.

4.3 Numerical Results

The FMR spectra of periodic arrays of air-spaced Py and Co stripes and a bi-component Co/Py MC in the DE and BV geometries (see Fig. 4.1) was calculated and compared with measured data. The analysis and discussion of the results is presented in two subsections devoted to the two geometries considered. Paramet-

ers used in the numerical calculations are following: gyromagnetic ratio $\gamma = 182.2$ GHz/T, Co saturation magnetization $M_{\mathrm{Co}} = 1.35 \times 10^6$ A/m, Py saturation magnetization $M_{\mathrm{Py}} = 0.705 \times 10^6$ A/m, Co exchange constant $A_{\mathrm{Co}} = 2.88 \times 10^{-11}$ J/m and Py exchange constant $A_{\mathrm{Py}} = 1.11 \times 10^{-11}$ J/m. The general qualitative agreement between the numerical results and the experimental data confirms that the pronounced peaks in the FMR spectra occur due to in-plane quantization of standing SWs.

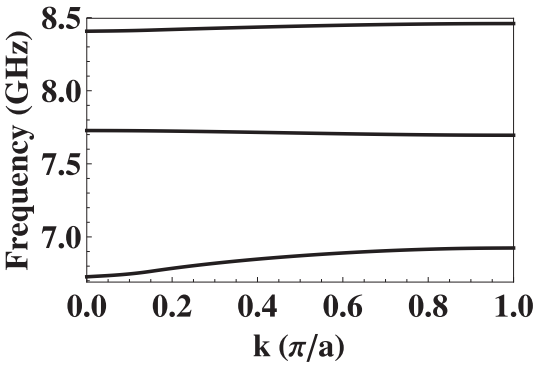

Figure 4.5: Dispersion relation, i.e. plot of frequency versus wavevector in the first Brillouin zone for the bi-component MC composed of alternate 3.4 μm wide Py stripes and 6.6 μm wide Co stripes (with a periodicity $a = 10$ μm) in magnetic field $\mu_0 H_0 = 0.05$ T. The field is oriented along the stripes; the spin waves propagate in the plane of the MC orthogonally to the bias field, i.e. in the DE geometry.

DE spin waves geometry

Figure 4.5 shows the frequency plotted versus wavevector in the first Brillouin zone for the bi-component Co/Py MC in the DE geometry. The group velocity is seen to be low but different from zero for the first few bands, which confirms the collective character of SWs in the bi-component structure. Also, one can see that the multiple SW resonances that occur at $k = 0$ can be regarded as a consequence of the periodicity of the structure. The properties of SWs with a zero wavevector, $k = 0$, strongly coupled to the external alternating field and observed in the FMR experiment will be investigated further. For an in-depth explanation of the magnonic band structure shown in Fig. 4.5 the plot of the amplitude of the SWs is presented. Figure 4.6(a) and (b) presents color maps of the SW amplitude over the (x, y) plane; Fig. 4.6 (c), (d) shows a linear plot of the amplitude along the periodicity direction (y-axis) at the mid-thickness of the MC. The profiles of SWs from the two lowest-frequency bands are calculated for $k = 0$. Quantization of SW modes is seen to occur in the Py stripes. The first mode does not have a nodal line in Py (Fig. 4.6(c)), and the second mode has one nodal line (Fig. 4.6(d)). In both modes the oscillations are suppressed in the Co stripes. These SWs have an almost uniform amplitude across the film thickness.

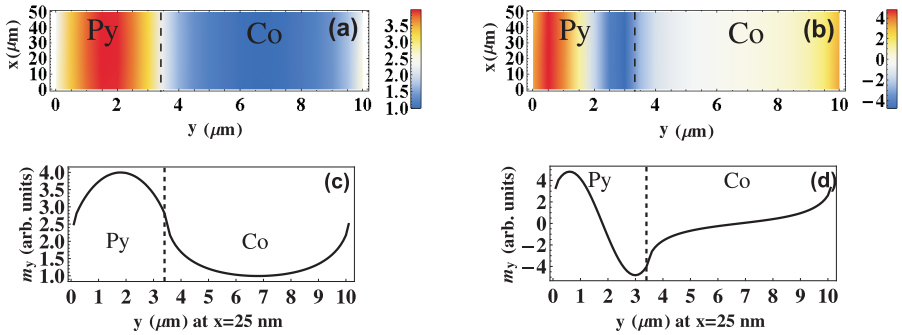

Figure 4.6: Profiles of two lowest-frequency SW modes in the bi-component MC in the DE geometry. (a), (b) Color map of the amplitude of the y component m_y of the dynamic magnetization vector in the plane defined by the thickness and the periodicity direction. (c), (d) The amplitude of m_y in the unit cell along the y-axis at the mid-thickness of the MC. The profiles are as calculated for $\mu_0 H_0 = 0.05$ T and $k = 0$, i.e. in the center of the BZ in Fig. 4.5.

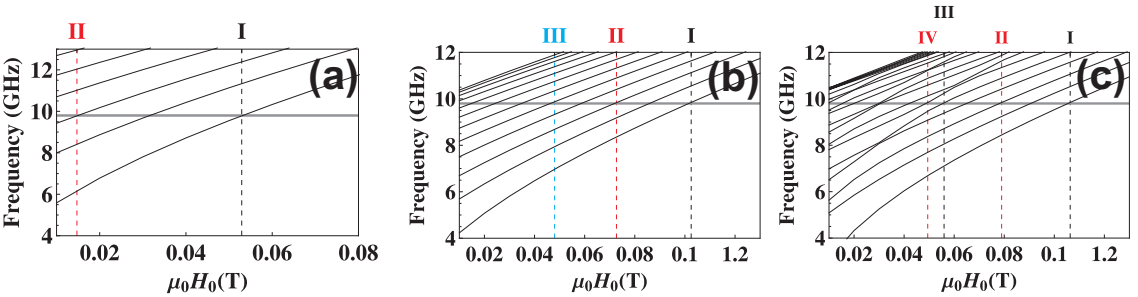

Figure 4.7: Spin wave frequency versus bias magnetic field for: (a) an array of Co stripes (6.6 μm wide), (b) an array of Py stripes (3.4 μm wide), (c) a bi-component Co/Py MCs (with a period of 10 μm) in the DE geometry for $k = 0$. All the three structures have equal thickness $d = 50$ nm and periodicity $a = 10$ μm. The horizontal solid line marks the resonance frequency of 9.8 GHz. The colored vertical grid lines indicate the position of the most intensive modes, the profiles of which are plotted in Fig. 4.8 with the corresponding numbers and colors.

The frequency of a magnonic excitation depends on the bias magnetic field. Figure 4.7 (a), (b) and (c) shows this dependence calculated for $k = 0$ for the three structures considered: an array of Py stripes, an array of Co stripes, and a bi-component Co/Py MC, respectively. The frequencies of all the modes increase with the bias magnetic field. An interesting feature of the bi-component structure (Fig. 4.7(c)) is the crossing and anti-crossing of some lines in the field dependence. This is because some modes have steeper slopes than others. The frequencies of these modes are around 6 GHz (third or forth mode in (c)) and around 8 GHz (seventh mode) at $\mu_0 H_0 = 0$ T, and match with the frequencies of the first two modes in the array of Co stripes (see Fig. 4.7 (a)). Also, as it is seen in Fig. 4.6, the first two modes in the bi-component MC at $\mu_0 H_0 = 0.05$ T are related to excitations

in the Py stripes. This, along with the different slopes, indicate that in the bi-component MC low-frequency modes with the amplitude concentrated in different parts of the MC can be distinguished, i.e. in Py or collectively in Py/Co stripes. Using Eq. (2.2) the intensity of the relative absorption can be calculated, which can be compared with the FMR absorption. In the FMR experiment nonzero-absorption modes are expected to appear at a frequency of 9.8 GHz for different magnetic fields corresponding to the points indicated by the crossing of the vertical grid lines with the horizontal line in Fig. 4.7(a)-(c). The calculated absorption spectra and the experimental data are compared directly in Fig. 4.8(d)-(f).

The Lorentzian function characteristic of each resonance absorption peak is determined by 3 parameters: the resonance magnetic field, the amplitude and the half-width of the peak. These parameters are obtained from the FMR signal in both the DE and BV geometries (solid lines in Fig. 4.8(g)-(i) and Fig. 4.10(g)-(i), respectively) by fitting with derivatives of the Lorentzian functions. The first two parameters can be obtained also from the solutions of the eigenvalue problem defined in (3.22) (or (3.24)). The half-width is directly related to the damping parameter was used for comparison of the numerical data with the experimental results the halfwidth values obtained from the FMR signal. The summation of the Lorentzian functions defined in this way yields a set of absorption spectra (dashed lines in Fig. 4.8(d)-(f) and Fig. 4.10(d)-(f)), which can be compared with the experimental FMR absorption (solid lines in the same Figures). The experimental FMR absorption spectra were calculated numerically by integrating the FMR signal. The calculation results can also be compared directly with the measured FMR signal by using the derivative of the calculated Lorentzian functions, as shown in Fig. 4.8(g)-(i) for the DE geometry and in Fig. 4.10(g)-(i) for the BV geometry; the dashed line represents the theoretical curve.

Spin waves propagating in air-spaced stripes of Co and Py are effectively reflected on the edges of the stripes. The propagation length for the uniform mode in the DE geometry is several times larger than the stripe width (see Fig. 4.4(c)); this enables the formation of standing waves. Since the spacing between the stripes is relatively large, all the measured lines are attributed to standing SW modes in the isolated Co or Py stripe. In Fig. 4.8(d) and (g) the results of the numerical calculations (dashed lines) are compared with the experimental data (solid lines) regarding the FMR absorption and the FMR signal, respectively, in the array of Co stripes. The experimental and numerical results for resonance fields are in good agreement, also in the case of Py stripes (Fig. 4.8(e) and (h)). Figure 4.9(a) and (b) presents the profiles at the mid-thickness of the sample for the most intensive excitations in the array of Co and Py stripes, respectively. However, the relative absorption values are overestimated for some modes, see Fig. 4.8(d) and (e), modes II and III. This overestimation can be attributed to the irregularities in the samples, especially at the edges of the stripes, inevitable in the fabrication process (see Sec. 4.1). These irregularities can suppress the conditions of formation of higher-order standing SWs and the FMR absorption. The damping of SWs can contribute to this effect as well. Spin wave modes with a higher number of nodes along the stripe width have

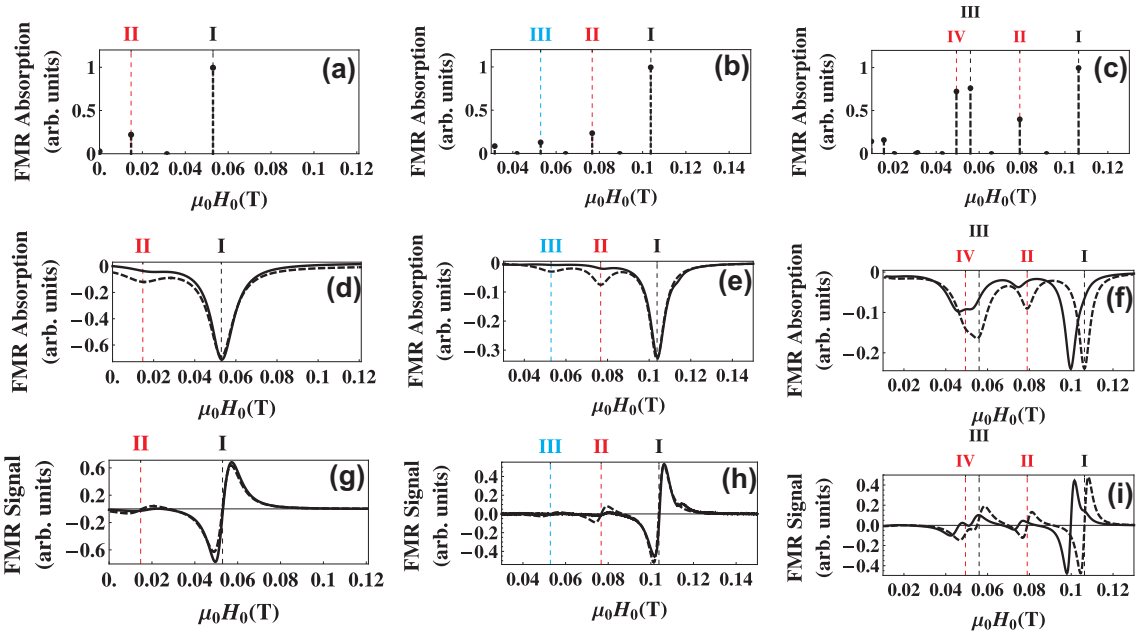

Figure 4.8: Results of numerical calculations and experimental data in the DE geometry for: (a), (d), (g) the array of Co stripes; (b), (e), (h) the array of Py stripes; (c), (f), (i) the bi-component Co/Py MC. (a)-(c) Amplitudes of relative absorption calculated numerically from Eq. (2.2). (d)-(f) FMR absorption spectra obtained by numerical integration of the experimental FMR signal (solid lines) and from calculations (dashed lines). (g)-(i) Experimental FMR signal (solid lines) and numerical curves (dashed lines). Colored vertical lines in (a)-(i) indicate the position of the most intensive modes, the profiles of which are plotted in Fig. 4.9(a)-(d) with the corresponding labels (I - IV) and colors (black, red and blue). Experimental data was measured by V. K. Sakharov from Kotenikov Institute of Radio Engineering and Electronics, Saratov branch, Russian Academy of Sciences.

a nonzero wavevector and a penetration length significantly reduced with respect to the uniform mode in the DE geometry. This is because the group velocity decreases with increasing k.[90] It can be estimated on the basis of an analysis similar to that presented above in Sec. 4.2 for plain thin films, but for wavevectors different from zero. this estimation was performed to find that L for the second standing SW (mode II in Fig. 4.9(b)) will be reduced by $\propto 60\%$ with respect to its value for $k = 0$. This means that the conditions of formation of standing modes will be suppressed to a significant extent and, as a consequence, the FMR absorption will be weaker than in an ideal damping-free medium. Also the effect of band bending will play an important role in the reduction of the group velocity and the propagation length in the MCs. It has been shown theoretically that in a 1D MC the propagation length for magnetostatic spin waves decreases significantly with increasing wavevector and mode number.[92]

In the bi-component Co/Py MC a shift of the calculated resonance fields to higher values with respect to the experimental data (Fig. 4.8(c) and (f)) is observed.

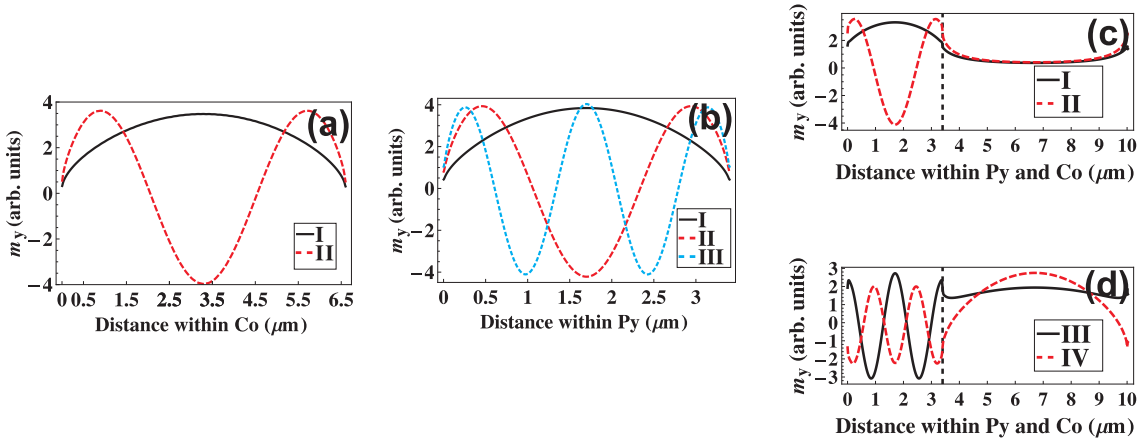

Figure 4.9: Amplitude of the y component of the magnetization vector for the most pronounced absorption peaks in: (a) the array of Co stripes; (b) the array of Py stripes; (c), (d) the bi-component Co/Py MC. The position of the peaks is indicated by colored vertical lines in Fig. 4.8(a)-(i) with corresponding labels (I - IV) and colors (black, red and blue).

The rise is of ca. 6% for all the peaks (lines I to IV). From the possible reasons of this shift one should exclude a small gap between the Co and Py stripes since the conductivity measured along the stripes and along the periodicity direction is almost equal, which means that Co and Py are in direct contact. Neither would a change in the boundary conditions at the interfaces of Co and Py affect the resonance field value significantly. This observation excludes also the effect of the irregularities on the interfaces. However, the interface irregularities can explain the increased absorption intensity of modes II to IV in the calculated spectra with respect to the FMR measurements, as discussed in the case of arrays of Co and Py stripes. The higher frequency obtained from the calculations can be attributed to an increased anisotropy field in the bi-component sample or a slight difference in the saturation magnetization value in Co and Py. The parameter values can vary with sample, since, as discussed above in Sec. 4.1, the samples were fabricated individually.

Figure 4.9(c) and (d) presents a magnetization profiles for the bi-component MC. Two kinds of profiles can be distinguished, depending on the resonance magnetic field: in the profiles of one kind the propagation of the wave is seen to be confined to Py; in the profiles of the other kind the wave can propagate in both materials. This is in agreement with the discussion presented in Sec. 4.2. Spin waves with resonance fields higher than the FMR field of Co will have a significant amplitude of magnetization in Py stripes (see Fig. 4.3). A similar dependence has already been observed in 1D bi-component Co/Py MCs with smaller lattice constants in Brillouin light scattering experiments.[11, 85, 64] These results confirm also the interpretation provided.

BV spin waves geometry

Measurements and calculations have been performed for the considered structures in the BV geometry, too. In this configuration the dispersion relation in a plain magnetic film is not monotonic and the slope of this function (i.e. the group velocity) is much lower than in the case of DE geometry within the range of external magnetic field used in the experiment (see Figs. 4.3 and 4.4). for the sample with lattice constant of 10 μm the border of the first Brillouin zone is at 3.14×10^5 1/m). A consequence of these characteristics of the dispersion relation and Brillouine zone size is high number of solutions of the eigenvalue problem within a given range of magnetic field in confined or periodic structures, such as stripes or 1D MCs. The numerous solutions form a dense band of SW modes. Thus, the plot of the SW frequency vs. the magnetic field for $k = 0$, similar to that discussed above for the DE geometry and shown in Fig. 4.7, presents a challenge because of computational limitations. Therefore the investigation should be confined to the resonance field values at a fixed frequency, namely the frequency of 9.8 GHz used in the FMR measurements. In the BV geometry the group velocity in a plain film is lower than in the DE geometry; consequently, the SW propagation length is much shorter (see Fig. 4.4), comparable with the width of the Co or Py stripe (see Fig. 4.4(d)). This means that the effect of damping on the SW spectrum of the arrays of stripes and the bi-component MC should be more pronounced than in the DE geometry. In the BV geometry the bias magnetic field crosses the edges and interfaces in the arrays of Co or Py stripes and in the bi-component MC, respectively. This results in a strongly inhomogeneous static internal magnetic field and, consequently, more complex SW spectra.

Figure 4.10(a), (d), (g) and Fig. 4.11(a) present the experimental and numerical results for the array of Co stripes; the results obtained for the array of Py stripes are shown in Fig. 4.10(b), (e), (h) and Fig. 4.11(b). The resonance field of the quasi-uniform mode (mode I in the respective panels of Fig. 4.10) in the Co and Py stripes is higher than in the DE geometry. This is a direct consequence of the occurrence of a demagnetizing field that reduces the internal magnetic field in the stripes. The calculated internal magnetic field is plotted in Fig. 4.12(a) and (b) for the array of Co stripes and the array of Py stripes, respectively, and in Fig. 4.12(c) for the bi-component MC. The internal magnetic field is discontinuous at the interfaces, with a step equal to the saturation magnetization difference. Narrow wells are seen to form near the edges of the ferromagnetic stripes in the arrays and at the interfaces within Co in the bi-component MC. These wells enable the formation of modes referred to as edge-localized modes. At the frequency of 9.8 GHz the FMR fields of these modes are relatively high; e.g., the resonance field for edge modes in the bi-component MC is above 0.24 T. Also, the FMR absorption of the edge modes is predicted to be very low, and therefore not observable experimentally. For these reasons the edge modes are excluded from consideration.

Several pronounced peaks are predicted by the numerical calculations for the array of Co stripes and the bi-component MC in the BV geometry, but not observed

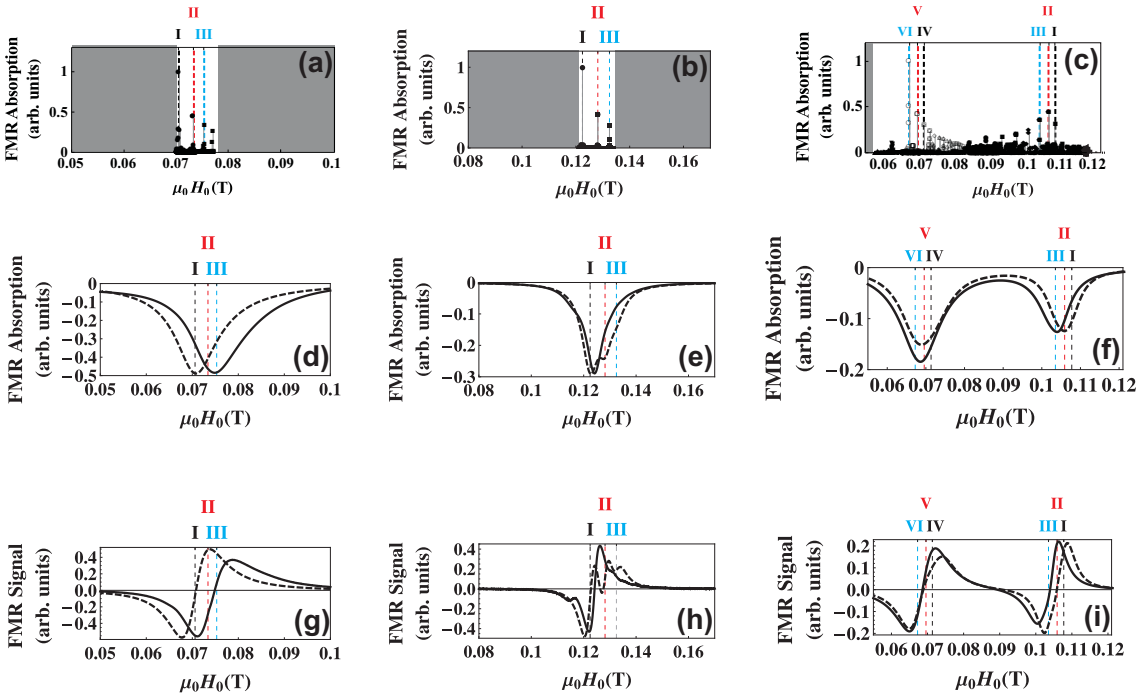

Figure 4.10: Numerical results and measurement data for the considered structures in the BV geometry: (a), (d), (g) the array of Co stripes; (b), (e), (h) the array of Py stripes; (c), (f), (i) the bi-component Co/Py MC. (a)-(c) Amplitudes of relative absorption calculated numerically from Eq. (2.2). (d)-(f) FMR absorption spectra (solid lines) obtained by numerical integration of the experimental FMR signal and the absorption spectra obtained from calculations (dashed lines). (g)-(i) Experimental FMR signal (solid lines) and numerical curves (dashed lines). Colored vertical lines in (a)-(i) indicate the position of the most intensive modes, the profiles of which are plotted in Fig. 4.11(a)-(d) with corresponding labels (I - VI) and colors (black, red and blue). Experimental data was measured by V. K. Sakharov from Kotelnikov Institute of Radio Engineering and Electronics, Saratov branch, Russian Academy of Sciences.

in the measurements, see Fig. 4.10 (a), (c) and (d), (f). However, in the FMR absorption function plotted with the use of the calculated resonance frequencies, absorption intensities and half-width estimated on the basis of the FMR resonance line the resonance peaks with contributions from different SW modes overlap with the main quasi-uniform peak and appear as a single broad absorption peak seen in Fig. 4.10(d) for the array of Co stripes and in Fig. 4.10(f) for the bi-component MC. The difference between the frequency position of the first two numerically calculated SWs in the Co stripes (modes I and II) and in the bi-component MC (modes III and IV) is of 0.0028 T and 0.0023 T, respectively. In the array of Py stripes, narrower than the Co stripes, the split of the peaks (0.0057 T between modes I and II) is large enough to observe a separate excitation (see Fig. 4.10(e) and (h)). Also, ΔH in Co is significantly higher than in Py: $\Delta H_{\mathrm{Py}} = 0.001$ T and $\Delta H_{\mathrm{Co}} = 0.005$ T in plain ferromagnetic films, respectively; as a result the peaks broaden and become

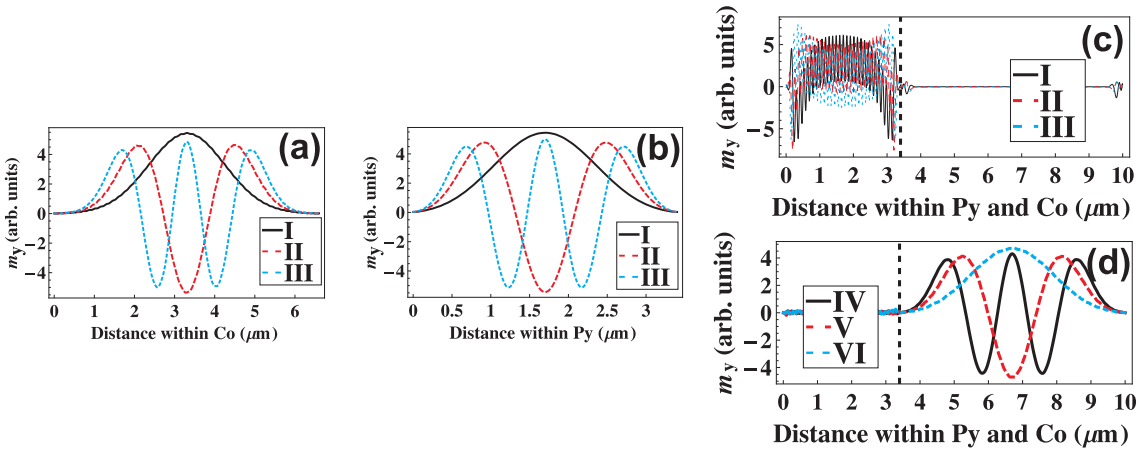

Figure 4.11: Amplitude of the y component of the dynamic magnetization vector for the most pronounced absorption peaks for: (a) the array of Co stripes; (b) the array of Py stripes; (c), (d) the bi-component Co/Py MC. The position of the peaks is indicated in Fig. 4.10(a)-(i) by colored vertical lines with corresponding labels (I - VI) and colors (black, red and blue).

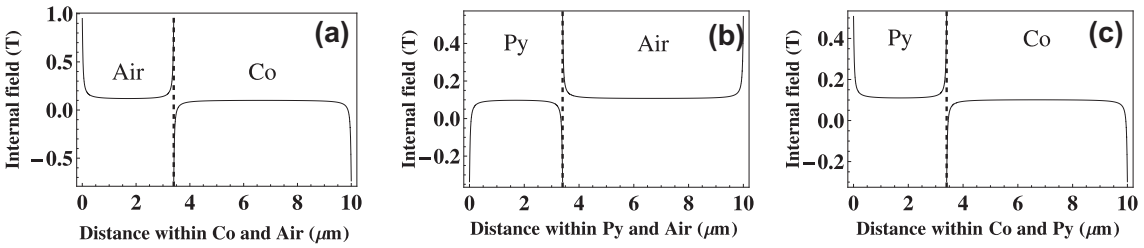

Figure 4.12: Internal magnetic field in (a) an array of 6.6 μm wide Co stripes with a 3.4 μm air spacing; (b) an array of 3.4 μm wide Py stripes with a 6.6 μm air spacing; (c) a bi-component MC composed of alternate 3.4 μm wide Py stripes and 6.6 μm wide Co stripes. All the stripes are 50 nm thick and are fully saturated along the y-axis. Calculations were performed for $\mu_0 H_0 = 0.05$ T.

harder to distinguish in the FMR measurements.

In another possible mechanism the occurrence of a single broad resonance line in the spectrum of the array of Co stripes or the bi-component MC might be due to high attenuation of SWs and a low propagation length in the BV geometry. The width of the Co stripes is 6.6 μm and the propagation length is below 1 μm, as can be estimated from Fig. 4.4(d). This means that the condition of formation of standing modes, including the first standing mode, is not fulfilled. This can also explain the difference in the position of the resonance line in the spectrum of the array of Co stripes obtained from the calculations and from the FMR measurements (see Fig. 4.10(d) and (g)). When the propagation length is much shorter than the wavelength a uniform SW mode, rather than the standing mode shown in Fig. 4.11(a) (mode I), will be excited under a uniform alternating magnetic field. If so, the

resonance field should be close to the FMR field of the plain film. The highlighted point in Fig. 4.3 corresponds to a field of approximately 0.065 T, very close to the value obtained from the FMR measurements, shown in Fig. 4.10(d). The other modes (i.e. II and III) will not be formed at all with such a small propagation length.

In the array of Py stripes the profiles of the most intensive modes (Fig. 4.11(b)) result from the formation of standing SWs in separate stripes. The experimental spectra shown in Fig. 4.10(h) include one intensive line from mode I and lower-intensity signals from modes II and III in higher fields because of the BV geometry and the negative group velocity. In Py the propagation length is above 3.5 μm for magnetic fields of $\propto$ 0.12 T (see the full dot on the dashed line in Fig. 4.4(d)). This means that the condition of formation of the first standing wave is approximately fulfilled; thus, the difference between the resonance field values obtained from measurements and from damping-free calculations should not be large. This is confirmed by Fig. 4.10(e). The formation of standing waves of higher order will be more suppressed due to the reduced group velocity and the consequent reduction of the propagation length.

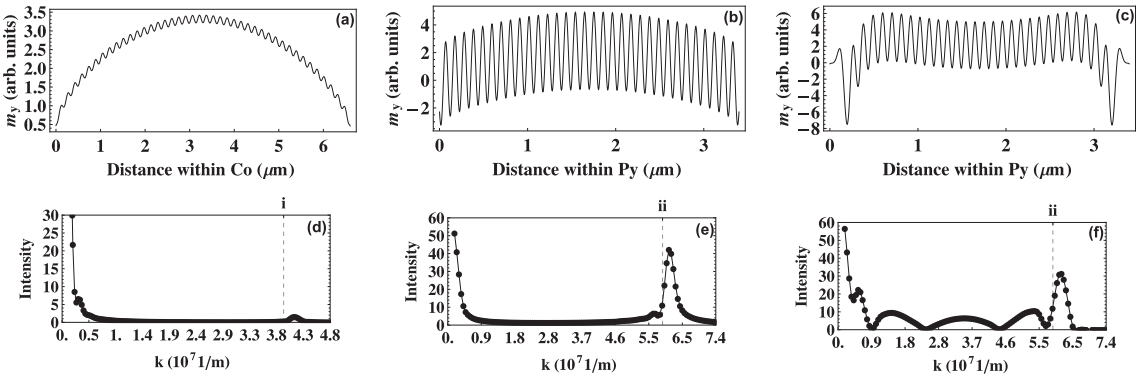

Figure 4.13: Profiles of the y component of the dynamic magnetization in different regions of the bi-component MC: (a) in Co stripes, without the demagnetizing field, (b) in Py stripes, without the demagnetizing field, (c) in Py stripes with the demagnetizing field taken into account. Plots (d)-(f) show the spectra obtained from the Fourier analysis of the respective profiles (a)-(c). Vertical grid lines indicate the value of the wavevector in plain films of Co or Py in the exchange region of the dispersion; see Fig. 4.3, points i and ii for Co and Py, respectively. The corresponding frequency in the plain film is equal to the frequency of the uniform SW.

However, the rapid oscillations in the profiles of the main excitations in the bi-component MC, depicted in Fig. 4.11(c), are rather surprising. The solutions were found to be physical. Their character stems from that of the SW dispersion in the BV geometry. The dispersion of SWs in a plain ferromagnetic thin film is not monotonic and has a minimum for $k \neq 0$. Thus, for certain magnetic field values two solutions are possible, one of which, with a low value of k, forms an envelope for the rapid oscillations of the other, with a higher wavevector value (see Fig. 4.3).The Fourier

analysis is used for verification of this interpretation of the profiles calculated for this MC. The results are shown in Fig. 4.13(d)-(f). The wavelength (wavevector) of the rapid oscillations is found to depend on the exchange constant of the material and correspond very closely to the wavelength of the solution for the uniform material, indicated by the vertical dashed line in Fig. 4.13(d)-(f). This confirms that the obtained profiles are the superposition of two solutions that correspond to the same magnetic field but have different wavevectors.

The Fourier analysis of the profiles has been performed both for the simplified case without the demagnetizing field (Fig. 4.13(a) and (b)) and for the more realistic case with the demagnetizing field fully taken into account (Fig. 4.13(c)). When the demagnetizing field is not taken into account only two Fourier components occur (see Fig. 4.13(d) and (e) for modes in Co and Py, respectively). The incorporation of the demagnetizing field results in the addition of other components (see the profile shown in Fig. 4.13(c)), since the inhomogeneity of the internal field allows for the propagation of waves with different wavevectors at the edges of the sample. Also without the demagnetizing field similar oscillations are seen to occur in Co with the second wavevector dependent of the exchange constant A_{Co}. As a result of incorporating the demagnetizing field the fast oscillations in Co are attenuated and their contribution becomes minor (see the profiles in Fig. 4.11(d)). The demagnetizing field also attenuates the oscillations in isolated Co and Py stripes. The shape of the internal field has a direct effect on the proportional contributions of the two solutions with different wavelength to the dynamic magnetization profiles. When a potential well occurs the contribution of the oscillations with a large k is very small, but increases drastically upon switching off the demagnetizing field or changing its sign in the numerical experiment.

The FMR spectra of fabricated periodic arrays of Co stripes and Py stripes and bi-component 1D MC composed of alternating stripes of Co and Py was studied. The performed numerical calculations have been compared with the results of measurements. The calculations have been done in the frequency domain by the finite element method for two geometries, with an in-plane bias magnetic field oriented along the stripes (DE spin waves geometry) or along the periodicity direction (BV spin waves geometry). The calculated resonance frequencies and relative intensities of the FMR absorption peaks are in a good agreement with the measured data. In both field configurations the group velocity and the propagation length to formulate the conditions of standing spin waves formation in magnonic crystal was analyzed.

Numerical calculations of the spatial distribution of the dynamic components of the magnetization vector confirm that the excitations in the FMR spectra are due to spin wave quantization. This strong absorption peaks suggest existing of a strong interaction of light and standing spin waves. The decrease of the absorption peaks due to the damping is not critical, thus the metamaterial based on the effect of lateral quantization will be described in the next chapter. In the BV geometry rapid oscillations modulated by a long-wavelength envelope oscillations have been observed. A Fourier analysis of these rapidly oscillating dynamic magnetization components has shown that their occurrence is related to the non-monotonic character of the

dispersion relation in the BV geometry. The experimental and theoretical results confirms that the presented method of calculation can be of use for the investigation of the properties of MCs.

Chapter 5

Negative Refractive Index Metamaterial[1]

In recent years negative refractive index metamaterials have attracted wide attention of researchers.[93] Materials possessing simultaneously negative electric permittivity and negative magnetic permeability [94, 95, 96] and therefore also the negative refractive index (NRI)[50] are desirable due to their unusual electromagnetic properties[51, 97] that open ways for creating new potential applications, such as perfect lensing, electromagnetic cloaking, modulators for terahertz radiation or compact waveguides.[98, 51, 99, 100, 101] Various methods of realization of metatmaterials have been proposed, e.g., based on arrays of split ring resonators[102] or ferromagnetic resonance (FMR) in a magnetic material, where the coupling of light is sufficiently strong to obtain negative permeability in the vicinity of the resonance. [103, 48]

The negative refraction of electromagnetic waves due to ferromagnetic resonance has been studied in recent years. It was shown that for the metallic system with large imaginary part of the dielectric permittivity the negative permeability is a sufficient condition to obtain a negative refraction. For example, the negative refraction was observed in $L_{2/3}$ $Ca_{1/3}MnO_3$ films at 150 GHz and 90 GHz frequencies, under very strong external magnetic field of over 5 T and 3 T, respectively.[104] In ferromagnetic dielectrics, like an yttrium iron garnet, YIG slabs implanted with metallic wires have been investigated as a NRI (left handed) metamaterial operating in the microwave band.[99] The experimental data were successfully compared with finite element simulations for systems operating in microwave bands from 8 to 18 GHz.[105] Also the periodic structure of interacting nanowires was proposed in Ref. [106] as a metamaterial. The calculations were performed on the basis of an effective permeability tensor for uniform spin-wave excitations, i.e., for FMR conditions.

The FMR in ferromagnetic materials appears usually at GHz frequencies,[103] thereby restricting the possible applications of metamaterials based on this effect to

[1] Based on the [49]

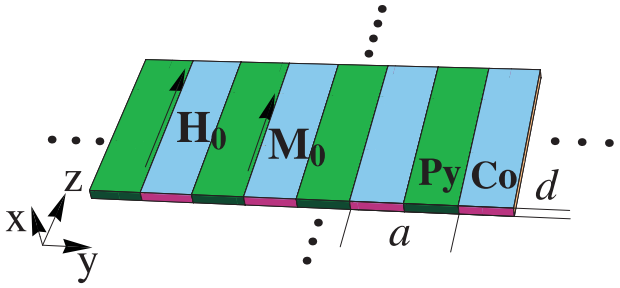

Figure 5.1: Magnonic crystals: one-dimensional MC of thickness d formed by long stripes of ferromagnetic metals Co and permalloy, arranged with the period a. Bias magnetic field H_0 saturates both materials along z axis.

microwaves. Spin wave resonance (SWR) can extend this limit to frequencies of up to hundreds of GHz and composites with SWR in THz frequencies are already considered for applications in THz communication. Maxwell equations simultaneously with the Landau-Lifshitz equation for the magnetization have been solved to obtain the transmission coefficients for the array of nanowires.[107] Extrema in the transmission function have been found due to spin-wave resonance and antiresonance modes.

A novel design of negative refractive index metamaterial working at sub-THz frequencies was proposed in the recent paper by Mykhaylovskiy et al. [48]. The system composed of thin ferromagnetic layers separated by nonmagnetic dielectric material was considered. The significant increase of the resonant frequencies was predicted due to the pinning of the spins on the surfaces of ferromagnetic layers. Here, a different structure to obtain a similar effect is proposed. Replacing the uniform ferromagnetic layer by a thin plate of a MC (see Fig. 5.1) will introduce the in-plane quantization of spin-waves. As a consequence, multiple resonances will be observed in the SWR spectrum in addition to the fundamental uniform excitation. A electromagnetic wave traveling along the x-axis (with such polarization that an alternating magnetic field component $\mathbf{b}$ is along y-axis) can be coupled with the h_y component of the standing spin wave. This effect can be used to obtain negative permeability, if the coupling of light to the higher order SWR excitation is strong enough. The method of calculating the scalar permeability function of the extraordinary wave is presented in the case of in plane magnetization for metamaterials consisting of one-dimensional magnonic crystals (Fig. 5.1). The calculations are based on the plane wave method (PWM) and analytical formulas for permeability of an effectively uniform magnetic film.[48]

Since the NRI is obtained by SW resonance, the electromagnetic properties of structures proposed in this chapter will be dependent upon the external magnetic field. The frequency range in which the negative refraction is observed might be tuned by the external magnetic field in a broad frequency range. Structures under consideration will offer some advantages over other NRI meta-materials, and the simplicity, diversity, and versatility of their design might be some of them. A

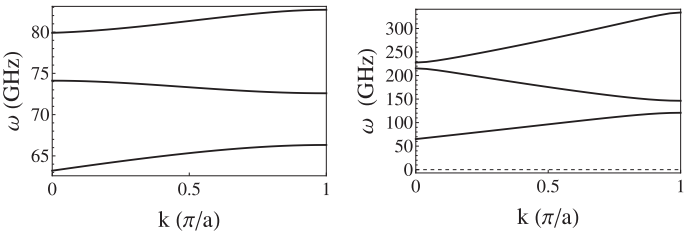

Figure 5.2: The dispersion relations of SWs propagating in a 1D MC composed of Co and Py stripes under bias magnetic field $\mu_0 H_0 = 0.01$ T are shown for lattice constant of (a) 500 nm and (b) 50 nm.

unique functional property of MCs is their re-programmability, i.e., a possibility to obtain the MC in ferromagnetic or antiferromagnetic configuration by manipulation of the bias magnetic field. Then the response of the device will be different in each configuration.[108, 109] The intrinsic loss is a factor that migh limit the applications of metamaterials[110, 111]. However the metamaterial proposed here might also find an application for developing a zero refractive index materials.[52, 112] At frequencies larger than the resonance frequency, the magnetic permeability goes from negative to positive values through zero, the latter point called antiresonance condition.[107] Because zero of permeability property appear the antiresonance condition occurs at frequencies shifted further away from resonant frequencies as compared to NRI, the associated absorption decreases.

5.1 Stationary Solutions in 1D Magnonic Crystals

All calculations were performed for MC composed of two materials, i.e., cobalt and permalloy. The parameters of permalloy are taken following: magnetization of saturation $M_S = 0.86{\cdot}10^6$ A/m and exchange constant $A = 1.1{\cdot}10^{-11}$ J/m; for cobalt: $M_S = 1.3 \cdot 10^6$ A/m and $A = 2.8 \cdot 10^{-11}$ J/m. This choice of constituent magnetic materials is not accidental. Recently, there appeared in literature a few papers on theoretical and experimental investigation of spin-waves in thin film MCs composed of Co and Py stripes with lattice constant 500 nm.[11, 85, 64] The parameters chosen here are taken from the Ref. [11] where anisotropy field was neglected, as it is here. This shows also that realization of such MC is feasible.

The investigation is limited to the Damon-Eshbach configuration, i.e., when the wave vector and H_0 are perpendicular to each other.[29] The SW's propagation along the y axis with bias magnetic field pointing in the z direction is considered, see Fig. 5.1. An important property of SWs is that their dispersion relation is not scalable with the lattice constant, since the relative strength of the exchange and dipolar interactions depends on the lattice constant value and on the wave vector. For small lattice constants, the onset of the domination of the exchange interaction is expected in the first BZ already, while for large lattice constants the magnetostatic interaction can dominate in the whole 1st BZ. The exchange interaction is also

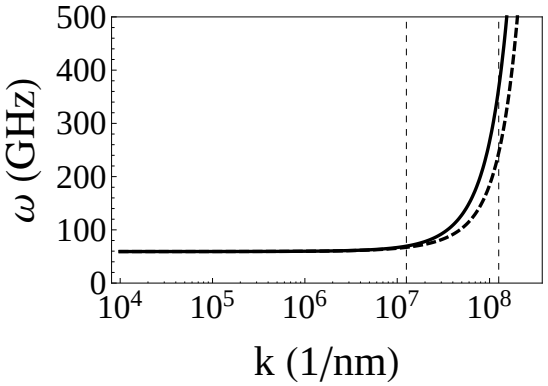

Figure 5.3: The dispersion relation of SW propagating in a thin uniform magnetic film under bias field $\mu H_0 = 0.1$ T for Co—dashed line and Py—continuous line. The grid lines indicate the values of the wavevector (in logarithmic scale) at the 2nd Brillouin zone edge of an lattice constant of 500 nm ($k = 1.26 \cdot 10^7$ 1/m)and 50 nm ($k = 1.26 \cdot 10^8$ 1/m). Values of frequencies at this points are in the range of frequencies of the 2nd order mode, appearing due to the periodicity, in MC. This explains the increase of the SW modes frequencies with decrease of the lattice constant of the magnonic crystal observed in Fig. 5.2 and Fig. 5.4.

responsible for increasing frequency of SW with decreasing the lattice constant. The dispersion relations of SWs calculated with PWM for 1D MCs of 5 nm thickness and lattice constants of 500 and 50 nm are shown in Fig. 5.2(a) and (b), respectively. It is clear that for small a the Brillouin zone is wider and consequently the frequencies of SWs reach higher values.

In Fig. 5.3, the dispersions of SWs in uniform films of Co (dashed line) and Py (continuous line) are presented as calculated according to analytical formula from Ref. [5]. On the same graph, the vertical dashed lines indicate the BZ edges occurred for the MC with the periodicity of $a = 50$ and 500 nm. One can see that, for small a, e.g., 50 nm, the dispersion has parabolic shape for wavevectors at the edge of BZ, while for large a, e.g., 500 nm, it is almost linear. The SW resonances at high frequencies in the center of BZ appear due to introducing the periodicity, as it was described in the chapter 4. Band folding for SWs with dominating exchange interactions will appear at large wavevectors. It means that for high frequency applications the MCs with small lattice constant are more convenient, see in Fig. 5.4. The frequency of SWs in 1D MC with the wavevector equal to 0 are plotted as a function of the lattice constant. The frequency of the first band is only weakly dependent on a while frequencies of higher bands significantly increase with frequency, e.g., 2nd band for 50 nm lattice constant has frequency already close to 40 GHz.

The relative amplitude of SWR calculated for Co/Py MC is shown in the Fig. 5.5(a). The intensity was calculated with the use of 2.2. The relatively high intensity of the 3rd resonant mode is visible. The reason of its high intensity could be

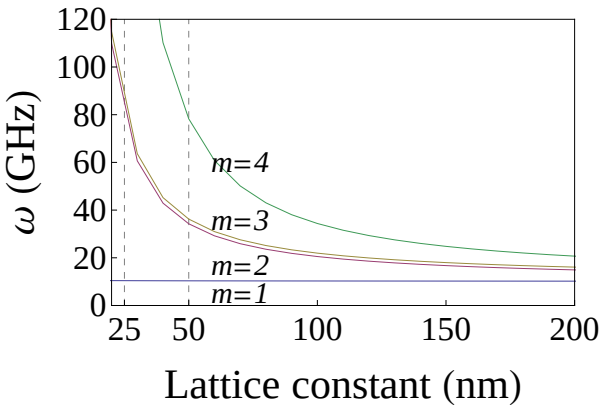

Figure 5.4: Dependence of the frequency of SWs on the lattice constant of 1D MC. The frequencies of spin waves at the center of the 1st BZ are shown. m indicates the mode number. The structure is composed of alternating cobalt and permalloy stripes of 5 nm thickness with the width varied from 10 to 100 nm, i.e., lattice constant vary from 20 to 200 nm. The frequencies of modes above the first one increase as the lattice constant decreases. This effect is crucial and indicates the importance of using the MC with small lattice constants.

understood by looking at the profiles of SWs shown in Fig. 5.5(b). The distribution of the dynamical component of the magnetization is not symmetric among Co and Py. The highest amplitude of the m_y component is localized within the permalloy stripes for the first mode, whereas within the cobalt stripes for the 3th mode. In the case of the 2nd and 4th mode, the distribution has an antysymmetrical character, so they do not couple with the electromagnetic wave.

5.2 Effective Parameters and Permeability of 1D MC

In the long wavelength limit when the length of the material modulation is much shorter than the wavelength of SWs, the magnonic crystal appears to have properties of a uniform material. In this limit, such effective parameters as the magnetization saturation, exchange coefficient and magnetic field can be assigned to the magnonic metamaterial and describe SWs in it. The proper assignment of the effective parameters is not a simple task because it depends on the scale and the structure of the MC. In the 2D case of MC formed by antidot lattice, it was shown that long SWs behave either as in effective waveguides or as in uniform thin film.[113, 114] This depends on the symmetry of the antidot lattice and on the filling fraction, i.e., the relative space occupied by antidots in a magnetic material. In MC formed by ferromagnetic materials only, the SW should behave as in a uniform thin film with effective values of the magnetization saturation and effective exchange constant in the long-wave limit.

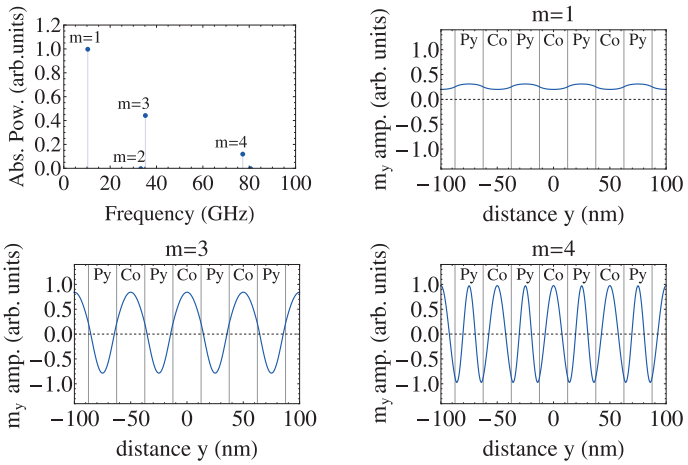

Figure 5.5: The analysis of the resonant modes of 1D magnonic crystal composed of alternating cobalt and permalloy stripes of 25 nm width each and 5 nm thickness. The graphs show: a) The relative absorption intensities. b)-d) The distribution of the y component of dynamic magnetization for modes with $m = 1$, 3, and 4.

The effective parameters could be extracted from a dispersion relation so that when they are applied in the analytical formula for dispersion relation, the function is reconstructed. [115, 116, 117] The value of the effective saturation magnetization can be also obtained by fitting the spin wave frequency to the following analytical formula as a function of the bias magnetic field, H_0, in the homogeneous thin film, i.e., the Kittel formula:[90]

$$\omega(H_0) = \gamma\mu_0\sqrt{(H_0(H_0 + M_{\text{eff}}))} \tag{5.1}$$

with numerical results of the PWM obtained by solving Eq. (3.11). In Eq. (5.1), M_{eff} is the effective saturation magnetization. In Fig. 5.6, the continuous line represents function $\omega(H_0)$ obtained from numerical solution of Eq. (3.11). By fitting M_{eff} in Eq. (5.1), the effective magnetization $M_{\text{eff}} = 1.0 \cdot 10^6$ A/m is found. This value is very close to the weighted average of magnetization in Co and Py, $M_{\text{av}} = 1.08 \cdot 10^6$ A/m. The dependence of the first resonance frequency upon the bias magnetic field given by Eq. (5.1) with the fitted value of the effective magnetization is superimposed on the PWM results and marked by dots. The relative error is small and does not exceed 1.5% in the range of bias magnetic fields from 0 to 0.2 T.

Using the results from PWM, a metamaterial with negative permeability is proposed. The idea is based on the model developed by Mikhaylovskiy et al. [48] where a stack of thin ferromagnetic films separated by nonmagnetic dielectric layers was proposed as a metamaterial. The effective negative permeability was obtained in the proximity of the SWR frequencies in a sub-THz range. The relatively high frequencies resulted from standing waves formed across the thickness of the thin ferromagnetic films. Here, another way of shifting SWR to higher frequencies by introducing thin MC slabs instead of the uniform thin films is proposed. A schem-

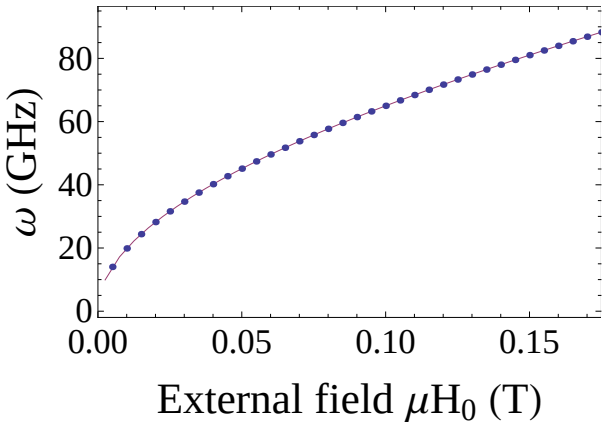

Figure 5.6: The first resonant frequency of the 1D MC composed of alternating cobalt and permalloy stripes of 25 nm width each (5 nm thicknesses) is plotted as a function of the external magnetic field using the analytical formula, where the effective magnetization is a parameter (continuous line), and from the results of PWM for Co/Py magnonic crystal (dots).

atic drawing of the proposed structure is shown in Fig. 5.7(a). The SWR resonance at high frequencies is achieved now due to the lateral (in-plane) quantization of spin-waves, while uniform excitations are assumed across the thickness. Below, the idea is described in detail together with estimations of the permeability of such a structure. According to the PWM results the values of the higher resonant frequencies are expected to increase with the decrease of the lattice constant, Fig. 5.4. This dependence gives an opportunity to design the structure of MC according to a required frequency range of negative permeability.

Having M_{eff} at hand the permeability as a function of frequency can be ploted by using the analytical solution derived in Ref. [48] for the material that is characterized by this effective magnetization. This analytical solution for the $\mu(\omega)$ in vicinity of the frequency of the 1^{st} resonance can be fitted with the resonance formula:[118]

$$\mu(\omega) = 1 + \frac{A_1}{\omega_1 - \omega + i\omega\alpha}, \tag{5.2}$$

where: A_1 is a fitting parameter and ω_1 is the first SWR frequency. In order to find the absolute value of an absorbed power at higher resonant frequencies their relative intensities (found in PWM) can be normalized to A_1, so the relative intensities of the first 3 modes for MC of 50 nm lattice constant are now:

$$A_1 = 0.0058,\ A_2 = 1.16 \cdot 10^{-13} \cdot A_1 \approx 0,\ A_3 = 0.45 \cdot A_1. \tag{5.3}$$

The permeability function can be obtained now by using frequencies and intensities from the normalized absorption of peaks calculated with the PWM and the fitting

formula for the resonances:

$$\mu(\omega) = 1 + \sum_{j=1}^{N} \frac{A_j}{\omega_j - \omega + i\omega\alpha}, \tag{5.4}$$

where A_j are the parameters that describe the intensities of the permeability function already found in Eq. (5.3) and ω_j are the resonant frequencies of the 1D MC (known from PWM calculations). N is the number of modes, which is restricted to 3. The resulting real part of function $\mu(\omega)$ is shown in Fig. 5.7 (b) by a solid line. The value of the damping factor, α, is taken as $\alpha = 0.01$. The same composition of the metamaterial is taken as in Ref. [48] but instead of the uniform ferromagnetic films the 1D MCs is included. The MC occupies 25% of the volume, while the rest is nonmagnetic dielectric (see Fig. 5.7 (a)).

This solution is obtained for the geometry where external magnetic field is applied in plane of the magnetic film. The propagating wave is linearly polarized, perpendicular to the magnetic field (see the Fig. 5.7 (a) for the orientation of the AC magnetic field and wave propagating direction). The wavelength of the electromagnetic wave is much longer than the thickness of the film, and so, the electromagnetic field is assumed to be uniform in single film made of 1D MC. In the MC, due to the periodicity in the structure the band folding effect is observed, and many resonances might be observed at higher frequencies for $k = 0$.

The Fig. 5.7 (b) shows that the relative absorption intensity of the higher modes of the thin slab of magnonic crystal can be comparable with that of the first mode and thus lead to a significant absorption due to the spin wave resonances. As a result the proposed metamaterial can have a negative permeability at elevated frequencies as shown in Fig. 5.7 (b).

The frequency of SWR can be increased and the frequency of NRI band more by applying higher external magnetic field or by decreasing a lattice constant. In Fig. 5.4 was shown the increase of SWR frequencies (for $m > 1$) with decreasing lattice constant. In Fig. 5.7 (b) by dashed line the permeability is shown in function of frequency for MC composed of Co and Py stripes of 12.5 nm width. The band of negative permeability connected with 2^{nd} mode still exists at frequencies above 80 GHz.

Finally, it is instructive to estimate the figure of merit of the proposed metamaterial defined as:

$$\text{FOM} = -\frac{\text{Re}(n)}{\text{Im}(n)}, \tag{5.5}$$

where n is defined according to Ref. [119], fulfilling the causality principle. Firstly, one should find the effective permittivity of the single magnonic crystal ${\varepsilon_{\text{eff}}}^{\text{MC}}$. In the case of normal incidence of light the permittivity can be approximated by:[120]

$$\frac{1}{{\varepsilon_{\text{eff}}}^{\text{MC}}} = \frac{f_{\text{Co}}}{\varepsilon_{\text{Co}}} + \frac{f_{\text{P}}}{\varepsilon_{\text{P}}}, \tag{5.6}$$

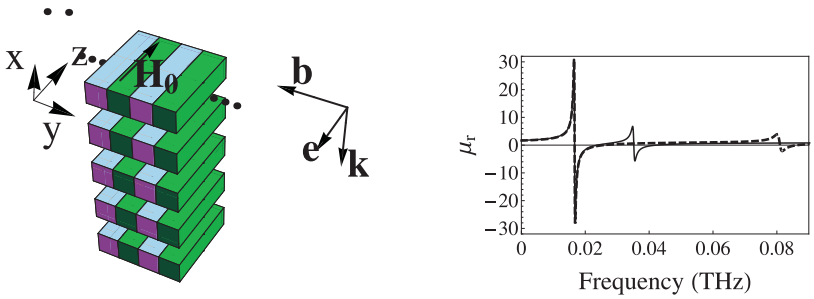

Figure 5.7: (a) The structure of the metamaterial under investigation. The **e**, **b** indicates the polarizations of external electric and magnetic fields, **k** indicates the direction of propagation. (b) The real part of permeability calculated according to Eq. 5.4 (μ_r) as a function of a frequency for the stack of a thin layers made of slabs of 1D MC, composed of alternating 5 nm thick cobalt and permalloy stripes of 25 nm width (solid line) and 12.5 nm width (dashed line) under influence of the external magnetic field of $H_0 = 0.2$ T. The filling fraction of the magnonic crystal in the nonmagnetic dielectric matrix is 25%, it the same as in Ref. [48].

where f_{Co}, $\varepsilon_{\mathrm{Co}}$, f_{P} and ε_{P} are the relative volume fraction and permittivity of cobalt and permalloy, respectively. Structures considered here have $f_{\mathrm{Co}} = f_{\mathrm{Co}} = 0.5$. Then the effective permittivity of the whole structure is:

$$\varepsilon_{\mathrm{eff}} = (1-\rho)\varepsilon_{\mathrm{h}} + \rho\varepsilon_{\mathrm{eff}}{}^{\mathrm{MC}}, \tag{5.7}$$

where ε_{h} is the permittivity of the host nonmagnetic dielectric and ρ denotes the filling factor of the magnonic plates in the metamaterial, $\rho = 0.25$. The $\varepsilon_{\mathrm{Co}} \approx \varepsilon_{\mathrm{Py}} \approx (-1-i)\cdot 10^4 \gg \varepsilon_{\mathrm{h}} isassumed.$[121] Thus leading to the simple estimate for the effective permittivity as $\varepsilon_{\mathrm{eff}} = \rho\varepsilon_{\mathrm{Co(Py)}}$. The FOM for metamaterial composed of 1D MCs with Co and Py stripes of 25 nm width is shown in Fig. 5.8 (a), the real part of refractive index is shown in Fig. 5.8 (b). One can see that FOM in the frequencies around negative refractive index (i.e., around 15 and 37 GHz) reaches the value of 2.

The values of FOM found at resonant frequencies in this work are comparable with values found for fishnet structures proposed in Ref. [122] and lower than those found in Ref. [123], where the coupling relationship between the electric and magnetic resonances was studied in double bowknot shaped structures in order to optimize losses. The authors of Ref. [124] propose a structure that does not contain any metallic materials but a cubic periodic array of layered dielectric spheres, made from low-loss high-permittivity ceramics. Since the absorption is much lower in dielectrics, they achieve a low loss NRI material. In MC based metamaterials considered here there are few ways for improving the FOM. Instead of the ferromagnetic metals a dielectric ferromagnet (e.g., yttrium iron garnet) can be considered as a basis for the proposed structures. Another way for decreasing loss is to remove one of the magnetic metallic materials or to use two-dimensional antidot lattices (ADL)

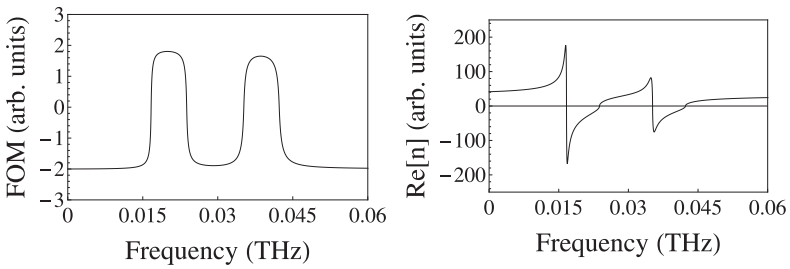

Figure 5.8: (a)The Figure of merit (FOM) in function of a frequency of the considered metamaterial (the stack of a thin layers made of slabs of 1D MC, composed of alternating 5 nm thick cobalt and permalloy stripes of 25 nm width) with negative refractive index. (b) The real part of the refractive index.

as the 1D MCs. In both cases one can expect the effect of periodicity and in-plane quantization to remain.[125, 109, 113, 126] The ADLs formed by a regular lattice of holes in thin film of ferromagnetic material are intensively studied recently and formation of a magnonic band structure was experimentally proved.[10, 127, 128]

As a result, considering that the interaction of EM with laterally quantized SWs is strong, it was possible that the negative permeability at frequencies close to 100 GHz can be achieved in the periodic metallic magnetic structures, i.e., thin plates of 1D magnonic crystals, being a result of the lateral quantization of SWs. The frequencies of the resonant modes of MC were investigated as well their relative absorption intensities in dependence on the lattice constant. The analysis of the mode profiles is conducted in order to demonstrate the strong coupling of high order magnonic modes to electromagnetic wave. It was shown that for the structure composed of the stack of thin films of 1D MCs of lattice constant 50 nm and 25 nm (i.e., alternating cobalt and permalloy stripes of the thickness of 5 nm and width of 25 nm or 12.5 nm) separated with nonmagnetic dielectric, the negative permeability can be achieved at relatively high frequencies. A further decreasing of the lattice constant or introducing periodicity in the second dimension should shift SWR and so bands of a negative permeability above 100 GHz. Another possibilities for increasing the resonant frequencies of SW modes are: increasing of the field or using the antidot systems. There is also a possibility for an applying the pinning boundary conditions on the top or bottom surfaces of the thin plate of MC. In this case the combined effects of the lateral and thickness quantization of SW modes should result in increasing frequencies of SWR above 100 GHz.

Chapter 6

Nonreciprocity in Structures with Metallic Overlayer[1]

In this chapter, the calculations of the dispersion of uniform film and MCs with conductive overlayer are presented. Nonreciprocal properties of the waves of different nature can have various origin and can be manifested as the dependence of a dispersion relation on the wave propagation direction, i.e., $\omega(k) \neq \omega(-k)$, where ω is the angular frequency and k is a wavenumber. The nonreciprocal properties of electromagnetic waves are often related with the magneto-optical interaction which reflects the time reversal broken symmetry in magnetic systems [131, 132, 133, 134], a necessary condition of nonreciprocity (apart from broken space inversion symmetry). The discovery of nonreciprocity in photonic crystals (PCs) has opened new paths for design of integrated photonic devices (like isolators and circulators) having big potentials for the integration with semiconductor technology [135, 136, 137]. Thus PCs with nonreciprocal properties are intensively studied and the accompanying effects of electromagnetic unidirectionality like frozen modes and slow light phenomena have already been explored [138]. Nonreciprocal property has also been exploited in PCs with a topological one-way edge states [139, 140]. In these structures electromagnetic wave is transmitted in one direction and is very resistant to scattering on defects and roughness due to prohibited propagation in the opposite direction. More complicated photonic structures with indirect interband photonic transitions [141], plasmonic systems [142] and metamaterials [143] were also investigated.

The spin wave in magnetostatic limit propagating in the in-plane direction of the film, perpendicular to the in-plane external magnetic field posses nonreciprocal property, although its dispersion relation is reciprocal [29]. The amplitude of dynamic component of the magnetization vector of this SW is localized near one of the surface of the film, depending upon the direction of propagation. Change of the direction of propagation (or alternatively the change of the direction of the external magnetic field) will cause the localization of SW moves to the opposite surface of the

[1]Based on the [129, 8, 130]

film. Any kind of asymmetry of the film or its surrounding should cause emerging of nonreciprocal dispersion relation. In that sense it is an analogy with the photonic case, where spectral nonreciprocity appears when are broken both, time and space inversion symmetries [144].

The SWs propagating in a ferromagnetic film covered on one side by a perfect electric conductor (PEC) (i.e., a metal with infinite conductivity) in direction perpendicular to the in-plane bias magnetic field will also posses a nonreciprocal dispersion [30]. Metallization strongly affects SW propagating in the direction that have localization corresponding to the metallized surface, while SWs propagating in opposite direction is almost unaffected. This nonreciprocal property of spin waves still exist if finite conductivity of the overlayer [145, 32, 38] or exchange interaction [146] are taken into account. In the first case the nonreciprocal dispersion exists only for limiting range of wave vectors, while for the second one the localization type can change. Investigations of the nonreciprocal propagation of SWs have been developed in various semi-infinite ferromagnetic structures: layered, thin film and periodically corrugated. Potential applications of the nonreciprocal effects have been discussed in references [147, 148].

6.1 Nonreciprocity and Damping in Ferromagnets with Conductive Overlayer

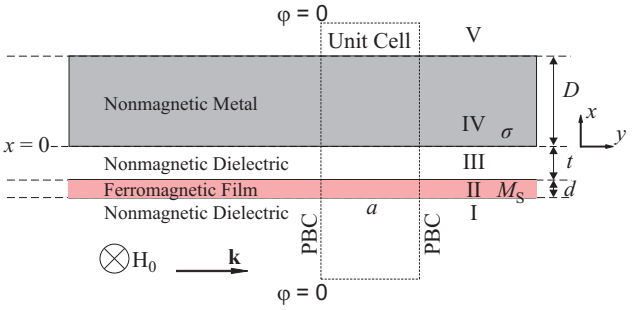

Figure 6.1: A structure under consideration. The bias magnetic field H_0 is in the film plane and directed along the z axis. The SWs propagate along the y axis. The rectangular unit cell used in numerical calculations is marked by dashed line. The PBC are used along the x axis. The bottom and top border of the unit cell is far from the structure, at these borders $\varphi = 0$.

For a uniform ferromagnetic film covered with a layer of a finite-conductivity metal an analytical solution has been obtained for the DE geometry with the field H_0 regarded as a function of the wave vector,[145, 149] since in this case the secular equation leads to a quadratic polynomial formula for H_0. In their case, a real set of parameters leads to a complex value of H_0. The analytical solutions for the SW frequencies f are more complicated; numerical solutions can be obtained.[150, 151, 152]

In this subsection, the numerical study of the uniform ferromagnetic film is presented and its results analyzed. This study is important to understand the range of wavevectors that are under the influence of the metal overlayer of finite conductivity. The geometry of the structure used in the calculations is shown in Fig. 6.1. The structure consists of five regions. Region I and V are nonmagnetic dielectric surroundings, which are assumed to be infinite thick in semi-analytical calculations [described in Sec. 6.1] or to be very thick in finite element calculation [see Sec. 6.1 for details]. Region II is a thin ferromagnetic film, characterized by the saturation magnetization M_{S} and thickness d. The region IV is a nonmagnetic metal characterized by the conductivity σ and thickness D. Region III is a dielectric nonmagnetic spacer, which separates the magnetic film from the metal overlayer and has thickness t. The external magnetic field H_0 is in the plane of the film–along z axis and the wave propagation is assumed to be along y axis, i.e., only DE geometry is considered. The origin of the Cartesian coordinate system is placed at the bottom surface of the metallic film.

The Maxwell equations in the magnetostatic approximation (dicplacement current is neglected but not an electric current of moving charges) will be used in the calculations:

$$\nabla \times \mathbf{h}(\mathbf{r}) = \sigma_n \mathbf{e}(\mathbf{r}), \tag{6.1}$$

$$\nabla \times \mathbf{e}(\mathbf{r}) = -i\mu_0\omega(\mathbf{h}(\mathbf{r}) + \mathbf{m}(\mathbf{r})), \tag{6.2}$$

where μ_0 is the permeability of vacuum, $\mathbf{r}$ is the position vector and t is time. $\mathbf{e}$ is the electric field vector, $\mathbf{h}$ and $\mathbf{m}$ are dynamic magnetic field and dynamic components of the magnetization vectors, respectively. The conductivity σ_n is different from 0 only in the region IV, i.e., $\sigma_{n=\mathrm{IV}} \equiv \sigma$. In the assumed geometry only z component of the electric field is related to dynamic magnetic field, $\mathbf{e} = (0, 0, e_z)$. The solutions in the form of monochromatic waves are assumed: $\mathbf{m}(\mathbf{r}, t) \sim \exp(-i\omega t)$ and $\mathbf{h}(\mathbf{r}, t) \sim \exp(-i\omega t)$, where $\omega = 2\pi f$. Maxwell equations are complemented with the LL equation of motion in the ferromagnetic film (in the region II):

$$-i\omega\mathbf{m}(\mathbf{r}) = \gamma\mu_0\mathbf{M}(\mathbf{r}, t) \times \mathbf{H}_{\mathrm{eff}}(\mathbf{r}, t), \tag{6.3}$$

where γ is a gyromagnetic ratio. $\mathbf{H}_{\mathrm{eff}}$ denotes the effective magnetic field acting on the magnetization and is defined as $\mathbf{H}_{\mathrm{eff}}(\mathbf{r}, t) = H_0\hat{z} + \nabla \cdot (\frac{2A_{\mathrm{ex}}}{\mu_0 M_{\mathrm{S}}})\nabla\mathbf{m}(\mathbf{r}, t) + \mathbf{h}(\mathbf{r}, t)$, where A_{ex} is the exchange constant, M_{S} is the saturation magnetization. The bias magnetic field H_0 is strong enough to saturate the sample along the z axis, thus the magnetization vector $\mathbf{M}$ in linear approximation can be decomposed into the static and dynamic parts, parallel to the z-axis and laying in the plane (x, y), respectively: $\mathbf{M}(\mathbf{r}, t) = M_0\hat{z} + \mathbf{m}(\mathbf{r}, t)$. $M_0 \equiv M_{\mathrm{S}}$, $\mathbf{m} = (m_x, m_y, 0)$ and $\mathbf{h} = (h_x, h_y, 0)$ is assumed.

FEM

To find the dynamical components of the magnetization vector and the dispersion relation of SWs FEM will be used. Artificial periodic boundary conditions (PBC) are imposed at surfaces parallel to the x axis at the borders of the unit cell of width a as shown in Fig. 6.1. Use of PBC allows to define film of infinity length in numerical calculations. The solutions of the coupled LL and Maxwell equations in the periodic system can be written according to the Bloch theorem as: $\varphi(x,y) = \varphi'(x,y)\mathrm{e}^{iky}$, where $\varphi' = m'_x$, m'_y, h'_x, h'_y and e'_z are periodic functions of x and k is a wavenumber.

One can expect that dynamic magnetic and electric fields should vanish at $x \to \infty$. To mimic this condition in FEM, the Dirichlet boundary condition ($\varphi' = 0$) was used at the bottom and top border of the computational unite cell, which is far away (150 μm from the ferromagnetic film) from the magnetic film [Fig. 6.1]. The boundary conditions for dynamic components of the magnetization vector are imposed only via LL and Maxwell equations, these provide zero of the first derivative of the dynamical magnetization with respect to the normal to the surface.[7, 66, 86]

After applying the Bloch theorem in linearized LL equation and in Maxwell equations the following set of equations is formed:

$$\begin{pmatrix} \frac{i2\pi f}{\gamma\mu_0} & \nabla\cdot(\frac{2A_{ex}}{M_S\mu_0})\nabla + 2ik\partial_y - (\frac{2A_{ex}}{M_S\mu_0})k^2 - H_0 & 0 & M_S & 0 \\ -\nabla\cdot(\frac{2A_{ex}}{M_S\mu_0})\nabla - 2ik\partial_y + (\frac{2A_{ex}}{M_S\mu_0})k^2 + H_0 & \frac{i2\pi f}{\gamma\mu_0} & -M_S & 0 & 0 \\ i2\pi f\mu_0 & 0 & i2\pi f\mu_0 & 0 & \partial_y + ik \\ 0 & i2\pi f\mu_0 & 0 & i2\pi f\mu_0 & -\partial_x \\ 0 & 0 & -\partial_y - ik & \partial_x & -\sigma \end{pmatrix} \begin{pmatrix} m'_x \\ m'_y \\ h'_x \\ h'_y \\ e'_z \end{pmatrix} = 0. \tag{6.4}$$

This set of equations is solved with the use of finite element method implemented in COMSOL MultiPhysics software. As a result egeinvalues are obtained that gives the dispersion relation of SWs and eigenvectors which represent the spatial distribution of dynamical components of m'_x, m'_y, h'_x, h'_y and e'_z. Since the structure is periodic in the real space with periodicity of a, the solutions (frequencies of SW) possess the periodicity in the 1D reciprocal space characterized by the period $2\pi/a$ with artificial folding to the first Brillouin zone. In order to investigate SWs in a uniform film (so called empty lattice model) the SW frequencies for the wavevectors from the first Brillouin zone are calculated and the artificial solutions from higher bands are eliminated. The lattice constant $a = 200$ nm was chosen in all calculations, so the computational unit cell is not large and the higher branches of empty lattice model do not cross with the first branch in the considered frequencies in this chapter.

Semi-analytical method

In semi-analytical model the dynamic magnetic field induction:[150]

$$\mathbf{b} = \mu_0(\mathbf{h} + \mathbf{m}) \tag{6.5}$$

is represented in terms of the vector potential function $\mathbf{A}$:

$$\mathbf{b} = \nabla \times \mathbf{A} = (\partial_y A_z, -\partial_x A_z, \partial_y A_x - \partial_x A_y). \tag{6.6}$$

With this vector potential the Gauss's law $\nabla \cdot \mathbf{b} = 0$ is identically fulfilled. From LL equation one can define magnetic permeability tensor $\hat{\mu}$ and express $\mathbf{h}$ field in terms of the $\mathbf{b}$ field. When $A_{\text{ex}} = 0$ it reads:

$$\mathbf{h} = \hat{\mu}^{-1}\ \mathbf{b} = \begin{pmatrix} \frac{1+\kappa}{(1+\kappa)^2-\nu^2} & \frac{i\nu}{(1+\kappa)^2-\nu^2} & 0 \\ -\frac{i\nu}{(1+\kappa)^2-\nu^2} & \frac{1+\kappa}{(1+\kappa)^2-\nu^2} & 0 \\ 0 & 0 & \frac{1}{2} \end{pmatrix}\ \mathbf{b}, \tag{6.7}$$

where:

$$\kappa = \frac{\Omega_H}{\Omega_H^2 - \Omega^2},\ \nu = \frac{\Omega}{\Omega_H^2 - \Omega^2} \tag{6.8}$$

and

$$\Omega = \frac{2\pi f}{\gamma \mu_0 M_{\text{S}}},\ \Omega_H = \frac{H_0}{M_{\text{S}}}. \tag{6.9}$$

From Eqs. (6.5)-(6.7) one can see that h_x, h_y, m_x and m_y are defined by A_z component of the vector potential. From equations (6.1) and (6.2) The following equation for A_z is obtained:

$$\left(\frac{1+\kappa}{(1+\kappa)^2 - \nu^2}\right)\nabla^2 A_z = i2\pi f \sigma \mu_0 A_z. \tag{6.10}$$

The total solution of the Eq. (6.10) can be found from the solutions in regions I to V imposed into boundary conditions at interfaces along x axis and at infinity. The solution of A_z in the region IV (metal) can be written in the following form:

$$A_z(x, y) = (a_4 \mathrm{e}^{k_{\text{M}} x} + b_4 \mathrm{e}^{-k_{\text{M}} x})\mathrm{e}^{-iky}, \tag{6.11}$$

where a_4 and b_4 are constants. k is a wavenumber of wave propagating along y axis and can take any real value. The wavenumber along x axis in the metal, k_{M} is derived from Eq. (6.10) with the use of Eq. (6.11):

$$k_{\text{M}} = \sqrt{k^2 + \frac{2i}{\delta_0^2}}, \tag{6.12}$$

where

$$\delta_0 = \sqrt{\frac{1}{\pi f \mu_0 \sigma}} \tag{6.13}$$

is a frequency dependent skin depth of the metal. For the remaining regions (regions I - III and V, where $\sigma \equiv 0$) the A_z can be taken in the form:

$$A_z(x, y) = (a_n \mathrm{e}^{kx} + b_n \mathrm{e}^{-kx})\mathrm{e}^{-iky}, \tag{6.14}$$

where a_n and b_n are constants. n denotes the region: I, II, III or V. In region I and V one can expect that the any $\psi\prime$ function decay for $x \to -\infty$ and $x \to \infty$, thus $b_1 = a_5 = 0$.

By imposing the solutions (6.11) and (6.14) into electromagnetic boundary conditions, it is a continuity of tangential component of the magnetic field h_y and the normal component of the magnetic induction field b_x the secular equation is obtained. This equation is solved using Newton iterative method. From the condition of existence of nontrivial solutions the dispersion relation of SW in magnetostatic approximation can be obtained as well.

Analyzis of the Calculation Results

In Fig. 6.2(a) the effect of a metallization (Δ_f) of the SWs propagating in thin film as a function of the conductivity of the metal overlayer and the wavenumber of a SW calculated with FEM is presented. One can define the measure of the metallization effect as a difference between frequency of SW propagating in positive y direction in the ferromagnetic film with metallic overlayer and with dielectric surroundings from both sides, i.e., $\Delta_f(\sigma, k) = f(\sigma, k) - f(0, k)$.[2] The calculations were performed for the ferromagnetic film with the following parameters: $M_S = 1.2 \times 10^6$ A/m, $d = 30$ nm, $t = 0$, $D = 150$ μm, $A_{ex} = 2.8 \times 10^{-11}$ J/m and with the in-plane bias magnetic field $\mu_0 H_0 = 0.1$ T.[3] Conductivity values of some common metals (Ag, Cu and Au) at room temperature are indicated by horizontal dashed lines in Fig. 6.2. One can see that for Ag, a metal with highest conductivity, Δ_f has its maximum at $k \approx 1 \times 10^6$ 1/m and Δ_f extends the value of 0.8 GHz. For other metals Δ_f is smaller but always its maximal value is for the similar value of $k \approx 10^6$ m^{-1}.

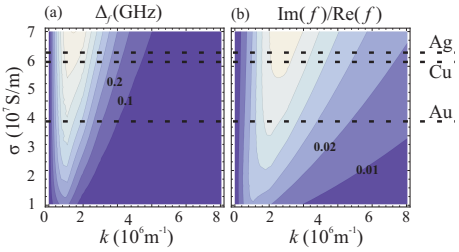

Figure 6.2: Color map of the metallization effect Δ_f and the inverse of FOM [1/FOM] as a function of the wavenumber k and the conductivity of the metallic overlayer σ is shown in (a) and (b), respectively. Horizontal black dashed lines mark the conductivity of a few common metals: Ag, Cu and Au.

[2]This definition of Δ_f is related also to the difference between frequencies of SW propagating in positive and negative direction in the same structure [i.e. to the nonreciprocity strength introduced at the end of the Sec. 6.1]. It is because the propagation of the wave with amplitude localized at the surface with dielectric is weakly affected by the presence of the metal on the opposite side.[8]

[3]The FEM results were compared with the semi-analytical results performed with neglecting exchange interactions, showing that the value of an exchange constant does not influence results in the considered here wavenumbers and frequencies.

In Fig. 6.2(b) the reversal of the figure of merit (FOM) defined as $\frac{1}{\mathrm{FOM}} = \frac{\mathrm{Im}(f)}{\mathrm{Re}(f)}$ in dependence on σ and k is shown. This function describes the attenuation of SW, it is an attenuation induced by metallization of the overlayer, because the intrinsic damping is not considered here. Thus for parameters where the dielectrics are on both sides of the ferromagnetic film FOM $\to \infty$ (1/FOM $\to 0$). The FOM is an important parameter regarding the potential applications, because in order to propagate signal for large distances, SWs need to have a long life time, i.e., the real part of frequency shell to be much higher than the imaginary part: $\mathrm{Re}(f) > \mathrm{Im}(f)$.[153] It means that 1/FOM has to be smaller than 1. In Figs. 6.2(a) and (b) one can see that Δ_f and 1/FOM have similar dependence on σ and k but the maximal value of 1/FOM is shifted to higher wavenumbers as compared to Δ_f.

To explain presented above results of FEM calculations an analysis of the dispersion relation and the fields emitted by the SW excitations outside of the magnetic film with the use of semi-analytical method described in Sec. 6.1 will be performed. The structure with conductivity $\sigma = 6 \times 10^7$ S/m (i.e., close to the value of Cu or Ag) and parameters described above will be considered as a base for further analysis of this chapter. Any variation of these parameters will be indicated.

Approximate analytical solution

Results of calculations for the structure with parameters specified above, where metal is in direct contact with ferromagnetic film and its thickness is much larger than the skin depth of metal are presented in Fig. 6.3(a). The three dispersion relations show: the results of semi-analytical calculations (which coincide with the FEM results)–dashed line; the dispersion of SWs for the same film but in contact with dielectric–solid line and in contact with perfect electric conductor (PEC)–dotted line. One can see, that at small wavenumbers ($k < k_1$) the dispersion of DE wave with metallic overlayer of finite conductivity (dashed line) follows the dispersion in ferromagnetic film in contact with PEC (dotted line), while for larger wavenumbers (k larger than k_3) it follows the dispersion relation in the film with both dielectric surroundings (solid line).

In order to understand the range of wavenumbers for which the SW dispersion is under influence of a metal overlayer with finite conductivity and infinite thickness, the penetration depth of electromagnetic field into a metal will be analyzed and compare with the penetration depth into a dielectric. Decay of the electric field associated with the SW excitation is exponentially depended on its wavevector and characterized by the penetration depth. In the case of ferromagnetic film surrounded by a dielectric the penetration depth is $\delta_k = 1/k$. If the magnetic film is surrounded by a metal, an additional attenuation of the field is present and this is described by metal's skin depth δ_0 [Eq. (6.13)]. The total penetration depth in this case is δ_M and is related to the metal wavenumber introduced in Eq. (6.12): $\delta_\mathrm{M} = 1/k_\mathrm{M}$. Which of the two decay contributions, $k = 1/\delta_k$ or $1/\delta_0$ to k_M is more important, will determine the influence of a metal on the SW excitation.

In the subsequent figures in Fig. 6.3(b) $|e_z(x)|$ (dashed line) is plotted along x

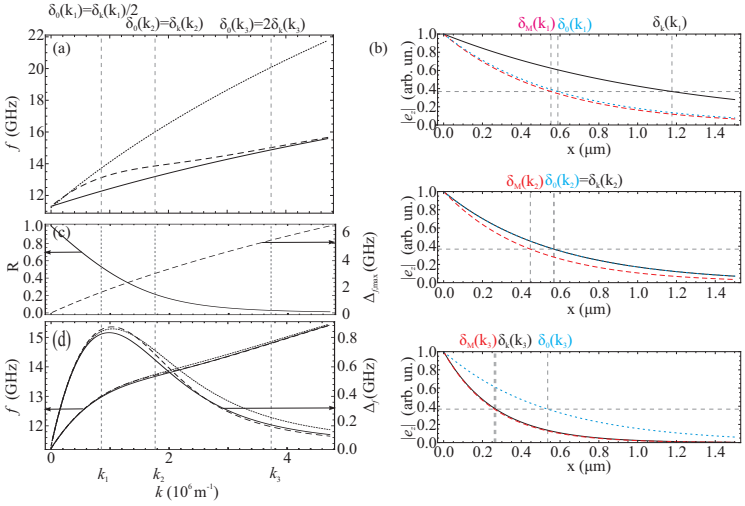

Figure 6.3: (a) Dispersion relation of DE wave in ferromagnetic film of $d = 30$ nm thickness and saturated by the external magnetic field $\mu_0 H_0 = 0.1$ T. Solid line shows calculations result for the film with both dielectric surroundings, dotted line for a film covered from one side with PEC and dashed line with metal with $\sigma = 6 \times 10^7$ S/m conductivity. (b) Amplitude of the z component of the electric field decaying with increasing distance from the surface of the ferromagnetic film as $\exp(-x/\delta_k)$—solid line, $\exp(-x/\delta_{\mathrm{M}})$—dashed line and as $\exp(-x/\delta_0)$—dotted line are shown for three values of the wavenumber. It is for $k_1 = 0.85 \times 10^6$ m^{-1}, $k_2 = 1.76 \times 10^6$ m^{-1} and $k_3 = 3.72 \times 10^6$ m^{-1} marked also by vertical lines in (a), (c) and (d). (c) R and $\Delta_{f,\max}$ as a function of the wavenumber are shown with solid and dashed line, respectively. (d) The approximate and exact values of f and Δ_f in dependence on the k. Solid line shows $f_{\mathrm{app}}(k)$ calculated from Eq. (6.17) with δ_0 estimated with Eq. (6.18), dot-dashed line with δ_0 estimated with Eq. (6.19), and dashed line shows the $f(k)$ obtained in semi-analytical model.

axis in the space occupied by the metal ($x > 0$) for three values of the wavevector. In the top figure for $k_1 = 0.85 \times 10^6$ m^{-1}, in the middle figure for $k_2 = 1.76 \times 10^6$ m^{-1} and in the figure at the bottom for $k_3 = 3.72 \times 10^6$ m^{-1}. These wavenumbers are marked by vertical lines also in Fig. 6.3(a). In each plot $e_z(x) \propto \exp(-x/\delta_{\mathrm{M}})$ dependence (dashed line) is decomposed onto two components: a decay due to nature of DE's SW ($\exp(-x/\delta_k)$, solid line) and due to finite conductivity attenuation in metal ($\exp(-x/\delta_0)$, dotted line). All functions are calculated with the use of semi-analytical method and normalized so that $|e_z|$=1 at the surface of the ferromagnetic film (at $x = 0$). The analytical dependencies are in perfect agreement with results obtained from FEM calculations, not shown here. The 1/e value of e_z is marked by the horizontal dashed line. One can see that in the first case decay is determined by a decay in metal because $\delta_{\mathrm{M}}(k_1) \approx \delta_0(k_1) < \delta_k(k_1)$, in the second case the skin depth of metal is close to the penetration depth of DE wave ($\delta_0(k_2) \approx \delta_k(k_2)$), this is intermediate case where both sources of attenuation have the same contribution to δ_{M}. Whereas in the third case $\delta_{\mathrm{M}}(k_1) \approx \delta_k(k_3) < \delta_0(k_3)$ and the total attenuation

is due to localization of the DE excitation at this wavelength, i.e., the penetration depth into dielectric is shorter than the skin depth of metal, an effect of metal is not visible. This analysis allows to define three wavenumber regions: i) $k < k_1$, the frequency is strongly influenced by metal, it corresponds to a dispersion of ferromagnetic film in contact with PEC. ii) $k_1 < k < k_2$, the influence of metal is visible, but not as strong as magnetic film would be in contact with PEC, but here the maximal influence of metallization (also a maximal nonreciprocity) on SW is expected, and iii) $k_3 < k$, the effect of metal is negligible.

The quantitative contribution of a metal attenuation to the total attenuation of SW in the region IV [Fig. 6.1] can be estimated by calculating the ratio, R, of the electric field attenuation in metal due to the conductivity:

$$R = 1 - \frac{\int_0^\infty \left|\mathrm{e}^{-kx}\right| dx}{\int_0^\infty \left|\mathrm{e}^{-k_\mathrm{M} x}\right| dx} = \frac{\delta_\mathrm{M} - \delta_k}{\delta_\mathrm{M}}. \tag{6.15}$$

The function R changes from 0 to 1; R close to 0 means that almost all the electric field attenuation is due to decay of the SW excitation, close to 1 means that almost all electric field attenuation is due to the presence of metal. R as a function of SW wavenumber is plotted in Fig. 6.3(c) with solid line. Function is monotonic and changes from 1 at $k = 0$ to 0 at $k \to \infty$, as expected. In order to obtain the approximate value of the metallization effect, the frequencies in the structure with PEC and without metal will be used, thus it will define $\Delta_{f,\mathrm{max}}$, i.e., a maximal available metallization effect. Here, the analytical formulas for SW dispersion of an uniform film surrounded by dielectrics and in direct contact with PEC will be used, $f_\mathrm{DE}(k)$ and $f_\mathrm{PEC}(k)$, which are defined in Refs.[29] and [30], respectively. Thus, $\Delta_{f,\mathrm{max}}(k) \equiv f_\mathrm{PEC}(k) - f_\mathrm{DE}(k)$ and its dependence on k is shown in Fig. 6.3(c) with dashed line. The approximate strength of the metallization effect, $\Delta_{f,\mathrm{app}}$ is then given by:

$$\begin{aligned} \Delta_f &\approx \Delta_{f,\mathrm{app}} = \Delta_{f,\mathrm{max}} R = (f_\mathrm{PEC} - f_\mathrm{DE}) R \\ &= (f_\mathrm{PEC} - f_\mathrm{DE}) \frac{\delta_\mathrm{M} - \delta_k}{\delta_\mathrm{M}}. \end{aligned} \tag{6.16}$$

The approximate real part of SW's frequency can be also calculated with approximate formulas:

$$\begin{aligned} f &= f_\mathrm{DE} + \Delta_f \approx f_\mathrm{app} \\ &= f_\mathrm{DE} + (f_\mathrm{M} - f_\mathrm{DE}) \frac{\delta_\mathrm{M} - \delta_k}{\delta_\mathrm{M}}, \end{aligned} \tag{6.17}$$

where δ_M depends on δ_0 [Eq. (6.12)] and so it is still a function of f. However this frequency can be approximated, two approaches to estimate f in Eq. (6.12) might be used:
i) from the analytical solution for DE mode in ferromagnetic film surrounded by

dielectrics:

$$\delta_0 \approx \delta_{\mathrm{DE}} = \sqrt{\frac{2}{2\pi\mu_0 f_{\mathrm{DE}}\sigma}}, \tag{6.18}$$

ii) from the averaged frequency of the film with PEC and with dielectrics:

$$\delta_0 \approx \delta_{\mathrm{avrg}} = \sqrt{\frac{2}{2\pi\mu_0 \frac{f_{\mathrm{DE}}+f_{\mathrm{PEC}}}{2}\sigma}}. \tag{6.19}$$

In Fig. 6.3(d) both, $\Delta_{f,\mathrm{app}}(k)$ and $f_{\mathrm{app}}(k)$ is plotted for the structure in contact with metal, obtained from Eqs. (6.16) and (6.17) with using skin depths Eqs. (6.18) and (6.19) (solid and dotted lines, respectively) and compare them with numerical solutions ($\Delta_f(k)$ and $f(k)$ obtained with semi-analytical method, marked by dashed line). One could expect that the choice of f function in δ_0 may influence results. In fact, the differences are observed but these are very small and almost invisible in frequency dependence on the wavevector due to frequency scale used in figure [the left scale in Fig. 6.3(d)]. However, one can see the discrepancy between numerical results and approximate solutions in the plot of the metallization (the right scale) for $k > k_1$. At small k numerical and both approximate solutions are very close to each other, this shows that the function δ_0 is approximated correctly at these wavenumbers. The differences between numerical solution of $\Delta_f(k)$ and $\Delta_{f,\mathrm{app}}(k)$ based on DE approximation Eq. (6.18) and the average value Eq. (6.19) (both approximate values coincide) increases up to wavenumber where Δ_f reach maximal value. It is since the frequency used in δ_0 is becoming significantly different from right solution. This discrepancy is eliminated when iterations of frequency are used. For large k the $\Delta_{f,\mathrm{app}}$ based on DE approximation is again close to numerical solution, while $\Delta_{f,\mathrm{app}}$ based on average value is higher from numerical solution and this difference saturate with increasing k. Also the influence of error in δ_0 due to frequency approximation is smaller at small k than at large k, since the value of R is larger at small k.

Maximizing the influence of metal

Based on the discussion from the previous subsection one can point at parameters which will be important in order to increase the effect of metallization (to decrease skin depth of metal δ_0) on the dispersion of SWs and so, to increase the strength of nonreciprocity. Since now solely FEM method will be used for analysis. According to Eq. (6.13) the skin depth is proportional to the square root from the inverse of frequency:

$$\delta_0 \propto \sqrt{\frac{1}{f}},$$

thus increasing the frequency at fixed k will lead to shorter skin depth in metal and the effect of metallization will be stronger (higher attenuation due to electron screening and higher value of function R). One can expect that the frequency at fixed k will increase by:

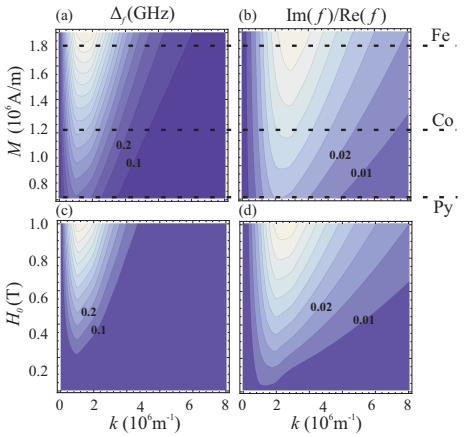

Figure 6.4: The strength of a metallization effect Δ_f as a function of (a) k and M_S, (c) k and H_0. The inverse of FOM [1/FOM] as a function of (b) k and M_S, (d) k and H_0. In (a) and (b) the dashed horizontal lines mark saturation magnetization of Py, Co and Fe.

- applaying higher bias magnetic field,
- using material with higher magnetization,
- increasing the thickness of the magnetic film.[4]

The results of numerical calculations confirm the predictions. In Figs. (6.4) (a) and (c) the Δ_f is plotted in two-dimensional maps as a function of (M_S, k) and (H_0, k), respectively.

In Figs. (6.4) (b) and (d) the reverse of the FOM function is plotted for the same dependence and it can be directly compared with Gilbert damping factor, since 1/FOM $\approx \alpha$.[154] For the structure with parameters taken from Fig. (6.3) (a) the imaginary part of the frequency is always much smaller than the real part and 1/FOM reaches the value 0.06 (FOM $\approx$ 16.7), which is of the same order as a Gilbert damping in many ferromagnetic materials.[155, 156] In other considered here parameters increase of 1/FOM with increase of M_S and d is observed, but a decrease with an increase of H_0.

In Fig. (6.4) (a) the magnetization saturation of Fe, Co and Py are indicated. The effect of metallization is negligible for thin films made of materials with low magnetisation, it is already for Py. Thus, the new materials with high magnetization, like a CoFeB alloys proposed recently for magnonics applications[157, 158] or Heusler alloys [159, 160, 161] might be useful for a fabrication the structures with high nonreciprocal effect and high velocity of SW with reasonable value of damping.

[4]In this chapter the investigation is limited to the thin ferromagnetic films ($d \leq 30$ nm) when the effect of its finite conductivity on the SW propagation is negligibly as was proved by a number of experiments on thin Py films. In the thicker ferromagnetic films the eddy currents generated in ferromagnetic film can influence the SW dispersion.[36]

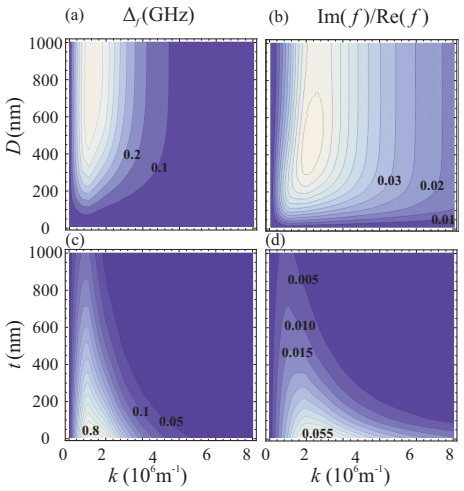

Figure 6.5: Δ_f as a function of (a) k and the thickness of the metallic layer D, (c) k and the separation between metal and ferromagnetic film t. 1/FOM as a function of (b) k and D, and (d) k and t.

In Figs. (6.5) (a)-(d) the strength of the metallization effect and 1/FOM in dependance on the thickness of the metal film D, a metal separation from the magnetic film t and a wavenumber are presented. For D dependance one can observe a saturation of Δ_f at values of order of skin depth in metal (δ_0 is usually in the range of 550-620 nm). However, a small variation of 1/FOM is still visible for thicker metallic film. The interesting point is that the region on the (D, k) plane, where $1/\mathrm{FOM} > 0.063$ has widest range of k when $D \approx \delta_0$. The t dependence of Δ_f and 1/FOM is opposite to dependence on D described above. Both functions decrease with increasing t, however they have a maximum in dependence on k, this maximum exists for SWs with small k wavevectors, i.e., when $\frac{1}{k} > t + \delta_0$ and shifts slightly to the smaller k with increasing t.

In addition to the magnetization, external field, metallic film thickness and metal separation, the change of the thickness of a ferromagnetic film will also have impact on nonreciprocity effect at given wavevector. With the increase of thickness, the group velocity of DE wave increases. At given wavevector the frequency of SW is higher for thicker sample, thus the penetration depth of the excitation decreases and an influence of metal is stronger. However, with the increase of ferromagnetic film thickness, the influence of a conductivity of the ferromagnetic film on the dispersion of SWs becomes not negligible. Moreover, the damping also increases limiting potential applications of such structures. Thus the investigations were limited to a thin ferromagnetic films. The thickness dependance on nonreciprocity strength might be also considered in nonconductive magnetic films, e.g., in YIG, then the thicker sample is, the stronger effect is expected.[145, 149]

There is also another factor, not considered in this chapter, which can contribute to the nonreciprocal properties of SW in thin films, this is an exchange interaction. The exchange interactions result in appearing of $A_{ex}k^2$ term in the

magnetostatic SW dispersion relation.[26] Thus high exchange constant should lift the frequency up at the fixed k and decrease δ_0, so the metallization can be visible at larger k values. However, as it was verified numerically, to observe this effect the value of A_{ex} should be at least two orders of magnitude higher than that of ferromagnetic materials considered in this chapter.

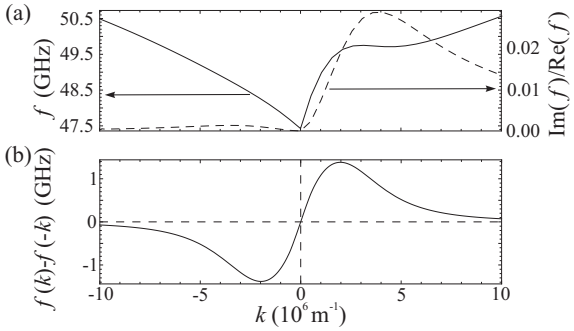

Figure 6.6: The dispersion relation (solid line) and the 1/FOM (dashed line) of DE's SW in the 30 nm thick CoFeB film with a Cu overlayer of 500 nm thickness. The following parameters were assumed in the numerical calculations: $\mu_0 H_0 = 1$ T, $M_S = 1.43 \times 10^6$ A/m, $A_{ex} = 2.8 \times 10^{-11}$ J/m and $\sigma = 6 \times 10^7$ S/m. (b) The nonreciprocity strength for CoFeB thin film in direct contact with the Cu overlayer.

On the basis of analysis presented above one can propose the material and the structure suitable for an observation of the nonreciprocal dispersion relation of SWs in thin ferromagnetic film with currently available resolution of the BLS setups.[78] The high magnetization material was chosen, it is CoFeB alloy,[158] to be studied at relatively high external field, $\mu_0 H_0 = 1$ T, and covered with the thick film of Cu. In Fig. (6.6)(a) the dispersion relation [solid line] and 1/FOM [dashed line] is shown for a 30 nm thick film with high nonreciprocal dispersion of SWs at wide wavevector range. The nonrecirpocity strength defined as the difference between frequency of SW propagation in $+k$ direction and $-k$ is shown in Fig. (6.6)(b). The maximal nonreciprocity is found at $k \approx 2.0 \times 10^6$ 1/m with $f(k) - f(-k) \approx 1.3$ GHz. The nonreciprocity higher than 0.2 GHz can be observed for wavevectors in the range of 7.0×10^6 1/m. There is also interesting effect related to the SW attenuation, it is the big noreciprocity in an attenuation of SW due to the presence of metal. SWs propagated in $-k$ direction are almost undamped, while in $+k$ are attenuated with maximum 1/FOM at 4×10^6 1/m. However this maximum does not coincide with the maximal value of a nonreciprocity strength shown in Fig. (6.6)(b).

6.2 Magnonic Crystals with Perfect Electric Conductor Overlayer

The effect of PEC ovelayer on MCs and appearing of nonreciprocal dispersion is described in this subsection. The nonreciprocal properties of SWs propagating in thin films of MCs are studied, with space inversion symmetry broken by a metallic overlayer. The homogeneous yttrium iron garnet film in contact with a metal grid has already been studied in transmission measurements [162, 24, 12]. The magnonic band gaps (MBGs) have been observed but the influence of the nonreciprocity was not discussed. The finite conductivity of the metal grid was considered in reference [163], where the strong nonreciprocity of the SW damping was predicted. Influence of nonreciprocity caused by a metal overlayer on SW Bragg resonances in YIG film with lattice of etched grooves with the period a was recently studied experimentally [164, 153]. It was shown, that if a dielectric spacer with thickness t is inserted between YIG film and the metal overlayer, MBGs were detected only for SWs with wavenumbers $k_n > 1/t$ where the effect of finite conductivity is strong and when the incident k^+ and reflected k^- waves have similar frequency and fulfill approximate Bragg diffraction condition (see figure 3 in reference [153]):

$$k_n \approx n\frac{\pi}{a}, \tag{6.20}$$

where n is an integer number. For SWs with wavenumbers $k < 1/t$ a nonreciprocity in dispersion leads to sufficiently big difference in wavenumbers of k^+ and k^- waves. It was concluded, that in MC with metal overlayer the Bragg resonances determined by equation (6.20) couldn't be observed for nonreciprocal waves [153].

It will be presented in the chapter that the formation of MBG in a media with nonreciprocal property is possible and it exists when the incident and reflected SW fulfill the so-called exchange Bragg condition [131]:

$$k^+ + k^- = n\frac{2\pi}{a}. \tag{6.21}$$

It will be shows and explained that this MBG will appear inside of the Brillouine zone (BZ) and it is indirect band gap. It will be also shown that in the part of the SW spectra corresponding to the half of BZ more than one MBG can exist.

Model

Finite element method (FEM) has been implemented in the frequency domain to solve the Landau-Lifshitz (LL) and Maxwell equations to find the dynamical components of the magnetization vector ($\mathbf{m}$) and to obtain the dispersion relation of one-dimensional (1D) bi-component MC shown in figure 6.7. In the frame of this approach the nonuniform spatial distribution of microwave magnetization as well

coupling between dipole and exchange subsystems of the MC can be taken into account [34, 38]. This method can be used to predict the SW spectra in MCs with nano- and meso-scale periodicity and finite thickness. It is an important extension of methods used previously in theoretical studies of nonreciprocal effects in magnonic structures [86, 147].

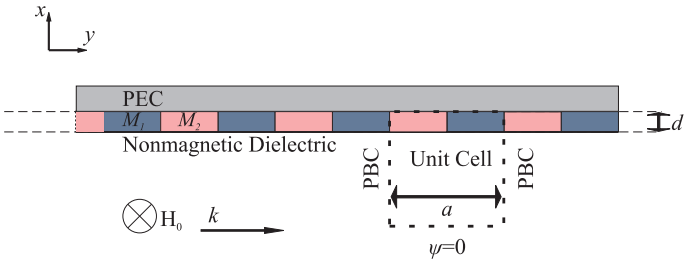

Figure 6.7: A structure of 1D MC with a layer of a PEC on the top surface. The MC is composed of alternating, infinitely long ferromagnetic stripes that have different saturation magnetization M_1 and M_2. The bias magnetic field H_0 is directed along z axis. The SWs propagate along the y axis. The rectangular unit cell used in numerical calculations is marked by a dashed line. The PBC are used along the y axis.

Analyzis of the Calculation Results

To make more clear specific properties of nonreciprocal SW spectra, two types of 1D MCs will be discussed, which are characterized by low $\Delta M \ll M_{1,2}$ and high $\Delta M \sim M_{1,2}$ magnetic contrasts [$\Delta M = |M_1 - M_2|$, M_1 and M_2 are saturation magnetizations of stripe 1 and 2] [7]. 1D MC with low magnetic contrast consists of stripes of the same thickness $d = 70$ nm, width $w = 300$ nm (lattice constant $a = 600$ nm), $\gamma = 182.2$ GHz/T and the exchange constant $A_{\text{ex}} = 7 \times 10^{-11}$ J/m but different saturation magnetization: $M_1 = 0.9 \times 10^6$ A/m and $M_2 = 1.0 \times 10^6$ A/m. These values can correspond to iron and nickel alloys with various compositions [165]. As an example of MC with $\Delta M \sim M_{1,2}$ the structure composed of Co and Py stripes can be taken, which was already investigated theoretically and experimentally [166, 86] with parameters $M_1 = 1.25 \times 10^6$ A/m, $M_2 = 0.65 \times 10^6$ A/m, $A_{\text{ex},1} = 2.88 \times 10^{-11}$ J/m, $A_{\text{ex},2} = 1.11 \times 10^{-11}$ J/m, $\gamma = 182.2$ GHz/T, $w = 250$ nm, $a = 500$ nm, $d = 30$ nm. All calculations were done for the external magnetic field $\mu_0 H_0 = 0.1$ T.

At first the dispersion curves within the first BZ for low magnetic contrast structure is calculated. the results are shown by dots in figure 6.8(a). For convenience, the SW dispersion for uniform magnetic film with saturation magnetization M_S being an average of M_1 and M_2, $M_S = (M_1 + M_2)/2 = 0.95 \times 10^6$ A/m, and other chosen parameters is shown by thick solid line. Two horizontal dashed lines pointing at f_S and f_{ex} are used as reference lines. They correspond to frequencies of short wavelength limit for MSSW (without exchange contribution) in magnetic film

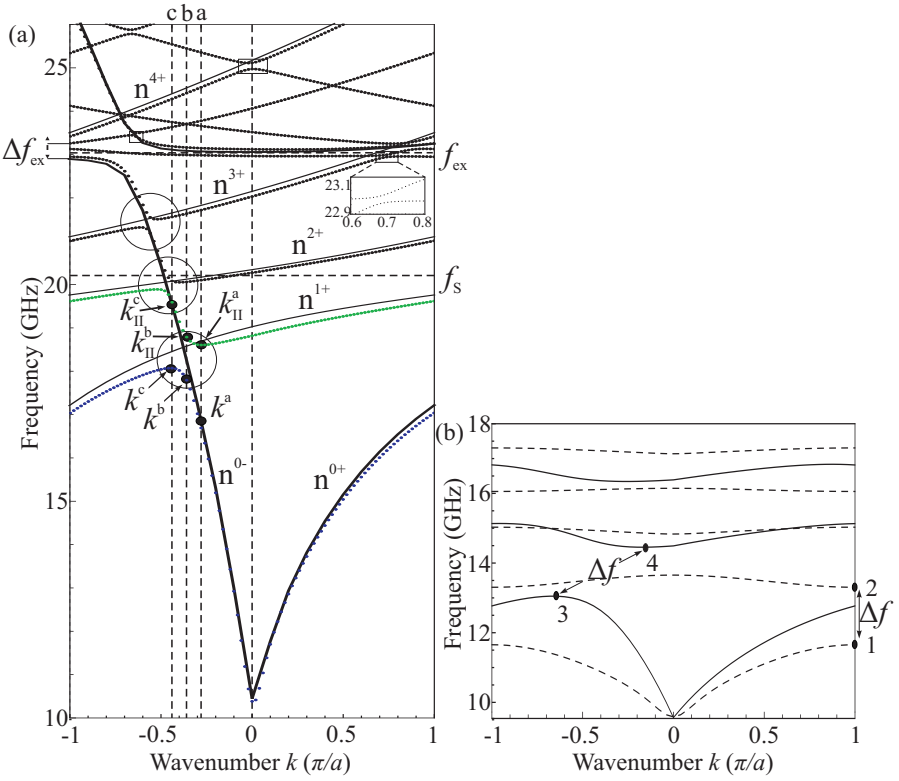

Figure 6.8: (a) The calculated magnonic band structure (dots) of the 1D MC with small magnetic contrast. For convenience the position of the upper frequency limit for MSSW f_S and frequency of the first exchange standing spin wave f_{ex} are shown for not metallized uniform magnetic film with structural parameters defined for MC with average magnetization $M_S = \frac{M_1+M_2}{2} = 0.95 \times 10^6$ A/m. The dispersion of metallized homogeneous ferromagnetic film like this is plotted by thick continuous line, additional thin continuous lines present solutions folded to the first BZ only for primary branches, they are marked as $n^{i\pm}$. The solid black dots described by k^a – k_{II}^c and vertical lines indicate the points for which profiles in figure 6.9 are plotted. (b) The dispersion relation of Co/Py (high magnetic contrast) 1D MC with one side metallized (solid lines) and with both dielectric surroundings (dashed lines).

with nonmagnetic dielectric surrounding $2\pi f_S \equiv \omega_S = \omega_H + \omega_M/2$ [29] and first exchange spin standing wave resonance mode $2\pi f_{ex} \equiv \omega_{ex} = \sqrt{\omega_H^*(N)(\omega_H^*(N)+\omega_M)}$, where $\omega_H = \gamma\mu_0 H_0$, $\omega_M = \gamma\mu_0 M_S$, $\omega_H^*(N) = \omega_H + \gamma\frac{2A_{ex}}{M_S}(\frac{\pi N}{d})^2$ and $N = 1$ [34, 38]. The metallization introduces strong nonreciprocity in SW spectra of thin film. The MSSW group velocities ($V_g = \frac{\partial\omega}{\partial k}$) at $k \to 0$ are different for opposite directions of propagation, $|V_g^+| \approx 3.1$ km/s and $|V_g^-| \approx 5.6$ km/s. The MSSW are propagating along the metallized surface (i.e., for k^-; their localization properties will be discussed later in the chapter) possess strong hybridization with the first exchange standing mode f_{ex}, leading to the exchange gap Δf_{ex} formation at frequency f_{ex} and $k \approx -0.7\pi/a$, similar to the case of uniform ferromagnetic film [34].

The periodicity of the structure leads to appearance of the back-folded bands. For $|k| \leq \pi/a$ and frequency interval from 10 GHz to 26 GHz shown in figure 6.8(a), only back folded waves traveling along not metallized surface (i.e., traveling in k^+ direction) and the first exchange standing mode take part in an interaction with SWs propagating along metallized surface (i.e., traveling in k^- direction). In figure 6.8(a) dispersion curves corresponding to the MSSW of uniform film traveling along free surface (k^+) and having its origin at $k_n = -(2\pi n)/a$ are shown by thin solid lines with numbers $n = 1^+...4^+$, where n corresponds to the order of BZ and index "+" pointed waves traveling along positive direction of y axis. Dispersions of these waves are folded back to the first BZ and these could be interpreted as MSSWs in unmetallized uniform film with the wavenumbers shifted by the reciprocal lattice vector k_n. At points where dispersion of these waves cross the dispersion of n^{0-} wave, the condition (2) is fulfilled and resonance scattering leads to MBGs appearance.

Among these Bragg resonances two types can be distinguished. For the first one nonreciprocity of SW propagation is not necessary, while for others it plays important role. The Bragg resonances of the first type arise due to interaction of the first standing spin wave resonance mode, f_{ex} with reflected MSSW traveling along the unmetallized surface (in positive **y** direction). Due to exchange interactions, dispersion curves for MSSW do not have frequency limit f_{S} for $k \to \infty$, as it is seen from curves pointed by $n = 1^+, .., n = 4^+$ which are shifted above the limiting frequency f_{S} and condition (2) can be fulfilled at frequencies close to f_{ex}. An example of the resonances of the first type is shown by rectangular frame in figure 6.8(a) with inset, which shows the enlarge view of the dispersion. This resonance is similar to resonance between two electromagnetic waves, with different polarizations in PC, from which at least one is folded-back to the first BZ [131, 133].

The resonance of the second type appears only in nonreciprocal structures. It corresponds to interaction of SWs traveling along metallized and unmetallized surfaces under condition (6.21) (see regions of the SW spectra marked by circles). One can see the MBG opening in pointed regions. The values of the MBG diminished as the number n increases from $n = 1^+$ to $n = 3^+$. This feature is due to decreasing of the overlapping integral of dynamic magnetizations and fields of interacting quasi-surface SWs as their localization near opposite surfaces become stronger with an increase of the wavenumber.

One of the specific features of MBGs opening at resonances (6.21) is indirect character of gaps. It means, that points with $V_g = 0$ on dispersion curves are characterized by different wavenumbers and it also reflects the loss of symmetry of the SW spectra in nonreciprocal structure: $\omega(k) \neq \omega(-k)$. The indirect character is more evident for larger MBGs (correspondent to gaps with lower numbers n) [figure 6.8(a)]. Because the value of the MBG increases with increasing the value of magnetic contrast ΔM [7], one can expect that indirect character of MBG in high contrast MC covered by PEC will be more brightly.

Now high contrast MC will be considered. In figure 6.8(b) the calculated SW spectra for high contrast MC contacted with one PEC and with both dielectric surroundings is shown by solid and dashed lines, respectively. For high contrast MC

an approach based on the use of the spectra of the partial waves of the uniform film with averaged saturation magnetizations M_S is not so obvious, as it was in the case of low contrast crystal. The SW dispersion calculated for MC with dielectric surroundings is reciprocal and MBGs between the magnonic bands are present with minimum and maximum (points 1 and 2 in figure 6.8(b)) at the BZ border according with the condition (6.20). The MPG calculated for the same MC with PEC has nonreciprocal property with pronounced shift of the maximum (or minimum) of the first (or second) band from the BZ border (points 3 and 4 in figure 6.8(b)). For chosen parameters the minimal energy state of high energy branch and maximal energy state of low energy branch are characterized by wavenumbers $k_3 \approx -0.7\pi/a$ and $k_4 \approx -0.2\pi/a$ and MBG has the width $\Delta f \approx 1.1$ GHz. The interesting point is that the metallization of the MC increases the group velocity of higher bands, e.g., in proximity of the point 4 in figure 6.8(b). This is an effect of the induced hybridization between first and second band. This may imply advantages for applications in magnetic field sensors, which require a high field sensitivity and a sharp band gap absorption peak [24].

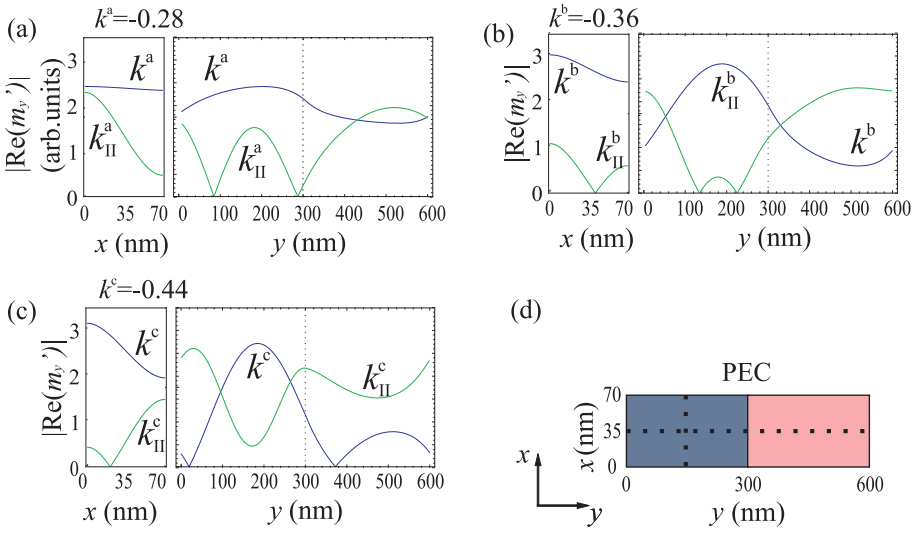

Figure 6.9: (a)-(c) The spatial distribution of the magnetization component $\left|\mathrm{Re}(m_y')\right|$ for three values of k^i wavenumber (in units of π/a) across the thickness of the MC (left plots) and along the y axis (right plots). The wavevectors are indicated by vertical dashed line on the fig 6.8(a). The path along which the distributions are plotted is indicated on the unite cell of MC by dotted lines in (d).

To receive insight in character of propagating SWs from different bands in the BZ lets consider the spatial distribution of the real part of the periodic Bloch function of the dynamic magnetization component $m_y'(x,y)$ ($\left|\mathrm{Re}(m_y')\right|$) for low magnetization contrast MC. In figures 6.9(a)-(c) the function $\left|\mathrm{Re}(m_y')\right|$ of two lowest modes across the MC thickness and along the periodicity are plotted for three wavenumbers k^a, k^b and k^c indicated in figure 6.8(a) by vertical dashed lines. The paths in MC along which the plots are made are marked by vertical dashed lines in figure 6.9(d).

For $k^{\mathrm{a}} = -0.28\pi/a$ the amplitude of SW is a quasi-uniform function of y for the mode I (figure 6.9(a)). The distortion from the uniform shape is due to different values of saturation magnetizations in materials 1 and 2. The distribution of the second mode has two nodal points along the y axis. This suggests that its effective wavenumber is larger than π/a and appear as a solution in the first BZ due to back-folding of the band. The effective wavenumber is $k_{\mathrm{II}}^{\mathrm{a}} = k^{\mathrm{a}} + 2\pi/a$. The dynamic component of the magnetization is neither uniform nor exponentially decaying across the thickness as could be expected for MSSW mode. This is ascribed to the role of exchange interactions, which have a minor influence on the dispersion relation but are sufficient to modify the profile of modes, as it was shown in references [34, 38] for thin films.

For $k^{\mathrm{b}} = -0.36\pi/a$ [figure 6.9(b)] the hybridization is very strong. The SW amplitude modulus shows the larger amplitude of the first mode in material with low saturation magnetization and of the second mode within material with higher saturation magnetization. For $k^{\mathrm{c}} = -0.44\pi/a$ [figure 6.9(c)] the distortion from quasi-uniform distribution of the second mode along y axis suggests, that hybridization between the first and second mode is still present and on the other hand the hybridization between second and third mode starts to play role. It is due to the non-symmetrical band structure when the density of MBGs within one BZ is increased. We might observe hybridizations between more than two SWs.

6.3 Magnonic Band Gaps in Metallized YIG Magnonic Crystals

This nonreciprocity remains even for large wavenumbers in a ferromagnetic film with a metal overlayer of finite conductivity σ separated by a distance t [32]. However, in this case the nonreciprocity will occur in a limited wavenumber range, as it was described in the subsection 6.1. The exchange interaction influences mainly the localization of SW amplitude, while the dispersion relation remains nonreciprocal and almost unchanged in the considered wavenumber range [146].

In an yttrium iron garnet (YIG) film (of thickness $d = 7.7$ μm) with a silver overlayer (of conductivity $\sigma = 6 \times 10^7$ S/m and thickness $D = 5$ μm) at a nonzero distance ($t = 18$ μm) from the YIG surface the SW dispersion is nonreciprocal only for wavenumbers below k_2, as shown in Fig. 6.10(b). The plot presents the SWs frequency f in the DE geometru versus the wavenumber in a YIG film without or with an Ag overlayer (solid and dashed line, respectively). As a quantitative measure of the nonreciprocity strength, a factor $\Delta_f(k) \equiv f_{\mathrm{metal}}(k) - f_{\mathrm{dielectric}}(k)$ is introduced, where $f_{\mathrm{metal}}(k)$ and $f_{\mathrm{dielectric}}(k)$ denote the dispersion relations of the YIG film surrounded by dielectrics on both sides and with a metallic overlayer, respectively. The wavenumber dependence of Δ_f in the YIG film is shown in Fig. 6.10(c). One can see that Δ_f increases from 0 at $k = 0$ to a maximal value of 0.35 GHz at $k = k_1$. Having reached the maximum, Δ_f decreases smoothly to 0 as

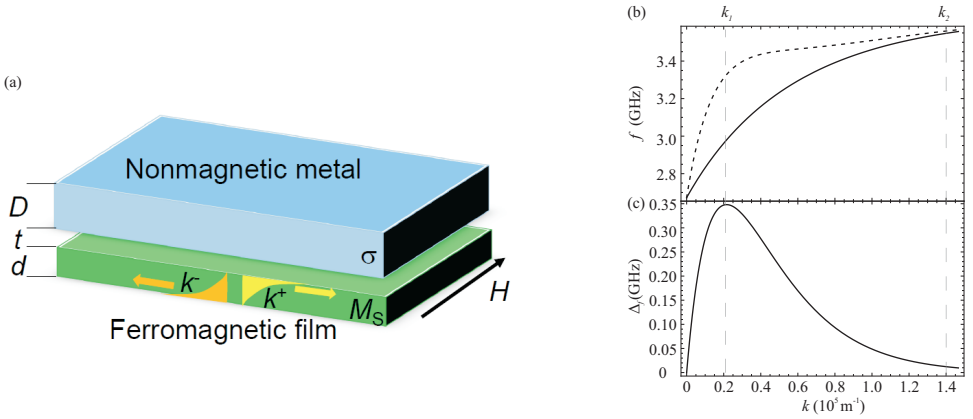

Figure 6.10: (a) Ferromagnetic film of thickness d saturated by external magnetic field H and covered with a nonmagnetic metallic film of conductivity σ and thickness D. The metal is separated from the ferromagnetic film by the distance $t = 18$ μm. (b) The dispersion relation of SWs propagating perpendicularly to H in a YIG thin film ($d = 7.7$ μm) surrounded by dielectrics on both sides (solid line) and with a thick Ag overlayer ($\sigma = 6\times10^7$ S/m and $D = 5$ μm) (dashed line). For wavenumbers $k > k_2$ the effect of the metallic overlayer is minor. (c) The nonreciprocity strength Δ_f as a function of the wavenumber for a YIG film with an Ag overlayer; k_1 indicates the wavevector for which Δ_f is maximal, i.e., the metallic overlayer has the maximal influence on the SW dispersion relation.

the wavenumber continues to grow.

Considering the limited range of wavenumbers for which Δ_f is significantly different from 0, and their small values, optimization of the structure seems unavoidable for the experimental observation of the nonreciprocity of the SW dispersion relation. In particular, it will be required in studies of SWs in nano-patterned magnetic structures to exploit the nonreciprocal properties for applications in integrated magnonic devices [167, 84, 22]. For application purposes the nonreciprocity strength should be studied along with the losses of SWs resulting from eddy currents induced in the metallic overlayer; however, such studies, discussed elsewhere [129], are beyond the scope of the present paper.

Here, theoretically and experimentally the influence of the nonreciprocal dispersion relation of SWs on the frequency of magnonic band gaps of a one-dimensional magnonic crystal is studied. Recent experimental studies of the influence of the nonreciprocity caused by a metal overlayer on SW Bragg resonances in a YIG film with a lattice of etched grooves [164, 153] have shown that if a dielectric spacer is inserted between the YIG film with a corrugated surface and the metal overlayer, magnonic band gaps occur, but only for SWs with large wavenumbers. This corresponds to $k > k_2$, a range in which the effect of the conductivity on the dispersion relation is negligible (see Fig. 6.10(b)). In papers [86, 8] it was shown theoretically that thin bi-component magnonic crystals with a PEC overlayer should have magnonic band gaps. Moreover, it was demonstrated [8] that the nonreciprocity caused by the PEC

shifts the minimums and maximums of the magnonic bands from the boundary of the Brillouin zone. This provides the mechanism of formation of the indirect magnonic band gaps found in calculations. However, the existence of magnonic band gaps in magnonic crystals with a nonreciprocal dispersion relation has not been verified experimentally to date. The present paper is the first to report their experimental observation in such structures.

Experiment

The experimental results has been obtained by Kotelnikov Institute of Radio Engineering and Electronics, Saratov branch, Russian Academy of Sciences. The studied magnonic crystal (Fig. 6.11(a)) was based on an epitaxial structure consisting of a 7.7 μm thick yttrium iron garnet (YIG) film grown on gadolinium gallium garnet (GGG). An array of 80 μm wide and 1.5 μm deep grooves with a lattice constant of 150 μm was introduced by chemical etching on the YIG surface. This magnonic crystal was placed on two prototype models of delay lines, coplanar (Fig. 6.11(b)) and microstripe waveguides (Fig. 6.11(c)), on input and output transducers with a width $w \approx 30$ μm and a length of 4 mm. The two transducers were separated by a distance $S = 4$ mm. The YIG film had a saturation magnetization of $M_S = 0.141 \times 10^6$ A/m, a ferromagnetic resonance width $\mu_0 \Delta H \approx 0.035$ mT, and planar dimensions 15 mm $\times$ 5 mm. The whole structure was placed in the gap of an electromagnet so that the external magnetic field was oriented along the grooves and parallel to the transducers. The field was strong enough to saturate the sample ($\mu_0 H = 41.6$ mT). The amplitude–frequency characteristics S21(f) of the delay line prototype models were measured by an Agilent E5071C-480 network analyzer.

The two different types of delay lines (microstripe and coplanar) were used to measure the transmission of SWs in the MC without and in contact with a metallic overlayer, thus without and with a nonreciprocal dispersion relation, respectively, for waves propagating in opposite directions. The transmission spectra measured with the coplanar and microstripe waveguides are shown in Fig. 6.11(d) and (e), respectively. Magnonic band gaps, indicated by low S21, are found in both transmission spectra. Moreover, the measured gaps lie in the frequency and wave-vector ranges in which strong nonreciprocity of the dispersion relation should already occur in the MC with the metallic overlayer (see Fig. 6.10(c)). Comparing the frequency position of the magnonic band gaps (indicated by colored bars), one can see that the gaps in a metalized MC are shifted to higher frequencies as compared to the respective magnonic band gaps found in microstripe measurements.

Magnonic band structure of metallized magnonic crystals

The numerical calculations were performed of the magnonic band structure of the one-dimensional magnonic crystal shown in Fig. 6.11(a), with and without metallic layer on top of the film. The wave equation for the electric field vector **E** obtained from the Maxwell equations need to be solved in order to calculate the SW dispersion

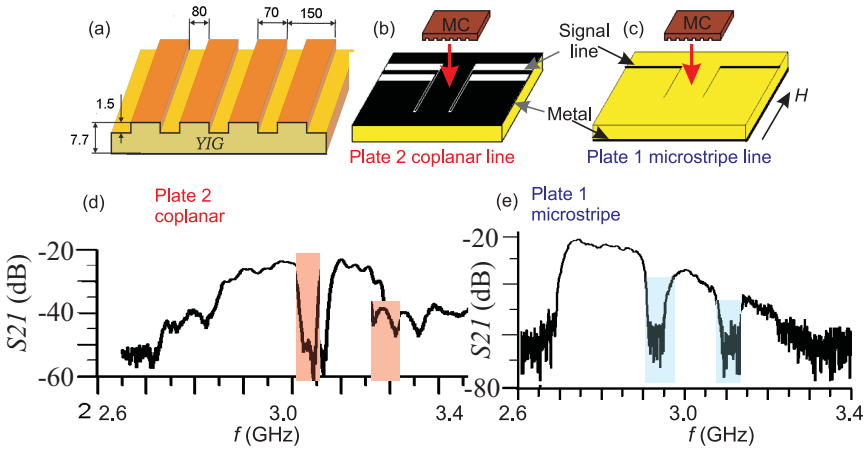

Figure 6.11: (a) The structure of the one-dimensional YIG-based MC with a periodically corrugated surface used in the experiments. The dimensions of the sample are specified in micrometers. (b), (c) Two configurations, with a coplanar line (plate 2) and a microstripe line (plate 1), used in the measurements of the SW transmission in the MC in and without contact with the metal, respectively. (d), (e) The transmission spectra (S21) versus the SW frequency f measured with the coplanar and microstripe lines. The colored bars indicate the magnonic band gaps.

relation:

$$\nabla \times (\hat{\mu}_r^{-1} \nabla \times \mathbf{E}) - (2\pi f)^2 \sqrt{\epsilon_0 \mu_0} \left(\epsilon_0 - \frac{i\sigma}{(2\pi f)\epsilon_0} \right) \mathbf{E} = 0, \tag{6.22}$$

where μ_0 and ϵ_0 denote the vacuum permeability and permittivity, respectively, and σ is the conductivity, different from zero only in the metallic overlayer. The permeability tensor $\hat{\mu}(\mathbf{r})$ is obtained from the linearized damping-free Landau-Lifshitz equation without exchange interaction [118]:

$$\hat{\mu}(\mathbf{r}) = \begin{pmatrix} \mu^{xx}(\mathbf{r}) & i\mu^{xy}(\mathbf{r}) & 0 \\ -i\mu^{yx}(\mathbf{r}) & \mu^{yy}(\mathbf{r}) & 0 \\ 0 & 0 & 1 \end{pmatrix}, \tag{6.23}$$

where

$$\mu^{xx}(\mathbf{r}) = \frac{\gamma\mu_0 H(\gamma\mu_0 H + \gamma\mu_0 M_S) - (2\pi f)^2}{(\gamma\mu_0 H)^2 - (2\pi f)^2}, \tag{6.24}$$

$$\mu^{xy}(\mathbf{r}) = \frac{\gamma\mu_0 M_S 2\pi f}{(\gamma\mu_0 H)^2 - (2\pi f)^2}, \tag{6.25}$$

$$\mu^{yx}(\mathbf{r}) = -\mu^{xy}(\mathbf{r}), \tag{6.26}$$

$$\mu^{yy}(\mathbf{r}) = \mu^{xx}(\mathbf{r}), \tag{6.27}$$

M_S is the saturation magnetization, and γ the gyromagnetic ratio. The equation (A.2), with the Bloch theorem applied, yields a linear eigenequation for the frequency

or a quadratic equation for the wavenumber [66]. The eigenequation is solved by the finite element method with the use of a commercial COMSOL software. The SW dispersion relations calculated from these equations are shown in Fig. 6.12(a) and (b).

A reciprocal band structure (with $f(k^+) = f(k^-)$) was obtained in the magnonic crystal without metallic overlayer (Fig. 6.12(b)) with magnonic band gaps open at the boundary (first gap) and center of the Brillouin zone. The first gap ranges from 2.925 GHz to 2.975 GHz, and the second one from 3.125 GHz to 3.15 GHz. When the MC is covered with an Ag film the slope of the dispersion relation branch for waves propagating in the positive direction is significantly increased, while the k^- branch remains almost unchanged. Thus, the k^+ and $k^- + G$ branches cross within the BZ at much higher frequencies than in the case of the reciprocal structure. The resulting magnonic band gap is an indirect gap and its opening requires the fulfillment of the Bragg condition [8]:

$$k^+ + k^- = nG,$$

where G is the shortest reciprocal lattice vector, $G = 2\pi/a = 0.419 \times 10^5$ m^{-1}, and $n = 1$ for the first gap. Ranging from 3.05 GHz to 3.09 GHz, this band gap is shifted to higher frequencies by ca. 0.75 GHz as compared with the MC without metallic overlayer. This shift is in agreement with the experimental results presented in Fig. 6.11(d). Considering that this change in the position of the magnonic band gap results from the change in the dispersion relation for k^+ waves, this shift can be also treated as a measure of nonreciprocity. In fact, it is close to the value of the nonreciprocity strength introduced in Fig. 6.10(c).

The results of the investigation of the influence of the metallic overlayer on the SW dispersion relation in ferromagnetic thin films were presented. By analyzing the electric field component within the finite-conductivity metallic layer the extent of the nonreciprocity was estimated in such structures versus various parameters, including the magnetic saturation of the ferromagnetic film, the conductivity of the metallic layer, its thickness and distance from the ferromagnetic film, and the in-plane external magnetic field. Using an approximate analytical formula for the SW frequency, a structure in which the effect of the metallization is significant in a wide wave-vector range was defined and should be measurable by standard experimental techniques suitable for the measurement of SWs.

It was shown that the results obtained by the FEM in the present study agree with the semi-analytical data. A major advantage of the FEM is its applicability, in the present formulation, to various structures, including magnonic crystals,[8] multilayered structures, ferromagnetic films with layers of various conductivity, films with corrugated surfaces or in contact with a metallic grid. These additional structural variations might further increase the nonreciprocal effect. The results presented can be of use for the development of devices exploiting the nonreciprocity of the SW dispersion relation. The proposed structure, based on a CoFeB thin film, can be further explored for magnonic applications[15] by periodic patterning of the

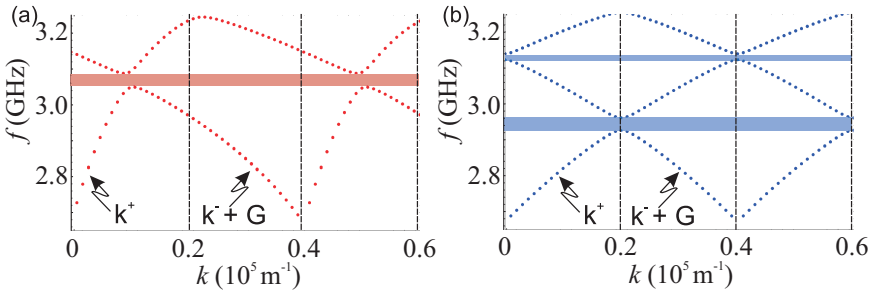

Figure 6.12: Magnonic band structure of the MC shown in Fig. 6.11(a), based on a YIG film with a corrugated surface (a) with and (b) without metallic overlayer. Color bars indicate magnonic band gaps. Vertical dashed lines represent Brillouin zone boundaries: π/a, $2\pi/a$ and $3\pi/a$. In (b) the metallic layer is assumed to be 10 μm above the YIG surface.

ferromagnetic film or patterning of the metallic cover layer.

The impact of a perfect metal overlayer on the spin wave dispersion relation of 1D bi-component magnonic crystals with high and low magnetic contrasts was investigated theoretically. In both cases one can found the nonreciprocal band structure where the Bragg resonances of the nonreciprocal spin waves take place under fulfillment of the so-called exchange Bragg condition and are characterizing by indirect magnonic band gap shifted from BZ border. Specific features of nonreciprocity in low contrast magnonic crystals lead to appearance of several magnonic band gaps located within the first BZ for waves propagating along metallized surface, while they are absent for waves traveling along unmetallized surface of MC. This property can lead to multimode hybridizations effects which are only possible because of the periodicity of the system and the folding of the dispersion branches to the first BZ.

In order to observe nonreciprocal magnonic band structure experimentally one need to consider the influence of finite conductivity and damping of SWs. Finite conductivity, overlayer thickness, skin depth and MC lattice constant must be properly adjusted to receive influence of metal layer mainly on dispersion but not on the losses of SWs [145]. These requirements demand the well designed structure of a MC to observe the indirect magnonic band gap formation in the first BZ with the Brillouin Light Scattering measurements [168] or with the broad-band ferromagnetic resonance [55]. When the finite conductivity is taken into account, the effect of metallization disappears for waves with large wavevectors. Thus, on one hand the lattice constant need to be chosen so the wavevector is big enough to measure it, but small enough that the effect of metallization is still present. However, the occurrence of magnonic band gaps was demonstrated experimentally in a one-dimensional YIG-based MC with a dispersion relation nonreciprocal due to the presence of a metallic overlayer at the corrugated surface of the YIG film, confirming the theoretical predictions. The presented results are of scientific and technological importance. They explain major questions arising from previous experimental results [153].

The presented result have importance for potential applications of MCs. The

results pointed out, that for high sensitive magnetic field sensors proposed recently [24], a shape of magnonic bands near the band gap edges will have important influence on its sensitivity. Its sensitivity might substantially depends on the direction of propagation and a design of the device. The additional studies, theoretical and experimental, are necessary to check if the structure proposed (1D bi-component MC but or an array of stripes, with the homogeneous metal plate on its top or bottom) can have better characteristics than a lattice of metallic stripes on the homogeneous ferromagnetic film [24]. The nonreciprocal properties of the magnonic band structure can be also useful to design miniaturized microwave isolators and circulators, essential elements in microwave technology. The fabrication of 1D MCs is relatively simple nowadays and can operate without an external magnetic field due to a shape anisotropy. The nonreciprocal property can be also combined with re-programmablity [40, 108, 81, 169].

Chapter 7

Summary

In this thesis the dispersion properties of the spin waves excitation were studied in the finite thickness ferromagnetic film and 1D magnonic crystals. The investigated samples were based on the YIG, Py and Co materials. The focus was put on the investigation of the properties that are crucial to the potential use for MC based devices, i.e., damping, interaction of standing spin waves with electromagnetic wave and nonreciprocity. The numerical calculations were performed in the frequency domain, solving the linearized Landau Lifshitz equation together with Maxwell equations. To approach the problem, the Plane Wave Method and the Finite Element Method were applied. Several models were presented throughout the thesis. In addition, some of the calculated data was compared with the experimental data obtained as part of scientific collaboration.

The numerical calculations prove to be in the agreement with the experimental observations and to have an important impact on the modern research in the field. The standing spin waves can interact strongly with the electromagnetic waves at GHz or sub-THz regime, leading to metamaterial posessing the negative refractive index. The nonreciprocity of the MCs is measurable, even that the metallization induces damping of the spin wave at wavelenght range of interest. A sensitive magnetic field sensor or parts of microwave signal transfer devices were outlined as potential applications.

Appendix A

Application of FEM to 1D Photonic Crystals

A simple case of application of FEM can be shown on the example of photonic crystal (PC). The dispersion relation of EM wave is solved for the 1D PC of infinite thickness, characterized by the unit cell of the length a. The unit cell is composed of equal length materials characterized by ϵ_1 and ϵ_2. The FEM procedure is described in the following subsections, listed in the part 3.2 of this thesis.

Defining a physical problem

In order to calculate the dispersion relation of light in 1D photonic ctystal, we solved the wave equation for an electric field vector ($\mathbf{e}$) obtained form the Maxwell equations:

$$\nabla \times (\hat{\mu}_r^{-1} \nabla \times \mathbf{e}) - (2\pi f)^2 \sqrt{\epsilon_0 \mu_0} \left(\epsilon_r - \frac{i\sigma}{(2\pi f)\epsilon_0} \right) \mathbf{e} = 0, \tag{A.1}$$

where μ_0 and ϵ_0 is a permeability and permittivity of vacuum, respectively, ϵ_r is relative permittivity. It will be assumed $\hat{\mu}_r$=1, $\sigma = 0$ and $\mathbf{e} = (0, 0, e_z)$. In 1D case $\frac{\partial}{\partial y}$=0 amd $\frac{\partial}{\partial z}$=0, giving:

$$\frac{\partial^2 e_z}{\partial x^2} + (2\pi f)^2 \sqrt{\epsilon_0 \mu_0} \epsilon_r e_z = 0. \tag{A.2}$$

Defining the governing equations in the weak formulation

This equation can be written in the weak form [73], i.e., multiplying by the arbitrary test vector and integrate over the domain. The domain here is a 1D photonic crystal

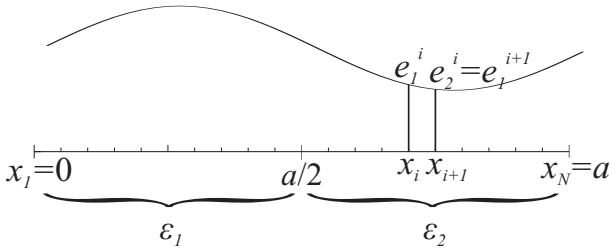

Figure A.1: Generating mesh of 1D photonic crystal.

of infinite length. According to 1.4 it is sufficient to look for the solution within the unit cell of length a:

$$\int_a^0 \frac{\partial^2 e_z}{\partial x^2} \cdot v dx + \int_a^0 (2\pi f)^2 \sqrt{\epsilon_0 \mu_0} \epsilon_r e_z \cdot v dx = 0. \tag{A.3}$$

Taking solution in the form of Bloch wave $e_z(x) = e(x)\mathrm{e}^{ik_x x}$

$$\int_a^0 \frac{\partial^2 e}{\partial x^2} \cdot v dx + 2ik_x \int_a^0 \frac{\partial e}{\partial x} \cdot v dx - k_x^2 \int_a^0 e \cdot v dx + \int_a^0 (2\pi f)^2 \sqrt{\epsilon_0 \mu_0} \epsilon_r e \cdot v dx = 0. \tag{A.4}$$

This equation can be transformed by integration by parts and using Green's identity to the following equation:

$$-\int_a^0 \frac{\partial e}{\partial x} \cdot \frac{\partial v}{\partial x} dx + 2ik_x \int_a^0 \frac{\partial e}{\partial x} \cdot v dx - k_x^2 \int_a^0 e \cdot v dx + \int_a^0 (2\pi f)^2 \sqrt{\epsilon_0 \mu_0} \epsilon_r e \cdot v dx = 0. \tag{A.5}$$

Discretization

In the next step of FEM procedure, the domain (a line of length a) is divided into sub intervals, see Fig. A.1. The set of points (nods) can define the sub intervals. The solution will be written on the base of some functions for each sub intervals separately, with the use of the value of e_z at nods. The system of nodes make a grid called a mesh.

Behavior of the function between nods can be presented by the polynomial functions. The choice of the functions complete the discretization of the problem. Here, the functions e can be defined locally, between nodal points in the form of first order polynomial function basis:

$$e^i(x) = a_1^i + a_2^i x. \tag{A.6}$$

That is in relation with function e describing whole unit cell by:

$$e = \sum_{i=1}^{N} e^i(x). \tag{A.7}$$

The functions can be also written in the form of $e^i(x_i) = e_1^i$ and $e^i(x_{i+1}) = e_2^i$

$$e^i(x) = e_1^i \frac{x_{i+1} - x}{x_{i+1} - x_i} + e_2^i \frac{x - x_i}{x_{i+1} - x_i}, \tag{A.8}$$

since:

$$e_1^i(x) = a_1^i + a_2^i x_i, \tag{A.9}$$

$$e_2^i(x) = a_1^i + a_2^i x_{i+1}, \tag{A.10}$$

$$a_1^i = \frac{e_1^i - e_2^i}{x_i - x_{i+1}}, \tag{A.11}$$

$$a_2^i = \frac{e_2^i x_i - e_1^i x_{i+1}}{x_i - x_{i+1}}. \tag{A.12}$$

The v^i is chosen to be composed of the linear functions:

$$v^i(x) = \begin{pmatrix} \frac{x_{i+1}-x}{x_{i+1}-x_i} \\ \frac{x-x_i}{x_{i+1}-x_i} \end{pmatrix}. \tag{A.13}$$

It is in relation with global test vector v by:

$$v = \sum_{j=1}^{N} v^j(x). \tag{A.14}$$

That can be written in terms of local coordinate ζ, that is 0 at x_i and 1 at x_{i+1}:

$$x = x_i + \zeta(x_{i+1} - x_i), \tag{A.15}$$

with following transforms:

$$dx = (x_{i+1} - x_i)d\zeta, \tag{A.16}$$

$$\frac{d}{dx} = \frac{1}{(x_{i+1} - x_i)} \frac{d}{d\zeta}. \tag{A.17}$$

Setting up the matrix

The above definitions allow to write Eq. A.5 in the form:

$$\sum_{i=1}^{N}\sum_{j=1}^{N}(-\int_{x_{i+1}}^{x_i}\frac{\partial e^i}{\partial x}\cdot\frac{\partial v^j}{\partial x}dx+2ik_x\int_{x_{i+1}}^{x_i}\frac{\partial e^i}{\partial x}\cdot v^j dx-k_x^2\int_{x_{i+1}}^{x_i}e^i\cdot v^j dx+ \int_{x_{i+1}}^{x_i}(2\pi f)^2\sqrt{\epsilon_0\mu_0}\epsilon_r e^i\cdot v^j dx)=0 \tag{A.18}$$

and with the use of A.15-A.17:

$$\sum_{i=1}^{N}\sum_{j=1}^{N}(\underbrace{-\frac{1}{(x_{i+1}-x_i)}\int_1^0\frac{\partial e^i}{\partial\zeta}\cdot\frac{\partial v^j}{\partial\zeta}d\zeta}_{\text{contributing to matrix } M_1}+\underbrace{2ik_x\int_1^0\frac{\partial e^i}{\partial\zeta}\cdot v^j d\zeta}_{\text{contributing to matrix } M_2}- \underbrace{k_x^2(x_{i+1}-x_i)\int_1^0 e^i\cdot v^j d\zeta}_{\text{contributing to matrix } M_3}+\underbrace{(2\pi f)^2(x_{i+1}-x_i)\int_1^0\sqrt{\epsilon_0\mu_0}\epsilon_r e^i\cdot v^j d\zeta}_{\text{contributing to matrix } M_4})=0. \tag{A.19}$$

The above equation might be written in form of the matrix operating on the vector, i.e., the first term is evaluated for $i,j=1$:

$$-\frac{1}{(x_{i+1}-x_i)}\left(\int_1^0\frac{\partial e_1^1(1-\zeta)}{\partial\zeta}d\zeta+\int_1^0\frac{\partial e_2^1\zeta}{\partial\zeta}d\zeta\right)\cdot\begin{pmatrix}\int_1^0\frac{\partial(1-\zeta)}{\partial\zeta}d\zeta\\ \int_1^0\frac{\partial\zeta}{\partial\zeta}d\zeta\end{pmatrix}= -\frac{1}{(x_{i+1}-x_i)}\begin{pmatrix}e_1^1 & -e_2^1\\ -e_1^1 & e_2^1\end{pmatrix}=\underbrace{-\frac{1}{(x_{i+1}-x_i)}\begin{pmatrix}1 & -1\\ -1 & 1\end{pmatrix}}_{\text{contributing to matrix } M_1}\begin{pmatrix}e_1^1\\ e_2^1\end{pmatrix}. \tag{A.20}$$

Defining the boundary conditions

Taking summation from 1 to N, PBC and the fact that $e_2^i=e_1^{i+1}$, the contribution from considered first term of A.19 might be written in the form of matrix multiplication.

$$M_1\mathbf{e} = -\frac{1}{(x_{i+1}-x_i)}\begin{pmatrix} 2 & -1 & 0 & \dots & \dots & \dots & -1 \\ -1 & 2 & -1 & \ddots & & & \vdots \\ 0 & -1 & 2 & \ddots & \ddots & & \vdots \\ \vdots & \ddots & \ddots & \ddots & \ddots & \ddots & \vdots \\ \vdots & & \ddots & \ddots & 2 & -1 & 0 \\ \vdots & & & \ddots & -1 & 2 & -1 \\ -1 & \dots & \dots & \dots & 0 & -1 & 2 \end{pmatrix}\begin{pmatrix} e_2^1 \\ e_2^2 \\ \vdots \\ \vdots \\ \vdots \\ e_2^N \end{pmatrix}. \tag{A.21}$$

The other contribution are calculated in the similar manner:

$$M_2 = \begin{pmatrix} 0 & \frac{1}{2} & 0 & \dots & \dots & \dots & -\frac{1}{2} \\ -\frac{1}{2} & 0 & \frac{1}{2} & \ddots & & & \vdots \\ 0 & -\frac{1}{2} & 0 & \ddots & \ddots & & \vdots \\ \vdots & \ddots & \ddots & \ddots & \ddots & \ddots & \vdots \\ \vdots & & \ddots & \ddots & 0 & \frac{1}{2} & 0 \\ \vdots & & & \ddots & -\frac{1}{2} & 0 & \frac{1}{2} \\ \frac{1}{2} & \dots & \dots & \dots & 0 & -\frac{1}{2} & 0 \end{pmatrix}, \tag{A.22}$$

$$M_3 = (x_{i+1}-x_i)\begin{pmatrix} \frac{2}{3} & \frac{1}{6} & 0 & \dots & \dots & \dots & \frac{1}{6} \\ \frac{1}{6} & \frac{2}{3} & \frac{1}{6} & \ddots & & & \vdots \\ 0 & \frac{1}{6} & \frac{2}{3} & \ddots & \ddots & & \vdots \\ \vdots & \ddots & \ddots & \ddots & \ddots & \ddots & \vdots \\ \vdots & & \ddots & \ddots & \frac{2}{3} & \frac{1}{6} & 0 \\ \vdots & & & \ddots & \frac{1}{6} & \frac{2}{3} & \frac{1}{6} \\ \frac{1}{6} & \dots & \dots & \dots & 0 & \frac{1}{6} & \frac{2}{3} \end{pmatrix}. \tag{A.23}$$

The matrix M_4 posses parameter ϵ_r that is defined in terms of ϵ_1 and ϵ_2. For $i < \frac{N}{2}$, $\epsilon_r = \epsilon_1$. For $i \geq \frac{N}{2}$, $\epsilon_r = \epsilon_2$ Thus:

$$M_4 = (x_{i+1}-x_i)\begin{pmatrix} \frac{2\epsilon_1}{3} & \frac{\epsilon_1}{6} & 0 & \dots & \dots & \dots & \frac{\epsilon_2}{6} \\ \frac{\epsilon_1}{6} & \frac{2\epsilon_1}{3} & -1 & \ddots & & & \vdots \\ 0 & \frac{\epsilon_1}{6} & \frac{2\epsilon_1}{3} & \ddots & \ddots & & \vdots \\ \vdots & \ddots & \ddots & \ddots & \ddots & \ddots & \vdots \\ \vdots & & \ddots & \ddots & \frac{2\epsilon_1}{3} & \frac{\epsilon_2}{6} & 0 \\ \vdots & & & \ddots & \frac{\epsilon_2}{6} & \frac{2\epsilon_1}{3} & \frac{\epsilon_2}{6} \\ \frac{\epsilon_1}{6} & \dots & \dots & \dots & 0 & \frac{\epsilon_2}{6} & \frac{2\epsilon_1}{3} \end{pmatrix}. \tag{A.24}$$

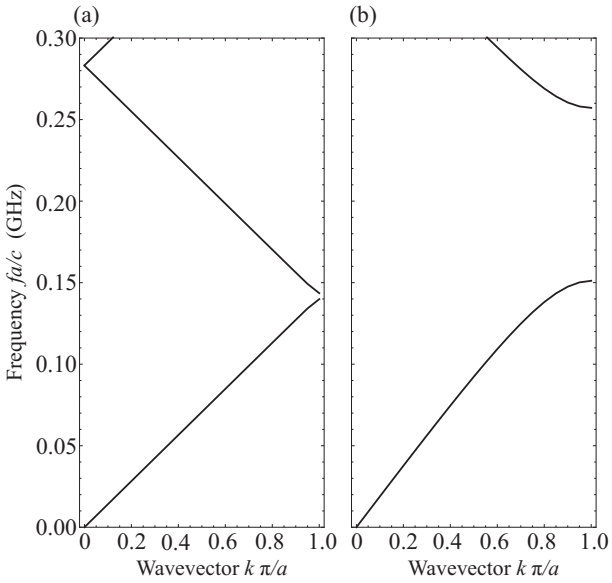

Figure A.2: The dispersion relation for (a) ϵ_1=12, ϵ_2=13 and (b) ϵ_1=1, ϵ_2=13.

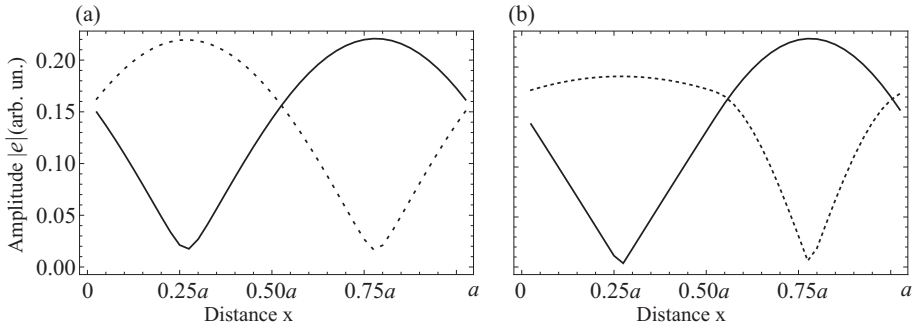

Figure A.3: The absolute value of the amplitude for (a) ϵ_1=12, ϵ_2=13 and (b) ϵ_1=1, ϵ_2=13. Continuous lines indicate the lowest frequency mode at $k = \frac{\pi}{a}$, dashed lines indicate second mode at $k = \frac{\pi}{a}$.

Thus we can write

$$M_1\mathbf{e} + M_2\mathbf{e} - M_3\mathbf{e} = -(2\pi f)^2 M_4\mathbf{e}. \tag{A.25}$$

Solving the matrix

The eigenequation is formed by multiplying the above equation by inverse of M^4:

$$M_4^{-1}M_1\mathbf{e} + M_4^{-1}M_2\mathbf{e} - M_4^{-1}M_3\mathbf{e} = -(2\pi f)^2\mathbf{e}. \tag{A.26}$$

This eigenequation might be solved with the use of numerical methods for larger systems. The results of the calculation of eigenvalues (ω) and eigenvectors (e) are

showed on the Figs. A.2 and A.3 respectively. The results are in accordance with [60]. The algorithm might be extended further, e.g., the quadratic eigenequation might be written for k wavevector and solved after linearization. This might be advantageous for systems where μ_r or ϵ_r are frequency dependent. In similar manner the method might be implied for 2D or 3D geometries (where neighboring elements are related in the matrix), or systems of equations with many variables (where size of egienvector increase).

Bibliography

[1] D. J. Norris, "Photonic crystals: A view of the future," *Nature Materials*, vol. 6, no. 3, p. 177, 2007.

[2] V. M. Passaro, *Advances in Photonic Crystals*. InTech, 2013.

[3] M. P. Kostylev, A. A. Serga, T. Schneider, B. Leven, and B. Hillebrands, "Spin-wave logical gates," *Applied Physics Letters*, vol. 87, no. 15, p. 153501, 2005.

[4] T. Schneider, A. A. Serga, B. Leven, B. Hillebrands, R. L. Stamps, and M. P. Kostylev, "Realization of spin-wave logic gates," *Applied Physics Letters*, vol. 92, no. 2, p. 022505, 2008.

[5] B. A. Kalinikos and A. N. Slavin, "Theory of dipole-exchange spin wave spectrum for ferromagnetic films with mixed exchange boundary conditions," *Journal of Physics C: Solid State Physics*, vol. 19, no. 35, p. 7013, 1986.

[6] H. Puszkarski and M. Krawczyk, "Magnonic crystals – the magnetic counterpart of photonic crystals," *Solid State Phenomena*, vol. 94, p. 125, 2003.

[7] M. Krawczyk and H. Puszkarski, "Plane-wave theory of three-dimensional magnonic crystals," *Physical Review B*, vol. 77, no. 5, p. 054437, 2008.

[8] M. Mruczkiewicz, M. Krawczyk, G. Gubbiotti, S. Tacchi, Y. A. Filimonov, D. V. Kalyabin, I. V. Lisenkov, and S. A. Nikitov, "Nonreciprocity of spin waves in metallized magnonic crystal," *New Journal of Physics*, vol. 15, p. 113023, 2013.

[9] Y. Gulyaev, S. Nikitov, L. Zhivotovskii, A. Klimov, P. Tailhades, L. Presmanes, C. Bonningue, C. Tsai, S. Vysotskii, and Y. Filimonov, "Ferromagnetic films with magnon bandgap periodic structures: Magnon crystals," *JETP Letters*, vol. 77, no. 10, p. 567, 2003.

[10] S. L. Vysotski, S. A. Nikitov, and Y. A. Filimonov, "Magnetostatic spin waves in two-dimensional periodic structures (magnetophoton crystals)," *Journal of Experimental and Theoretical Physics*, vol. 101, p. 547, 2005.

[11] Z. K. Wang, V. L. Zhang, H. S. Lim, S. C. Ng, M. H. Kuok, S. Jain, and A. O. Adeyeye, "Observation of frequency band gaps in a one-dimensional nanostructured magnonic crystal," *Applied Physics Letters*, vol. 94, no. 8, p. 083112, 2009.

[12] A. B. Ustinov, B. A. Kalinikos, V. E. Demidov, and S. O. Demokritov, "Formation of gap solitons in ferromagnetic films with a periodic metal grating," *Physical Review B*, vol. 81, no. 18, p. 180406, 2010.

[13] G. Gubbiotti, S. Tacchi, M. Madami, G. Carlotti, S. Jain, A. O. Adeyeye, and M. P. Kostylev, "Collective spin waves in a bicomponent two-dimensional magnonic crystal," *Applied Physics Letters*, vol. 100, no. 16, p. 162407, 2012.

[14] R. Gieniusz, V. D. Bessonov, U. Guzowska, A. I. Stognii, and A. Maziewski, "An antidot array as an edge for total non-reflection of spin waves in yttrium iron garnet films," *Applied Physics Letters*, vol. 104, no. 8, p. 082412, 2014.

[15] V. V. Kruglyak, S. O. Demokritov, and D. Grundler, "Magnonics," *Journal of Physics D: Applied Physics*, vol. 43, no. 26, p. 264001, 2010.

[16] A. A. Serga, A. V. Chumak, and B. Hillebrands, "YIG magnonics," *Journal of Physics D: Applied Physics*, vol. 43, no. 26, p. 264002, 2010.

[17] A. Khitun, M. Bao, and K. L. Wang, "Magnonic logic circuits," *Journal of Physics D: Applied Physics*, vol. 43, no. 26, p. 264005, 2010.

[18] S. O. Demokritov and A. N. Slavin, eds., *Magnonics from fundamentals to applications*. Springer, 2013.

[19] P. Hartemann, "Magnetostatic wave planar YIG devices," *IEEE Transactions on Magnetics*, vol. 20, no. 5, p. 1272, 1984.

[20] J. Ding, M. Kostylev, and A. O. Adeyeye, "Realization of a mesoscopic reprogrammable magnetic logic based on a nanoscale reconfigurable magnonic crystal," *Applied Physics Letters*, vol. 100, no. 7, p. 073114, 2012.

[21] J. Topp, D. Heitmann, M. P. Kostylev, and D. Grundler, "Making a reconfigurable artificial crystal by ordering bistable magnetic nanowires," *Physical Review Letters*, vol. 104, no. 20, p. 207205, 2010.

[22] M. Krawczyk and D. Grundler, "Review and prospects of magnonic crystals and devices with reprogrammable band structure," *Journal of Physics: Condensed Matter*, vol. 26, no. 12, p. 123202, 2014.

[23] P. Gay-Balmaz and O. J. Martin, "Electromagnetic resonances in individual and coupled split-ring resonators," *Journal of Applied Physics*, vol. 92, no. 5, p. 2929, 2002.

[24] M. Inoue, A. Baryshev, H. Takagi, P. B. Lim, K. Hatafuku, J. Noda, and K. Togo, "Investigating the use of magnonic crystals as extremely sensitive magnetic field sensors at room temperature," *Applied Physics Letters*, vol. 98, no. 13, p. 132511, 2011.

[25] F. Bloch, "Zur theorie des ferromagnetismus," *Zeitschrift für Physik*, vol. 61, no. 3-4, p. 206, 1930.

[26] D. D. Stancil and A. Prabhakar, *Spin waves. Theory and applications.* Springer, 2009.

[27] L. D. Landau and E. M. Lifshits, "On the theory of the dispersion of magnetic permeability in ferromagnetic bodies," *Physikalische Zeitschrift der Sowjetunion*, vol. 8, p. 153, 1935.

[28] T. Gilbert, "A phenomenological theory of damping in ferromagnetic materials," *IEEE Transactions on Magnetics*, vol. 40, no. 6, p. 3443, 2004.

[29] R. W. Damon and J. Eshbach, "Magnetostatic modes of a ferromagnet slab," *Journal of Physics and Chemistry of Solids*, vol. 19, no. 3, p. 308, 1961.

[30] S. R. Seshadri, "Surface magnetostatic modes of a ferrite slab," *Proceedings of the IEEE*, vol. 58, p. 506, 1970.

[31] M. U. K. Kawasaki, H. Takagi, "Surface magnetostatic modes of a ferrite slab," *IEEE Transactions on Microwave Theory and Techniques*, vol. 22, p. 924, 1974.

[32] T. Wolfram and R. E. D. Wames, "Magnetoexchange branches and spin-wave resonance in conducting and insulating films: Perpendicular resonance," *Physical Review B*, vol. 8, p. 3125, 1971.

[33] M. Sparks, "Effect of exchange on magnetostatic modes," *Physical Review Letters*, vol. 24, p. 1178, 1970.

[34] R. E. D. Wames and T. Wolfram, "Dipole-exchange spin waves in ferromagnetic films," *Journal of Applied Physics*, vol. 41, p. 987, 1970.

[35] E. G. Lokk, "Effect of a magnetic wall and a conducting plane on the characteristics of magnetostatic waves in an in-plane-magnetized ferrite plate," *Journal of Communications Technology and Electronics*, vol. 52, p. 189, 2007.

[36] N. S. Almeida and D. L. Mills, "Eddy currents and spin excitations in conducting ferromagnetic films," *Physical Review B*, vol. 53, p. 12232, 1996.

[37] L. R. Walker, "Resonant modes of ferromagnetic spheroids," *Journal of Applied Physics*, vol. 29, no. 3, 1958.

[38] M. Kostylev, "Non-reciprocity of dipole-exchange spin waves in thin ferromagnetic films," *Journal of Applied Physics*, vol. 113, no. 5, p. 053907, 2013.

[39] S. Nikitov, P. Tailhades, and C. Tsai, "Spin waves in periodic magnetic structures-magnonic crystals," *Journal of Magnetism and Magnetic Materials*, vol. 236, no. 3, p. 320, 2001.

[40] J. Topp, D. Heitmann, M. P. Kostylev, and D. Grundler, "Making a reconfigurable artificial crystal by ordering bistable magnetic nanowires," *Physical Review Letters*, vol. 104, no. 20, p. 207205, 2010.

[41] R. Huber, M. Krawczyk, T. Schwarze, H. Yu, G. Duerr, S. Albert, and D. Grundler, "Reciprocal Damon-Eshbach-type spin wave excitation in a magnonic crystal due to tunable magnetic symmetry," *Applied Physics Letters*, vol. 102, no. 1, p. 012403, 2013.

[42] A. Khitun, M. Bao, Y. Wu, J.-Y. Kim, A. Hong, A. Jacob, K. Galatsis, and K. L. Wang, "Spin wave logic circuit on silicon platform," *IEEE Computer Society*, p. 1107, 2008.

[43] A. Khitun, M. Bao, J. Lee, K. Wang, D. Lee, S. Wang, and I. Roshchin, "Inductively coupled circuits with spin wave bus for information processing," *Journal of Nanoelectronics and Optoelectronics*, vol. 3, no. 1, p. 24, 2008.

[44] Y. Fetisov and C. E. Patton, "Microwave bistability in a magnetostatic wave interferometer with external feedback," *IEEE Transactions on Magnetics*, vol. 35, no. 2, p. 1024, 1999.

[45] S. V. Vasiliev, V. V. Kruglyak, M. L. Sokolovskii, and A. N. Kuchko, "Spin wave interferometer employing a local nonuniformity of the effective magnetic field," *Journal of Applied Physics*, vol. 101, no. 11, p. 113919, 2007.

[46] A. B. Ustinov, A. V. Drozdovskii, and B. A. Kalinikos, "Multifunctional nonlinear magnonic devices for microwave signal processing," *Applied Physics Letters*, vol. 96, no. 14, p. 142513, 2010.

[47] Y. Liu and X. Zhang, "Metamaterials: a new frontier of science and technology," *Chemical Society Reviews*, vol. 40, p. 2494, 2011.

[48] R. V. Mikhaylovskiy, E. Hendry, and V. V. Kruglyak, "Negative permeability due to exchange spin-wave resonances in thin magnetic films with surface pinning," *Physical Review B*, vol. 82, no. 19, p. 195446, 2010.

[49] M. Mruczkiewicz, M. Krawczyk, R. V. Mikhaylovskiy, and V. V. Kruglyak, "Towards high-frequency negative permeability using magnonic crystals in metamaterial design," *Physical Review B*, vol. 86, p. 024425, Jul 2012.

[50] V. G. Veselago, "The electrodynamics of substances with simultaneously negative values of ϵ and μ," *Soviet Physics Uspekhi*, vol. 10, p. 509, 1968.

[51] J. B. Pendry, D. Schurig, and D. R. Smith, "Controlling electromagnetic fields," *Science*, vol. 312, no. 5781, p. 1780, 2006.

[52] R. W. Ziolkowski, "Propagation in and scattering from a matched metamaterial having a zero index of refraction," *Physical Review E*, vol. 70, no. 4, p. 046608, 2004.

[53] C. K. Lo, *Ferromagnetic Resonance - Theory and Applications.*

[54] B. Razavi and R. Behzad, *RF microelectronics*, vol. 1. Prentice Hall New Jersey, 1998.

[55] S. Vysotskii, S. Nikitov, E. Pavlov, and Y. Filimonov, "Bragg resonances of magnetostatic surface waves in a ferrite-magnonic-crystal-dielectric-metal structure," *Journal of Communications Technology and Electronics*, vol. 58, no. 4, p. 347, 2013.

[56] R. Sarbacher and W. Edson, *Hyper and Ultrahigh Frequency Engineering.* J. Wiley & Sons, Incorporated, 1943.

[57] K. Kurokawa, "Power waves and the scattering matrix," *IEEE Transactions on Microwave Theory and Techniques*, vol. 13, p. 194, Mar 1965.

[58] A. S. S. O. Demokritov, B. Hillebrands, "Brillouin light scattering studies of confined spin waves: linear and nonlinear confinement," *Physics Reports*, vol. 348, p. 441, 2001.

[59] R. Gieniusz, T. Blachowicz, A. Maziewski, A. Petroutchik, L. T. Baczewski, A. Wawro, J. Hamrle, O. Serga, and B. Hillebrands, "Brillouin light scattering investigations of magnetic and elastic properties in mbe grown trilayer mo/co/au systems," *Acta Physica Polonica A*, vol. 115, p. 213, 2009.

[60] J. D. Joannopoulos, S. G. Johnson, J. N. Winn, and R. D. Meade, *Photonic Crystals: Molding the Flow of Light.* Princeton Univ. Press., 2 ed., 2008.

[61] D. Prather, *Photonic Crystals, Theory, Applications and Fabrication.* Wiley Series in Pure and Applied Optics, Wiley, 2009.

[62] V. Laude, M. Wilm, S. Benchabane, and A. Khelif, "Full band gap for surface acoustic waves in a piezoelectric phononic crystal," *Physical Review E*, vol. 71, no. 3, p. 036607, 2005.

[63] J. O. Vasseur, P. A. Deymier, B. Djafari-Rouhani, Y. Pennec, and A.-C. Hladky-Hennion, "Absolute forbidden bands and waveguiding in two-dimensional phononic crystal plates," *Physical Review B*, vol. 77, p. 085415, 2008.

[64] M. Sokolovsky and M. Krawczyk, "The magnetostatic modes in planar one-dimensional magnonic crystals with nanoscale sizes," *Journal of Nanoparticle Research*, vol. 13, p. 6085, 2011.

[65] J. W. Kos, M. Krawczyk, and M. Sokolovskyy, "Bulk and edge modes in two-dimensional magnonic crystal slab," *Journal of Applied Physics*, vol. 109, no. 7, 2011.

[66] M. Mruczkiewicz, M. Krawczyk, V. K. Sakharov, Y. V. Khivintsev, Y. A. Filimonov, and S. A. Nikitov, "Standing spin waves in magnonic crystals," *Journal of Applied Physics*, vol. 113, no. 9, p. 093908, 2013.

[67] A. I. Akhiezer, V. G. Bar'yakhtar, and S. V. Peletminskii, *Spin waves*. North Holland, Amsterdam, 1968.

[68] S. Chikazumi and C. Graham, *Physics of Ferromagnetism*. International Series of Monographs on Physics, Clarendon Press, 1997.

[69] J. O. Vasseur, L. Dobrzynski, B. Djafari-Rouhani, and H. Puszkarski, "Magnon band structure of periodic composites," *Physical Review B*, vol. 54, no. 2, p. 1043, 1996.

[70] V. Kruglyak, A. Kuchko, and V. Finokhin, "Spin-wave spectrum of an ideal multilayer magnet upon modulation of all parameters of the Landau-Lifshitz equation," *Physics of the Solid State*, vol. 46, no. 5, p. 867, 2004.

[71] J. Kaczer and L. Murtinova, "On the demagnetizing energy of periodic magnetic distributions," *Physica status solidi (a)*, vol. 23, no. 1, p. 79, 1974.

[72] M. Krawczyk, M. Sokolovskyy, J. Klos, and S. Mamica, "On the formulation of the exchange field in the landau-lifshitz equation for spin-wave calculation in magnonic crystals," *Advances in Condensed Matter Physics*, vol. 2012, 2012.

[73] M. Schäfer, *Computational Engineering - Introduction to Numerical Methods*. Springer, 2006.

[74] J. Castera and P. Hartemann, "A multipole magnetostatic volume wave resonator filter," *IEEE Transactions on Magnetics*, vol. 18, no. 6, p. 1601, 1982.

[75] R. Carter, C. Smith, and J. Owens, "Magnetostatic forward volume wave - spin wave conversion by etched gratings in LPE-YIG," *IEEE Transactions on Magnetics*, vol. 16, no. 5, p. 1159, 1980.

[76] A. Maeda and M. Susaki, "Nano-order depth control in magnetic grating," *Physica status solidi (c)*, vol. 4, no. 12, p. 4396, 2007.

[77] A. V. Chumak, A. A. Serga, S. Wolff, B. Hillebrands, and M. P. Kostylev, "Scattering of surface and volume spin waves in a magnonic crystal," *Applied Physics Letters*, vol. 94, no. 17, p. 172511, 2009.

[78] G. Gubbiotti, S. Tacchi, M. Madami, G. Carlotti, A. O. Adeyeye, and M. Kostylev, "Brillouin light scattering studies of planar metallic magnonic crystals," *Journal of Physics D: Applied Physics*, vol. 43, no. 26, p. 264003, 2010.

[79] V. L. Zhang, F. S. Ma, H. H. Pan, C. S. Lin, H. S. Lim, S. C. Ng, M. H. Kuok, S. Jain, and A. O. Adeyeye, "Observation of dual magnonic and phononic bandgaps in bi-component nanostructured crystals," *Applied Physics Letters*, vol. 100, no. 16, p. 163118, 2012.

[80] R. L. Carter, J. M. Owens, C. V. Smith, and K. W. Reed, "Ionimplanted magnetostatic wave reflective array filters," *Journal of Applied Physics*, vol. 53, no. 3, 1982.

[81] J. Ding, M. Kostylev, and A. O. Adeyeye, "Magnetic hysteresis of dynamic response of one-dimensional magnonic crystals consisting of homogenous and alternating width nanowires observed with broadband ferromagnetic resonance," *Physical Review B*, vol. 84, p. 054425, Aug 2011.

[82] S. Vysotsky, S. Nikitov, N. Novitskii, A. Stognii, and Y. Filimonov, "Spectrum and losses of surface magnetostatic waves in a 1D magnon crystal," *Technical Physics*, vol. 56, no. 2, p. 308, 2011.

[83] S. Vysotskii, S. Nikitov, E. Pavlov, and Y. Filimonov, "The spectrum of the spin-wave excitations of the tangentially magnetized 2d hexagonal ferrite magnonic crystal," *Journal of Communications Technology and Electronics*, vol. 55, no. 7, p. 800, 2010.

[84] S. O. Demokritov and A. N. Slavin, *Magnonics: From Fundamentals to Applications*, vol. 125. Springer, 2012.

[85] Z. K. Wang, V. L. Zhang, H. S. Lim, S. C. Ng, M. H. Kuok, S. Jain, and A. O. Adeyeye, "Nanostructured magnonic crystals with size-tunable bandgaps," *ACS nano*, vol. 4, no. 2, p. 643, 2010.

[86] M. L. Sokolovskyy, J. W. Klos, S. Mamica, and M. Krawczyk, "Calculation of the spin-wave spectra in planar magnonic crystals with metallic overlayers," *Journal of Applied Physics*, vol. 111, no. 7, p. 07C515, 2012.

[87] M. Bertolotti, "Waves in metamaterials, by l. solymar and e. shamonina," *Contemporary Physics*, vol. 51, no. 6, p. 545, 2010.

[88] B. Edwards, A. Alù, M. E. Young, M. Silveirinha, and N. Engheta, "Experimental verification of epsilon-near-zero metamaterial coupling and energy squeezing using a microwave waveguide," *Physical Review Letters*, vol. 100, p. 033903, 2008.

[89] P. E. Tannenwald and M. H. Seavey, "Ferromagnetic resonance in thin films of permalloy," *Physical Review*, vol. 105, p. 377, 1957.

[90] D. D. Stancil, "Phenomenological propagation loss theory for the magnetostatic waves in thin ferrite films," *Journal of Applied Physics*, vol. 59, p. 218, 1986.

[91] V. Kruglyak and A. Kuchko, "Effect of the intralayer inhomogenity in the distribution of the parameter of spin waves in multilayers," *The Physics of Metals and Metallography*, vol. 93, p. 511, 2002.

[92] M. P. Kostylev and A. A. Stashkevich, "Stochastic properties and Brillouin light scattering response of thermally driven collective magnonic modes on the arrays of dipole coupled nanostripes," *Physical Review B*, vol. 81, no. 5, p. 054418, 2010.

[93] Y. Liu and X. Zhang, "Metamaterials: a new frontier of science and technology," *Chemical Society Reviews*, vol. 40, no. 5, p. 2494, 2011.

[94] R. A. Shelby, D. R. Smith, and S. Schultz, "Experimental verification of a negative index of refraction," *Science*, vol. 292, no. 5514, p. 77, 2001.

[95] A. Grigorenko, "Negative refractive index in artificial metamaterials," *Optics letters*, vol. 31, no. 16, p. 2483, 2006.

[96] W. J. Padilla, D. R. Smith, and D. N. Basov, "Spectroscopy of metamaterials from infrared to optical frequencies," *The Journal of the Optical Society of America B*, vol. 23, no. 3, p. 404, 2006.

[97] N. Engheta and R. W. Ziolkowski, *Metamaterials: physics and engineering explorations*. John Wiley and Sons - IEEE Press, 2006.

[98] J. B. Pendry, "Negative refraction makes a perfect lens," *Physical Review Letters*, vol. 85, no. 18, p. 3966, 2000.

[99] H. Zhao, J. Zhou, Q. Zhao, B. Li, L. Kang, and Y. Bai, "Magnetotunable left-handed material consisting of yttrium iron garnet slab and metallic wires," *Applied Physics Letters*, vol. 91, no. 13, p. 131107, 2007.

[100] H.-T. Chen, J. F. O'Hara, A. K. Azad, A. J. Taylor, R. D. Averitt, D. B. Shrekenhamer, and W. J. Padilla, "Experimental demonstration of frequency-agile terahertz metamaterials," *Nature Photonics*, vol. 2, no. 5, p. 295, 2008.

[101] A. Alù and N. Engheta, "Pairing an epsilon-negative slab with a mu-negative slab: resonance, tunneling and transparency," *IEEE Transactions on Antennas and Propagation*, vol. 51, no. 10, p. 2558, 2003.

[102] J. Pendry, A. J. Holden, D. J. Robbins, and W. J. Stewart, "Magnetism from conductors and enhanced nonlinear phenomena," *IEEE Transactions on Microwave Theory and Techniques*, vol. 47, no. 11, p. 2075, 1999.

[103] O. Acher, "Copper vs. iron: Microwave magnetism in the metamaterial age," *Journal of Magnetism and Magnetic Materials*, vol. 321, no. 14, p. 2093, 2009.

[104] A. Pimenov, A. Loidl, K. Gehrke, V. Moshnyaga, and K. Samwer, "Negative refraction observed in a metallic ferromagnet in the gigahertz frequency range," *Physical Review Letters*, vol. 98, p. 197401, 2007.

[105] J. Carbonell, H. García-Miquel, and J. Sánchez-Dehesa, "Double negative metamaterials based on ferromagnetic microwires," *Physical Review B*, vol. 81, p. 024401, Jan 2010.

[106] V. Boucher and D. Ménard, "Effective magnetic properties of arrays of interacting ferromagnetic wires exhibiting gyromagnetic anisotropy and retardation effects," *Physical Review B*, vol. 81, p. 174404, 2010.

[107] M. Pardavi-Horvath, G. Makeeva, and O. Golovanov, "Spin-wave resonances affected by skin-effect in conducting magnetic nanowire arrays at terahertz frequencies," *IEEE Transactions on Magnetics*, vol. 47, no. 2, p. 313, 2011.

[108] S. Tacchi, M. Madami, G. Gubbiotti, G. Carlotti, S. Goolaup, A. O. Adeyeye, N. Singh, and M. P. Kostylev, "Analysis of collective spin-wave modes at different points within the hysteresis loop of a one-dimensional magnonic crystal comprising alternative-width nanostripes," *Physical Review B*, vol. 82, no. 18, p. 184408, 2010.

[109] G. Duerr, R. Huber, and D. Grundler, "Enhanced functionality in magnonics by domain walls and inhomogeneous spin configurations," *Journal of Physics: Condensed Matter*, vol. 24, p. 024218, 2012.

[110] J. T. Shen and P. M. Platzman, "Near field imaging with negative dielectric constant lenses," *Applied Physics Letters*, vol. 80, no. 18, 2002.

[111] D. R. Smith, D. Schurig, M. Rosenbluth, S. Schultz, S. A. Ramakrishna, and J. B. Pendry, "Limitations on subdiffraction imaging with a negative refractive index slab," *Applied Physics Letters*, vol. 82, no. 10, 2003.

[112] S. Kocaman, M. Aras, P. Hsieh, J. McMillan, C. Biris, N. Panoiu, M. Yu, D. Kwong, A. Stein, and C. Wong, "Zero phase delay in negative-refractive-index photonic crystal superlattices," *Nature Photonics*, vol. 5, no. 8, p. 499, 2011.

[113] S. Neusser, G. Duerr, S. Tacchi, M. Madami, M. L. Sokolovskyy, G. Gubbiotti, M. Krawczyk, and D. Grundler, "Magnonic minibands in antidot lattices with large spin-wave propagation velocities," *Physical Review B*, vol. 84, no. 9, p. 094454, 2011.

[114] S. Neusser, H. G. Bauer, G. Duerr, R. Huber, S. Mamica, G. Woltersdorf, M. Krawczyk, C. H. Back, and D. Grundler, "Tunable metamaterial response of a $Ni_{80}Fe_{20}$ antidot lattice for spin waves," *Physical Review B*, vol. 84, no. 18, p. 184411, 2011.

[115] S. Datta, C. T. Chan, K. M. Ho, and C. M. Soukoulis, "Effective dielectric constant of periodic composite structures," *Physical Review B*, vol. 48, p. 14936, Nov 1993.

[116] A. Krokhin, P. Halevi, and J. Arriaga, "Long-wavelength limit (homogenization) for two-dimensional photonic crystals," *Physical Review B*, vol. 65, no. 11, p. 115208, 2002.

[117] Y. Wu, Y. Lai, and Z.-Q. Zhang, "Effective medium theory for elastic metamaterials in two dimensions," *Physical Review B*, vol. 76, no. 20, p. 205313, 2007.

[118] A. Gurevich and G. Melkov, *Magnetization oscillations and waves*. CRC Press, Boca Raton, 1996.

[119] R. W. Ziolkowski and E. Heyman, "Wave propagation in media having negative permittivity and permeability," *Physical review E*, vol. 64, no. 5, p. 056625, 2001.

[120] R. W. Boyd, R. J. Gehr, G. L. Fischer, and J. Sipe, "Nonlinear optical properties of nanocomposite materials," *Pure and Applied Optics: Journal of the European Optical Society Part A*, vol. 5, no. 5, p. 505, 1996.

[121] M. Ordal, L. Long, R. Bell, S. Bell, R. Bell, R. Alexander Jr, C. Ward, *et al.*, "Optical properties of the metals al, co, cu, au, fe, pb, ni, pd, pt, ag, ti, and w in the infrared and far infrared," *Applied Optics*, vol. 22, no. 7, p. 1099, 1983.

[122] C. Sabah and H. G. Roskos, "Numerical and experimental investigation of fishnet-based metamaterial in a x-band waveguide," *Journal of Physics D: Applied Physics*, vol. 44, no. 25, p. 255101, 2011.

[123] X. Zhou, Y. Liu, and X. Zhao, "Low losses left-handed materials with optimized electric and magnetic resonance," *Applied Physics A*, vol. 98, no. 3, p. 643, 2010.

[124] E. F. Kuester, N. Memić, S. Shen, A. Scher, S. Kim, K. Kumley, and H. Loui, "A negative refractive index metamaterial based on a cubic array of layered nonmag-netic spherical particles.," *Progress In Electromagnetics Research B*, vol. 33, 2011.

[125] S. Tacchi, M. Madami, G. Gubbiotti, G. Carlotti, A. O. Adeyeye, S. Neusser, B. Botters, and D. Grundler, "Angular dependence of magnetic normal modes in NiFe antidot lattices with different lattice symmetry," *IEEE Trans. Mag.*, vol. 46, no. 6, p. 1440, 2010.

[126] A. Barman, "Control of magnonic spectra in cobalt nanohole arrays: the effects of density, symmetry and defects," *Journal of Physics D: Applied Physics*, vol. 43, no. 19, p. 195002, 2010.

[127] S. Neusser, G. Duerr, S. Bauer, H. G. amd Tacchi, M. Madami, G. Woltersdorf, G. Gubbiotti, C. H. Back, and D. Grundler, "Anisotropic propagation and damping of spin waves in a nanopatterned antidot lattice," *Physical Review Letters*, vol. 105, p. 067208, 2010.

[128] R. Zivieri, "Metamaterial properties of one-dimensional and two-dimensional magnonic crystals," *Solid State Physics*, vol. 63, p. 151, 2012.

[129] M. Mruczkiewicz and M. Krawczyk, "Nonreciprocal dispersion of spin waves in ferromagnetic thin films covered with a finite-conductivity metal," *Journal of Applied Physics*, vol. 115, no. 11, p. 113909, 2014.

[130] M. Mruczkiewicz, E. S. Pavlov, S. L. Vysotskii, M. Krawczyk, Y. A. Filimonov, and S. A. Nikitov, "Magnonic band gaps in metallized one-dimensional yig magnonic crystals," *accepted in IEEE Transactions on Magnetics*, 2014.

[131] P. Yeh, "Electromagnetic propagation in birefringent layered media," *The Journal of the Optical Society of America*, vol. 69, no. 5, p. 742, 1979.

[132] H. Dötsch, N. Bahlmann, O. Zhuromskyy, M. Hammer, L. Wilkens, R. Gerhardt, P. Hertel, and A. F. Popkov, "Applications of magneto-optical waveguides in integrated optics: review," *The Journal of the Optical Society of America B*, vol. 22, no. 1, p. 240, 2005.

[133] A. I. Ignatov, A. M. Merzlikin, M. Levy, and A. P. Vinogradov, "Formation of degenerate band gaps in layered systems," *Materials*, vol. 5, no. 6, p. 1055, 2012.

[134] D. Szaller, S. Bordács, and I. Kézsmárki, "Symmetry conditions for nonreciprocal light propagation in magnetic crystals," *Physical Review B*, vol. 87, p. 014421, 2013.

[135] Z. Yu, G. Veronis, Z. Wang, and S. Fan, "One-way electromagnetic waveguide formed at the interface between a plasmonic metal under a static magnetic field and a photonic crystal," *Physical Review Letters*, vol. 100, p. 023902, 2008.

[136] Z. Yu and S. Fan, "Complete optical isolation created by indirect interband photonic transitions," *Nature Photonics*, vol. 3, no. 2, p. 91, 2009.

[137] W. Śmigaj, J. Romero-Vivas, B. Gralak, L. Magdenko, B. Dagens, and M. Vanwolleghem, "Magneto-optical circulator designed for operation in a uniform external magnetic field," *Optics Letters*, vol. 35, no. 4, p. 568, 2010.

[138] A. Figotin and I. Vitebsky, "Nonreciprocal magnetic photonic crystals," *Physical Review E*, vol. 63, p. 066609, 2001.

[139] F. D. M. Haldane and S. Raghu, "Possible realization of directional optical waveguides in photonic crystals with broken time-reversal symmetry," *Physical Review Letters*, vol. 100, p. 013904, 2008.

[140] Z. Wang, Y. Chong, J. Joannopoulos, and M. Soljačić, "Observation of unidirectional backscattering-immune topological electromagnetic states," *Nature*, vol. 461, no. 7265, p. 772, 2009.

[141] H. Lira, Z. Yu, S. Fan, and M. Lipson, "Electrically driven nonreciprocity induced by interband photonic transition on a silicon chip," *Physical Review Letters*, vol. 109, p. 033901, 2012.

[142] V. Yannopapas, "Non-reciprocal photonic bands in a two-dimensional holey metal filled with a magnetoelectric material," *Journal of Optics*, vol. 14, no. 8, p. 085105, 2012.

[143] V. Yannopapas, "Topological photonic bands in two-dimensional networks of metamaterial elements," *New Journal of Physics*, vol. 14, no. 11, p. 113017, 2012.

[144] H. Takeda and S. John, "Compact optical one-way waveguide isolators for photonic-band-gap microchips," *Physical Review A*, vol. 78, p. 023804, 2008.

[145] R. E. D. Wames and T. Wolfram, "Characteristics of magnetostatic surface waves for a metalized ferrite slab," *Journal of Applied Physics*, vol. 41, p. 5243, 1970.

[146] I. S. Maksymov and M. Kostylev, "Impact of conducting nonmagnetic layers on the magnetization dynamics in thin-film magnetic nanostructures," *Journal of Applied Physics*, vol. 113, p. 043927, 2013.

[147] R. E. Camley, N. E. Glass, and A. A. Maradudin, "Propagation of magnetostatic surface waves across a large amplitude grating," *Journal of Applied Physics*, vol. 53, no. 4, 1982.

[148] R. Camley, "Nonreciprocal surface waves," *Surface Science Reports*, vol. 7, no. 3-4, pp. 103 – 187, 1987.

[149] T. Wolfram and R. E. Dewames, "Surface dynamics of magnetic materials," *Progress in Surface Science*, vol. 2, 1972.

[150] H. van den Berg, "Magnetostatic-wave propagation in media with finite electrical conductivity," *IEEE Transactions on Magnetics*, vol. 27, p. 5480, 1991.

[151] Y. Okamura, K. Kitatani, and S. Yamamoto, "Characteristics of magnetostatic surface waves propagating in thin metal film coated ferrimagnetic layered structure," *IEEE Transactions on Magnetics*, vol. 29, p. 3428, 1993.

[152] Y. Okamura, A. Senoh, and S. Yamamoto, "Characteristics of magneto-static surface-wave propagating in layeredferrimagnetic structure with a slightly absorptive superstrate," *IEEE Transactions on Magnetics*, vol. 31, p. 3449, 1995.

[153] E. N. Beginin, Y. A. Filimonov, E. S. Pavlov, S. L. Vysotskii, and S. A. Nikitov, "Bragg resonances of magnetostatic surface spin waves in a layered structure: Magnonic crystal-dielectric-metal," *Applied Physics Letters*, vol. 100, no. 25, p. 252412, 2012.

[154] J. Romero Vivas, S. Mamica, M. Krawczyk, and V. V. Kruglyak, "Investigation of spin wave damping in three-dimensional magnonic crystals using the plane wave method," *Physical Review B*, vol. 86, p. 144417, Oct 2012.

[155] M. Kostylev, A. Stashkevich, A. Adeyeye, C. Shakespeare, N. Kostylev, N. Ross, K. Kennewell, R. Magaraggia, Y. Roussigné, and R. Stamps, "Magnetization pinning in conducting films demonstrated using broadband ferromagnetic resonance," *Journal of Applied Physics*, vol. 108, no. 10, p. 103914, 2010.

[156] E. Barati, M. Cinal, D. Edwards, and A. Umerski, "Calculation of gilbert damping in ferromagnetic films," in *EPJ Web of Conferences*, vol. 40, p. 18003, EDP Sciences, 2013.

[157] H. Yu, R. Huber, T. Schwarze, F. Brandl, T. Rapp, P. Berberich, G. Duerr, and D. Grundler, "High propagating velocity of spin waves and temperature dependent damping in a cofeb thin film," *Applied Physics Letters*, vol. 100, no. 26, p. 262412, 2012.

[158] T. Schwarze and D. Grundler, "Magnonic crystal wave guide with large spin-wave propagation velocity in cofeb," *Applied Physics Letters*, vol. 102, no. 22, p. 222412, 2013.

[159] S. Trudel, O. Gaier, J. Hamrle, and B. Hillebrands, "Magnetic anisotropy, exchange and damping in cobalt-based full-heusler compounds: an experimental review," *Journal of Physics D: Applied Physics*, vol. 43, no. 19, p. 193001, 2010.

[160] T. Sebastian, T. Brächer, P. Pirro, A. Serga, B. Hillebrands, T. Kubota, H. Naganuma, M. Oogane, and Y. Ando, "Nonlinear emission of spin-wave caustics from an edge mode of a microstructured co 2 mn 0.6 fe 0.4 si waveguide," *Physical review letters*, vol. 110, no. 6, p. 067201, 2013.

[161] J. Dubowik, I. Gościańska, K. Załe, ski, H. Głowiński, Y. Kudryavtsev, and A. Ehresmann, "Exchange bias in thin heusler alloy films in contact with antiferromagnet," *Journal of Applied Physics*, vol. 113, no. 19, p. 193907, 2013.

[162] M. E. Dokukin, K. Togo, and M. Inoue, "Propagation of magnetostatic surface waves in a tunable one-dimensional magnonic crystal," *Journal of the Magnetics Society of Japan*, vol. 32, no. 2 2, p. 103, 2008.

[163] Gulyaev, S. Yu.V. Nikitov, and V. Plessky, "Magnetostatic surface wave Bragg reflection from periodic system of thin conducting strips," *Technical Physics Journal*, vol. 52, p. 799, 1982.

[164] S. Vysotskii, E. Beginin, S. Nikitov, E. Pavlov, and Y. Filimonov, "Effect of ferrite magnonic crystal metallization on Bragg resonances of magnetostatic surface waves.," *Technical Physics Letters*, vol. 37, no. 11, p. 1024, 2011.

[165] S. V. Vonsovsky, *Magnetism.* New Tork: Wiley, 1974.

[166] G. Shimon, A. O. Adeyeye, and C. A. Ross, "Reversal mechanisms of coupled bi-component magnetic nanostructures," *Applied Physics Letters*, vol. 101, no. 8, p. 083112, 2012.

[167] V. V. Kruglyak, S. O. Demokritov, and D. Grundler, "Magnonics," *Journal of Physics D: Applied Physics*, vol. 43, no. 26, p. 264001, 2010.

[168] G. Carlotti and G. Gubbiotti *Journal of Physics: Condensed Matter*, vol. 14, p. 8199, 2002.

[169] J. Topp, G. Duerr, K. Thurner, and D. Grundler, "Reprogrammable magnonic crystals formed by interacting ferromagnetic nanowires," *Pure Appl. Chem.*, vol. 83, no. 11, p. 1989, 2011.

Publications

1. **M. Mruczkiewicz, E. S. Pavlov, S. L. Vysotskii, M. Krawczyk, Yu. A. Filimonov, and S. A. Nikitov, *Magnonic band gaps in metallized one-dimensional YIG magnonic crystals*, accepted in IEEE Trans. Magn., (2014)** *

2. **M. Mruczkiewicz, and M. Krawczyk, *Nonreciprocal dispersion of spin waves in ferromagnetic thin films covered with a finite conductivity metal*, J. Appl. Phys., 115, 113909 (2014)**

3. **M. Mruczkiewicz, M. Krawczyk, G. Gubbiotti, S. Tacchi, Y. A. Filimonov, D. V. Kalyabin, I. V. Lisenkov, and S. A. Nikitov, *Nonreciprocity of spin waves in metallized magnonic crystal*, New J. Phys. 15 (2013)**

4. M. Krawczyk, S. Mamica, M. Mruczkiewicz, J.W. Klos, S. Tacchi, M. Madami et al, *Magnonic band structures in two-dimensional bi-component magnonic crystals with in-plane magnetization*, J. Phys. D: Appl. Phys. 46, 495003 (2013).

5. **M. Mruczkiewicz, M. Krawczyk, and Y. Fillimonov, V. K. Sakharov, Yu. V. Khivintsev, Yu. A. Filimonov, S. A. Nikitov, *Standing spin waves in magnonic crystals*, J. Appl. Phys. 113, 093908 (2013)**

6. **M. Mruczkiewicz, M. Krawczyk, R. V. Mikhaylovskiy and V. V. Kruglyak, *Towards high-frequency negative permeability using magnonic crystals in metamaterial design*, Phys. Rev. B 86, 024425 (2012)**

7. S. Pal, B. Rana, S. Saha, R. Mandal, O. Hellwig, J. Romero-Vivas, S. Mamica, J. W. Klos, M. Mruczkiewicz, M. L. Sokolovskyy, M. Krawczyk, and A. Barman, *Time-resolved measurement of spin-wave spectra in CoO capped [Co (t)/Pt (7Å)] n-1 Co (t) multilayer systems*, J. Appl. Phys. 111, 07C507 (2012)

8. G. Venkat, D. Kumar, M. Franchin, O. Dmytriiev, M. Mruczkiewicz, H. Fangohr, A. Barman, M. Krawczyk, A. Prabhakar, *Proposal for a standard mi-*

*The bold font indicate the publications included in the PhD thesis

cromagnetic problem: Spin wave dispersion in a magnonic waveguide, IEEE Trans. Magn. 49, 524 (2013)

9. M. Krawczyk, S. Mamica, J. W. Klos, J. Romero-Vivas, M. Mruczkiewicz, and A. Barman, *Calculation of spin wave spectra in magnetic nanograins and patterned multilayers with perpendicular anisotropy*, J. Appl. Phys. 109, 113903 (2011)

10. M. Mruczkiewicz, J. W. Klos and M. Krawczyk; ISBN 978-953-307-1343-0, *Semiconductor Superlattice-Based Intermediate-Band Solar Cells*, INTECH, (2011)

Conference Presentations

1. 23.10 - 25.10 2013, COMSOL Conference, Rotterdam, Netherlands
2. 15.10 - 17.10 2013, QEINO 2013, Poznan, Poland
3. 08.09 - 13.09 2013, 42^{nd} General Meeting of Polish Physicists, Poznan, Poland
4. 09.06 - 15.06 2012, International Symposium on Spin Waves, Saint Petersburg, Russia
5. 10.10 - 12.10 2012, COMSOL Conference, Milan, Italy
6. 03.09 - 07.09 2012, International Advanced School on Magnonics, Santa Margherita Ligure, Italy
7. 30.10 - 03.11 2011, Magnetism and Magnetic Materials (MMM), Scottsdale, Arizona, USA
8. 13.09 - 15.09 2011, Nanoelectronics, Nanophotonics, and Nonlinear Physics, Saratov, Russia
9. 27.06 - 01.07 2011, Physics of Magnetism 2011 (PM'11), Poznan, Poland
10. 01.06 - 04.06 2011, Recent Trends in Nanomagnetism, Ordizia, Spain
11. 20.03 - 23.03 2011, Progress in Electromagnetics Research Symposium (PIERS), Marrakesh, Morocco

Scientific Visits

1. 20.04 - 20.07 2013, Russian Academy of Science, Saratov, Russia
2. 25.05 - 25.08 2012, Russian Academy of Science, Saratov, Russia
3. 25.04 - 25.05 2012, Physical and Technical Institute of the NAS of Ukraine, Donetsk, Ukraine
4. 01.03 - 15.03 2012, Indian Institute of Technology, Mandi, India
5. 01.07 - 31.09 2011, Russian Academy of Science, Saratov, Russia
6. 01.06 - 08.06 2011, Lawrence Berkeley National Laboratory, Berkeley, USA